UNIVERSITY OF OKLAHOMA

GRADUATE COLLEGE

STRUCTURE OF TROPOPAUSE POLAR VORTICES REPRESENTED FROM THE ATMOSPHERIC PROFILES OF SATELLITE OBSERVATIONS

A THESIS

SUBMITTED TO THE GRADUATE FACULTY

in partial fulfillment of the requirements for the

Degree of

MASTER OF SCIENCE IN METEOROLOGY

By

RYAN PAJELA
Norman, Oklahoma
2022

STRUCTURE OF TROPOPAUSE POLAR VORTICES REPRESENTED FROM THE ATMOSPHERIC PROFILES OF SATELLITE OBSERVATIONS

A THESIS APPROVED FOR THE
SCHOOL OF METEOROLOGY

BY THE COMMITTEE CONSISTING OF

Dr. Steven Cavallo, Chair

Dr. David Turner

Dr. Jens Redemann

Acknowledgments

This project would not have been possible without the following people. To Dr. Steven Cavallo and Dr. Dave Turner, I cannot express how grateful I am for your patience, and for never giving up on me. Despite every misadventure that protracted my progress, to which there were many, you saw me through to the end. To Dr. Jens Redemann, thank you not just for serving on my committee, but for the advice and assistance that I sought out from you in desperate occasions. To Dr. Amanda Kis, you were a mentor to me, helping me gain the confidence that I needed to finish this program, and I cannot thank you enough.

I must also thank all members of the Arctic and Antarctic Atmospheric Research Group, for your valuable guidance and suggestions through my research here at OU. I would like to recognize the invaluable assistance of the SoM staff for sorting out whatever unanticipated details that would come up to help me succeed. And I would like to pay my regards to those in security working the evening and graveyard hours that have gotten to know me, through many conversations over the countless late-nights and all-nighters that I've pulled in the building.

For the following people who I've met since I first started at OU, I didn't realize how much you've influenced me along the way. To Dylan and Zach, you were the ones who got me on my feet during my first year. Thanks guys for setting an example for me–not to mention I also wouldn't've been able to learn Python without you. To Alex, who was one of the first friends I've made at OU, I won't forget your company and mentorship, and for tutoring me through homework assignments last-minute. To Trey, thanks for being someone I could always chat with–also, most of my severe weather knowledge exists pretty much because of you. To Eric, thanks for our spontaneous late-night conversations as roommates, and for the continued moral support through the worst of the pandemic. And to Paulina, Lené, Dolly, Ben, and Bo, thank you for your companionship–you've each helped me in a way that meant a lot to me.

There are those from my undergraduate at UMass that have influenced me as advisors and mentors–without you I wouldn't have made it this far. To Dr. Julie Brigham-Grette, Dr. Lori Goldner, Dr. Chris Condit, and Professor Nadine Shank†, you have all been an inspiration for me, providing me direction not only academically, but with navigating life itself, especially when things were going rough. Thank you so much.

I'm very grateful for my friends Kyle and Nathan, who I've known since undergrad and who I continue share deep friendships with to this day, however many oceans and continents that lay between us. And finally, I wish to express my deepest gratitude to my family, and especially to my parents, for loving me and being present for me the whole time.

Contents

Abstract

Tropopause polar vortices (TPVs) are long-lived sub-synoptic tropopause disturbances commonly found poleward of the polar jet stream. Their roles in cyclogenesis and linkages to mid-latitude weather make them relevant to the improvement of long-range weather prediction. Previous TPV studies have been based primarily on numerical models, whereas observational studies are limited. The purpose of this study is to characterize the three-dimensional composite temperature and water vapor structure of TPVs using retrieved atmospheric quantities from the Atmospheric Infrared Sounder (AIRS) and to verify these results with the TPV structure documented in previous numerical and observational studies. The composite structure of AIRS-observed TPVs averaged over a one-year period exhibits a cold (warm) temperature anomaly and a positive (negative) relative humidity anomaly in the troposphere (lower stratosphere). TPV composites also reveal dry mixing ratio anomalies throughout the troposphere and lower stratosphere, and that the percent decrease in mixing ratio is largest at the dynamic tropopause at the vortex center. This study confirms the TPV anomaly structure previously characterized in numerical models and surface-based observations. This illustrates the potential usefulness that hyperspectral atmospheric profilers on polar-orbiting satellites have in representing TPVs over the high latitudes where observational data is scarce.

Chapter 1

Literature Review and Study Overview

Vortices are ubiquitous features of the Arctic and Antarctic atmospheres across all spatial scales. A non-exhaustive list of examples may include the planetary-scale tropospheric polar vortex (i.e., polar jet stream) and stratospheric polar vortex (i.e., polar night jet) over each hemisphere (Waugh, Sobel, and Polvani 2017); synoptic-scale surface cyclones over the Arctic (Keegan 1958; Reed and Kunkel 1960) and Southern oceans (Taljaard 1967; Simmonds, Keay, and Lim 2003); and mesoscale polar lows (Rasmussen 2003). The scope of this thesis however concerns the numerous long-lived mesoscale-to-synoptic scale vortex structures that populate the polar tropopause, giving these vortices their namesake: tropopause polar vortices (TPVs). TPVs may be either cyclonic or anticyclonic[1].

Improving the predictability of TPVs are important to the research and development of numerical weather prediction (NWP) (Cavallo and Hakim 2013) and climate models. Localized tropopause disturbances such as TPVs present a challenge in numerical models because they are non-dispersive and long-lived. In addition, TPV lifetimes are typically on the order of days to weeks but can occasionally exceed a month (Hakim and Canavan 2005; Cavallo and Hakim 2010, 2013; Borg, Cavallo, and Turner 2020; Bray and Cavallo 2022; Hakim, Bosart, and Keyser 1995). For these reasons, they become computationally expensive to forecast (Hakim, Keyser, and Bosart 1996). The primary motivation for TPV research is to improve their predictability and to fill knowledge gaps in long-range weather forecasting.

Cyclonic TPVs have been important in the surface development of high-impact weather events, such as cold air outbreaks (CAOs) (Biernat, Bosart, and Keyser 2021; Lillo et al. 2021) and tornado outbreaks (Bray, Cavallo, and Bluestein 2021), in the mid-latitudes due to their association with surface cyclogenesis (Cavallo and Hakim 2012). For example, they can initiate Rossby wave packets that become subsequently responsible for downstream cyclogenesis events in the mid-latitudes (Johnson and Wang 2021; Röthlisberger, Martius, and Wernli 2018). Studies in cyclonic TPVs have been motivated by historical winter weather events such as the 1979 Presidents' Day cyclone (Uccellini et al. 1984; Uccellini et al. 1985; Spaete, Johnson, and Schaack 1994) and the 1993 "Storm of the Century" (Uccellini et al. 1995; Huo et al. 1995; Kocin et al. 1995; Bosart et al. 1996).

In polar regions, cyclonic TPVs are important to the climate system via air-ice-ocean interactions and are thus relevant in the context of anthropogenic climatic change. For instance, they can initiate surface cyclones directly and are often precursors and/or intensifiers to strong surface cyclones in the Arctic Ocean. The surface cyclones can in turn be responsible for sea-ice loss events during the summer season (Simmonds and Rudeva 2012; Gray et al. 2021; Screen, Simmonds, and Keay 2011).

[1] Depending on the context, the usage of the term "TPV" may either refer collectively to both cyclonic and anticyclonic TPVs, or it may refer more specifically to the cyclonic TPVs. Anticyclonic TPVs are specifically referred to as ATPVs. The impact of ATPVs will not be discussed because they are not yet as understood as cyclonic TPVs. However, research in ATPVs and their impacts are underway. ATPVs are hypothesized to have a role in atmospheric blocking.

Section 1.1: Potential vorticity and vortices on the tropopause

Tropopause vortices are a well-known feature of both the extratropical (Hakim and Canavan (2005)) and the polar (e.g. Walsh et al. (2018), their section 4.f.) tropopause. For example, Price and Vaughan (1992) define a broader definition of cutoff lows (referred to as COLs in literature e.g. (Nieto et al. 2008; Fuenzalida, Sánchez, and Garreaud 2005; Pinheiro, Gan, and Hodges 2021)), classifying them into "subtropical type", "polar type", and "polar vortex type" categories (TPVs may overlap with the third category). In another example, Pyle, Keyser, and Bosart (2004) refer to long-lived vorticial structures along the tropopause as coherent tropopause disturbances (TPVs are a subset of these (Biernat, Bosart, and Keyser 2021)).

However, tropopause vortices, such as TPVs and cutoff lows, are most easily described from the context of potential vorticity (PV), which in turn derives from isentropic potential vorticity thinking (IPV-thinking (B.J. Hoskins, McIntyre, and Robertson 1985). In contrast to Rossby waves consisting of a row of alternating cyclonic and anticyclonic potential vorticity anomalies (PV-anomalies), a single PV-anomaly can be idealized as an isolated vortex (Thorpe 1986). While cutoff lows are a common example for vorticial upper-level PV-anomalies in B.J. Hoskins, McIntyre, and Robertson (1985), the IPV-thinking framework is easily extendable to TPVs.

The etymology of potential vorticity[2] (PV) is somewhat complicated (C.-G. Rossby 1940; Thorpe and Volkert 1997), but it is a quantity that depends on absolute vorticity $\zeta_a = f + \zeta_r$ (planetary vorticity plus relative vorticity) and the gradient of potential temperature ($\boldsymbol{\nabla}\theta$). The vertical component of $\boldsymbol{\nabla}\theta$ represents atmospheric stability. PV quantities are expressed in potential vorticity units (PVU), where 1 PVU = 1×10^{-6} m^2 s^{-1} K kg^{-1}. PV represented in height, isobaric/pressure, and isentropic coordinates are shown respectively in the following equation (B.J. Hoskins, McIntyre, and Robertson 1985):

$$\mathrm{P} = \frac{\boldsymbol{\zeta_a}\cdot\boldsymbol{\nabla_z}\theta}{\rho} = -\mathrm{g}\left(f\hat{\boldsymbol{k}} + \boldsymbol{\nabla_p}\times\boldsymbol{v}\right)\cdot\boldsymbol{\nabla_p}\boldsymbol{\theta} = \frac{-g\left(f + \hat{\boldsymbol{k}}\cdot\boldsymbol{\nabla_\theta}\times\boldsymbol{v}\right)}{\frac{\partial \mathrm{p}}{\partial\theta}}. \qquad (1)$$

In isentropic coordinates, $\boldsymbol{\nabla}\theta$ simplifies to static stability (∂p/$\partial\theta$) because isentropic levels have constant θ. Air parcels that are advected horizontally in an adiabatic flow will tend to translate along levels of constant θ, remaining on the same isentropic level. PV is a conserved quantity in adiabatic flows (i.e., PV cannot be created nor destroyed without diabatic forcing) and will change only in the presence of nonconservative processes such as diabatic heating and friction (Stoelinga 1996). PV on an isentropic surface is called isentropic potential vorticity (IPV).

From a vertical cross-sectional perspective, positive (negative) PV-anomalies will be associated with more (less) stable vertical temperature gradients. Diabatic heating mechanisms such as shortwave and longwave radiation and latent heating alter the vertical potential temperature profile and can thus intensify or weaken both upper-level and lower-level PV-

[2] Potential vorticity (PV) hereafter will always reference Ertel's potential vorticity (EPV) and not quasi-geostrophic potential vorticity (QGPV).

anomalies (B.J. Hoskins, McIntyre, and Robertson 1985). The theoretical structure of upper-level, axisymmetric PV-anomalies can be viewed in Figures 1 and 2 in Thorpe (1986).

In general, mechanisms such as latent heating from clouds in the mid-troposphere will increase (decrease) lapse rates with respect to height in the lower (upper) troposphere, thus increasing (decreasing) the PV in the lower (upper) troposphere (e.g., Wirth (1995)). On the other hand, the reverse effect will occur under a clear-sky free atmosphere where radiative cooling is maximized in the mid-troposphere (e.g. Figures 2a and 4a in (Zierl and Wirth 1997)). A diabatically-driven thermally indirect circulation between the vortices' centers and peripheries is present in both studies (Wirth 1995; Zierl and Wirth 1997).

The evolution of axisymmetric tropopause vortices in the presence of diabatic heating has been investigated in idealized numerical studies. For example, Wirth (1995) performed experiments with an idealized cold-core cyclonic cutoff low with mid-tropospheric diabatic latent heating to simulate deep convection, resulting in the weakening of the vortex from PV destruction. In another example, an idealized tropopause anticyclone is given in Zierl and Wirth (1997), where a radiatively driven diabatic heating profile with cooling (heating) in the troposphere below (stratosphere above) the tropopause results in PV creation that weakens the anticyclone.

Further studies have been conducted on the interaction between upper-level and lower-level PV-anomalies in the presence of nonconservative mechanisms via idealized simulations (e.g., Takayabu (1991)) and numerical simulations of real-world weather events (e.g., (Stoelinga 1996; Takayabu 1991; Davis and Emanuel 1991)).

Section 1.2: The physical atmospheric environment at high latitudes

Over the Arctic and the Antarctic reside numerous TPVs that are bounded by the tropospheric polar vortex (e.g., Hakim and Canavan (2005)), which in turn separates them from tropopause vortices at lower latitudes (such as cutoff lows and blocking highs). Being in polar regions, TPVs experience a different physical environment than tropopause vortices over the mid-latitudes. Polar regions differ from the mid-latitudes both dynamically and thermodynamically.

Dynamically, the variation of the Coriolis parameter f with respect to latitude (the β-effect) becomes negligible at high latitudes, so vortices become favorable over Rossby waves (Hakim 2000). Moreover, vortices will tend to remain stationary when β is absent, assuming no background flow (e.g. J. McWilliams (1991)). On the other hand, β is important in the mid-latitudes. Not only do Rossby waves become common synoptic features, but vortices are also no longer stationary. When β is present, cyclonic vortices propagate to the northwest (southwest) in the Northern (Southern) Hemisphere (also assuming no background flow) (e.g. (C. Rossby 1948; Adem 1956; Reznik and Dewar 1994; Hakim 2000)). The westward component of the translational velocity of a vortex also increases with vortex size (e.g. J.C. McWilliams and Flierl (1979)). Lower-latitude cyclonic vortices have been recorded to exhibit this behavior after accounting for background flow (Hakim 2000).

However, when β is neglected in polar regions, the presence of "synoptic scale" topographies (i.e., the Greenland and East Antarctica ice sheets) can introduce local PV gradients

since ζ_a/h is constant, where h is the depth of the atmospheric column[3] (C.-G. Rossby 1940; B.J. Hoskins, McIntyre, and Robertson 1985). As long as the topography has a length scale larger than that of the cyclonic vortices, the vortices propagate to the "local northwest (southwest)" in which "north" ("south") is oriented in the direction of the topographic gradient in the geographic Northern (Southern) hemisphere (Carnevale et al. 1988) (this assumes the absence of background flow). This might be one possible reason why cyclonic TPVs on average travel from the geographic southwest to the northeast over Greenland (Borg, Cavallo, and Turner 2020), or from "local southeast" to "local northwest" from a topographic perspective.

There are also thermodynamic characteristics that are unique to the polar regions and that are highly interconnected with one another. These include the seasonal cycle of solar radiation, the effects of snow and sea-ice on surface albedo, and the vertical distribution and phase of arctic clouds. Arctic clouds have been an important topic of study because of challenges of their representation in models (e.g., (De Boer et al. 2012; Pithan, Medeiros, and Mauritsen 2014; Tjernström, Sedlar, and Shupe 2008)).

There are numerous studies of the impact of arctic clouds on the surface radiation budget (e.g., (J.A. Curry et al. 1996; J. Curry, Schramm, and Ebert 1993; Shupe and Intrieri 2004)), but they are important throughout the vertical extent of the troposphere as well. Clouds containing liquid water are common in the Arctic (e.g., (Shupe et al. 2011; Cesana et al. 2012)), and have a higher impact on atmospheric radiation than ice-only clouds, which have little effect by comparison (Shupe and Intrieri 2004; Stramler, Del Genio, and Rossow 2011; Turner, Shupe, and Zwink 2018). Longwave radiative cooling in the proximity of the cloud top of liquid-only and mixed phase clouds are the largest contributors to the vertical heating profile in the Arctic. In instances in which there are two cloud layers and at least one is liquid-bearing, the uppermost liquid-bearing cloud layer is the primary contributor of cloud-top radiative cooling (Turner, Shupe, and Zwink 2018). Many of these mechanisms become important in how TPVs are maintained and how they evolve over time (Cavallo and Hakim 2013, 2012), which is discussed in the next section.

Section 1.3: Tropopause polar vortices in the Arctic

For this point onward TPVs will reference only cyclonic TPVs rather than cyclonic TPVs and ATPVs collectively. The same applies when referencing vortices in general unless otherwise noted.

IPV-thinking is a useful tool in analyzing tropopause disturbances (e.g. (Uccellini et al. 1984; Uccellini et al. 1985; Kew, Sprenger, and Davies 2010; B. Hoskins and Berrisford 1988)), but it has the disadvantage of requiring multiple isentropic surfaces. An alternative approach by Morgan and Nielsen-Gammon (1998) uses a surface of constant PV in which potential temperature is a conserved quantity. Surfaces of constant PV can be used to define a dynamic tropopause, where values ranging from 1–3.5 PVU have previously been used (Spaete, Johnson, and Schaack 1994; Hoerling, Schaack, and Lenzen 1991; Morgan and Nielsen-Gammon 1998).

The 2 PVU surface currently defines the dynamic tropopause and is used to identify TPVs along the tropopause. On a dynamic tropopause map, a TPV will have local minimum of potential temperature surrounded by closed isentropes. The largest closed isentrope around the

[3] Topographic Rossby waves would apply in this case but will not be discussed.

TPV defines the separation of the TPV from the background flow. A TPV's amplitude (expressed in K) is the difference between the values of the θ minimum and last closed θ isentrope (Cavallo and Hakim 2012, 2010, 2009).

In Hakim and Canavan (2005), tropopause vortices in the Arctic have been a subject of study because of their separation from the polar and subtropical jet streams. This subset of vortices was desirable because it enabled direct comparisons between real-world vortices and vortices in idealized simulations. Arctic vortices on the tropopause have been enacted to satisfy the requirements having lifetimes of at least 48 hours, and spending 60% of their lifetime north of the 65˚N latitude circle (Hakim and Canavan 2005). It is at around 48–72-hours in which the amplitude and radii of the vortices do not change as much with respect to time (Figure 5a, b, & d in Hakim and Canavan (2005)). These requirements have been used in subsequent studies of TPVs.

There are a number of studies that investigate the mechanisms that influence changes in TPV intensity, as TPVs in the absence of any forcing will simply be translated by the background flow. TPV intensity change is expressed as PV tendency. The equation in height coordinates in the Lagrangian format is displayed below. **F** is the surface friction vector and is neglected (the second term is effectively zero) because TPVs are along the tropopause (Cavallo and Hakim 2013):

$$\frac{DP}{Dt} = \frac{\boldsymbol{\zeta_a}}{\rho} \cdot \boldsymbol{\nabla}\left(\frac{\mathrm{D}\theta}{Dt}\right) + \frac{\boldsymbol{\nabla}\theta}{\rho} \cdot \left(\frac{\boldsymbol{\nabla} \times \boldsymbol{F}}{\rho}\right). \tag{2}$$

Potential temperature tendency (the material derivative of θ) can be decomposed into separate constituent diabatic processes. Longwave radiation (LW), shortwave radiation (SW), and latent heating (LH) make up the bulk of the overall potential temperature tendency, while other processes such as convection, boundary layer effects, and entrainment have a negligible effect and are generally neglected (Cavallo and Hakim 2009, 2010, 2012, 2013):

$$\frac{\mathrm{D}\theta}{Dt} = \dot{\theta} = \dot{\theta}_{LW} + \dot{\theta}_{SW} + \dot{\theta}_{LH} + \dot{\theta}_{everything\ else}\ . \tag{3}$$

The intensity and evolution of TPVs are influenced by local factors rather than by larger circulation patterns in their surrounding environment (Cavallo and Hakim 2009). Local factors may include whether a TPV is over land or water, whether it is polar day or polar night at the TPV's location, and the distribution of ice, liquid, and/or mixed phase clouds within the TPV. One example is a case study of a long-lived TPV by Cavallo and Hakim (2009), where the TPV strengthens over Siberia as a result of cloud-top radiative cooling being the dominant θ tendency. The TPV weakens over Hudson Bay and eastern Canada as the locality introduces moisture, and the magnitude of latent heating becomes comparable to that of radiation.

Overall, LW radiation is the primary driver for PV creation and TPV intensification. Composites of Canadian TPVs as anomalies to a 2-year background climatology show a warm (cold) temperature anomaly above (below) the lowered tropopause at the TPV core (Cavallo and Hakim 2010). Water vapor also plays an important role in LW cooling within a TPV. TPV composites exhibit a negative (positive) relative humidity anomaly above (below) the vortex-centered tropopause (Cavallo and Hakim 2010) (e.g., Figures 9a, 9d, 14a-d). Anomalously dry air over the lowered tropopause of the TPV increases the vertical water vapor gradient with

respect to height across the tropopause at the TPV core. This increases LW cooling at the tropopause and contributes to TPV intensification and maintenance (Cavallo and Hakim 2013).

The destructive effect of SW radiation on PV has a much lower magnitude than the PV-generating effect of LW radiation. SW radiation slightly reduces TPV intensification in the presence of LW cooling alone but has a larger abating effect when cloud effects are included. Ozone is an absorber of SW radiation, but the effect of increased ozone concentration above the tropopause at the TPV core does not show to have much effect on TPV intensification (Cavallo and Hakim 2013). Ozone concentrations in the upper troposphere and lower stratosphere are much lower than in the middle and upper stratosphere, even within a TPV, and thus the radiative impact of ozone is minimal.

Longwave radiative cooling in the clear-sky atmosphere is the primary contributor to TPV intensification. However, the presence of clouds and cloud-top radiative cooling can further increase cooling rates and PV creation in the vicinity of the tropopause. In addition, while latent heating has a destructive effect of PV in the troposphere, its effects are small in comparison to LW radiative forcings (Cavallo and Hakim 2013). Overall, LW radiation is a key ingredient to TPV intensification and maintenance, and TPVs will weaken without it (Cavallo and Hakim 2012).

Ongoing studies of TPVs and their structure and evolution have begun to include an observational component to verify model studies. While an early TPV case study utilized observations from radiosonde data over Coral Harbour, Nunavut, Canada and imagery from the Moderate Resolution Imaging Spectroradiometer (MODIS) (Figures 5 and 6 from Cavallo and Hakim (2009)), the initial characterization of TPVs (Cavallo and Hakim 2013, 2012, 2010, 2009) as well as subsequent TPV studies (e.g., (Biernat, Bosart, and Keyser 2021; Johnson and Wang 2021; Lillo et al. 2021; Papritz et al. 2019; Bray and Cavallo 2022; Bray, Cavallo, and Bluestein 2021)) have primarily relied on idealized models, forecast models, and/or reanalysis data.

The first in-depth observational study of TPVs was conducted by Borg, Cavallo, and Turner (2020). This study utilizes the ShupeTurner (ST) retrieval algorithm (Shupe et al. 2015) which in turn uses surface-based radar, lidar, radiometry, and interferometry observations from the Summit Station on Greenland (the specific instruments used can be seen in Table 1 of Shupe et al. (2015)). In this study, observed TPVs whose paths intersect the Summit Station were considered. TPV cloud properties were investigated in case studies (Figures 4, 5, and 7 in Borg, Cavallo, and Turner (2020)), and time-height composites of clear-sky LW heating rates for intensifying and weakening TPVs (Figures 10 and 11 in Borg, Cavallo, and Turner (2020)). These composites were further decomposed into water vapor contributions and temperature contributions to the PV budget, where water vapor (temperature) contributions were the dominant clear-sky LW forcing in strengthening (weakening) TPV cases (Borg, Cavallo, and Turner 2020). The general TPV composite structure was also consistent with that in Cavallo and Hakim (2010), except for the absence of a positive relative humidity anomaly below the tropopause in the TPV core (Figure 9 from Borg, Cavallo, and Turner (2020)).

Section 1.4: Study overview

The observation network in the polar regions has remained sparse in comparison to lower latitudes by nature of their remoteness from human habitation. While TPVs can be observed directly using radiosonde data, such occurrences are infrequent due to TPVs being sub-synoptic features in constant motion that must be further intercepted by fixed stations. In recent decades, polar-orbiting satellites have become integral to Earth-observation systems in the high latitudes, greatly increasing the coverage and data availability from these regions. Atmospheric profilers aboard polar-orbiting satellites are thus potentially powerful tools for observing the three-dimensional structure and variability of the atmospheric state of TPVs.

This study utilizes the AIRS/AMSU Version 7 Level 2 Product (Thrastarson et al. 2020), the most recently updated AIRS/AMSU L2 product developed by the Jet Propulsion Laboratory (Thrastarson et al. 2021). This dataset is derived from infrared and microwave spectra collected by the Atmospheric Infrared Sounder (AIRS) and Advanced Microwave Sounding Unit (ASMU) instruments aboard the low-orbit polar-orbiting Aqua satellite (Thrastarson et al. 2021; Aumann et al. 2003; Aumann and Pagano 1994). This product is also ideal for TPV research due to its robustness in penetrating through cloudy environments (Joel Susskind et al. 2006; Joel Susskind, Barnet, and Blaisdell 2003).

The purpose of this study is to add to the growing body of observational TPV research, and is conducted in the context of past model studies (Cavallo and Hakim 2013, 2010) and observational studies (Borg, Cavallo, and Turner 2020). While Borg, Cavallo, and Turner (2020) addresses both the spatial structure and temporal evolution of TPVs, this study takes advantage of the three-dimensionality of the AIRS/AMSU V7 L2 data product and Aqua's frequent coverage of polar regions where TPVs reside, and thus emphasis is placed on the composite spatial structure of TPVs.

TPVs in the North and South Polar geographic regions are investigated over a one-year period from September 2015 through August 2016. The structure of TPVs will be represented by the spatial distribution of temperature, moisture, and ozone variables within satellite-observed TPVs. TPV structure will also be compared between the spring (MAM), summer (JJA), autumn (SON), and winter (DJF) seasons. This study addresses the following questions and hypotheses:

Question: Is the overall composite structure of TPVs characterized in numerical model studies reproducible using AIRS/AMSU-derived observations?

Hypothesis: There will be no notable difference in the overall structure of the temperature nor the humidity profiles other than a difference in magnitude.

Question: Is the overall composite structure of TPVs characterized from ground-based observations at Summit Station, Greenland consistent with TPVs characterized from AIRS/AMSU-derived observations?

Hypothesis: There will be no notable difference in the overall temperature structure other than a difference in magnitude. There are expected to be qualitative differences in the relative humidity profiles of TPVs between this study and a previous study conducted by

Borg, Cavallo, and Turner (2020). TPVs over Greenland lack the anomalously high relative humidities in the lower troposphere that are present in TPVs over the Canadian Arctic, presumably due to the altitude of the local geography (Borg, Cavallo, and Turner 2020; Cavallo and Hakim 2010). Most AIRS/AMSU Arctic observations will be over low topography because most of the Arctic region is topographically low. The average Northern Hemisphere TPV in this study will therefore reflect a relative humidity profile of TPVs over low altitudes, such as those over the Canadian Arctic, rather than a relative humidity profile of TPVs over high altitudes, such as those over Greenland.

Question: Are there detectable differences in composite structure between TPVs of the Northern and Southern Hemispheres based on AIRS/AMSU-derived observations?

Hypothesis: There are expected to be measurable differences in the composite temperature profiles of TPVs between the Northern and Southern Hemispheres. The maximum amplitude and maximum θ anomaly distributions of TPV populations in the Northern and Southern Hemispheres have been shown to be statistically different across all seasons albeit being similarly shaped (Gordon, Cavallo, and Novak 2022), so TPV temperature profiles are expected to differ between hemispheres in this study. There will be no measurable difference in the overall structure of mixing ratio[4]. Since humidity profiles of Southern Hemisphere TPVs have yet to be fully characterized, a null hypothesis for differences in mixing ratio is assumed.

This study is divided into four chapters. Chapter 1 consists of this literature review, which has surveyed select topics relevant to TPVs, including the PV framework, general tropopause vortices, high-latitude dynamic and thermodynamic environments, arctic clouds, and TPV structure and mechanisms of evolution. Chapter 2 covers the TPV tracking algorithm utilized in this study, the collocation of tracked TPVs with coincident AIRS/AMSU observations, and the compositing methods for the collection of observed TPV cases. Chapter 3 reports the resultant TPV composites from AIRS/AMSU data. Chapter 4 compares these results with previous composite studies and discusses the structural variability between seasons and hemispheres. Chapter 4 also discusses the limitations of this study's methodology and results which must be considered during interpretation.

[4] Temperature and relative humidity will be examined when comparing this study to previous studies, as these were the variables examined in previous studies. For comparisons between TPVs in the Northern and Southern Hemispheres, mixing ratio will be used instead of relative humidity to make quantitative comparisons of TPV structure between hemispheres. This is because temperature and mixing ratio have corresponding observational errors in the AIRS/AMSU L2 product, whereas relative humidity does not.

Chapter 2

Methods

The AIRS/AMSU Version 7 Level 2 Standard Product is the principal observational dataset utilized in this study to characterize the three-dimensional spatial structure of TPVs. The Atmospheric Infrared Sounder (AIRS) and the Atmospheric Microwave Sounding Unit (AMSU) are atmospheric profilers aboard the Aqua polar-orbiting satellite (Aumann et al. 2003). Both instruments were jointly utilized by the Jet Propulsion Laboratory (JPL) to develop the AIRS/AMSU V7 L2 products (Thrastarson et al. 2021), which utilizes the most recent version of the AIRS science team AIRS/AMSU retrieval algorithm (J Susskind et al. 2020).

As the Aqua satellite orbits, the AIRS and AMSU instruments take individual atmospheric profiles in a row from left to right (across-track) relative to the direction of the satellite trajectory (along-track) before continuing to the next row (**Figure 2.0.1**). The satellite data swath is almost continuous (except for data outages), but the AIRS/AMSU L2 product is organized into segments called granules. There are 240 granules for each 24-hour period, with each granule spanning 6 minutes (**Figure 2.0.2**) (Thrastarson et al. 2020; Thrastarson et al. 2021).

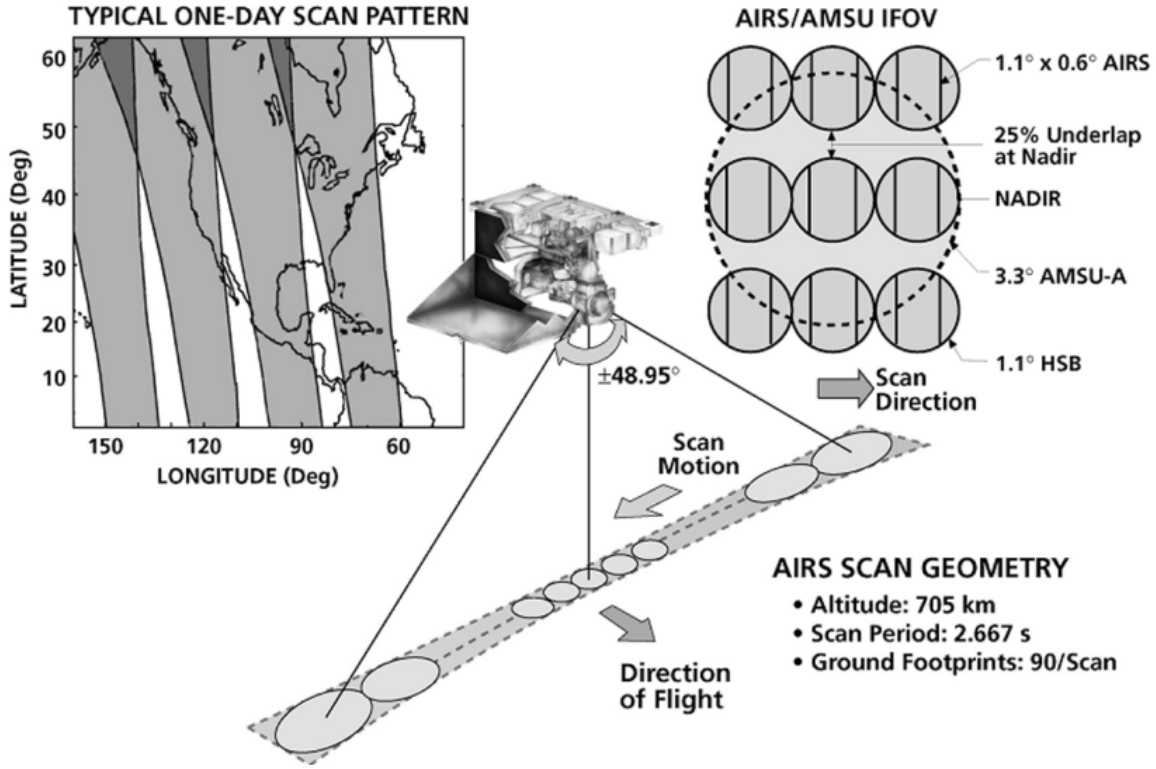

Figure 2.0.1: Schematic of AIRS data collection. AIRS swaths are depicted in the top-left. Each AIRS/AMSU profile (9 AIRS footprints + 1 AMSU footprint) is displayed on the top-right. A single row of an across-track scan is depicted in the center image. © 2003 IEEE; Figure 1 from (Aumann et al. 2003)

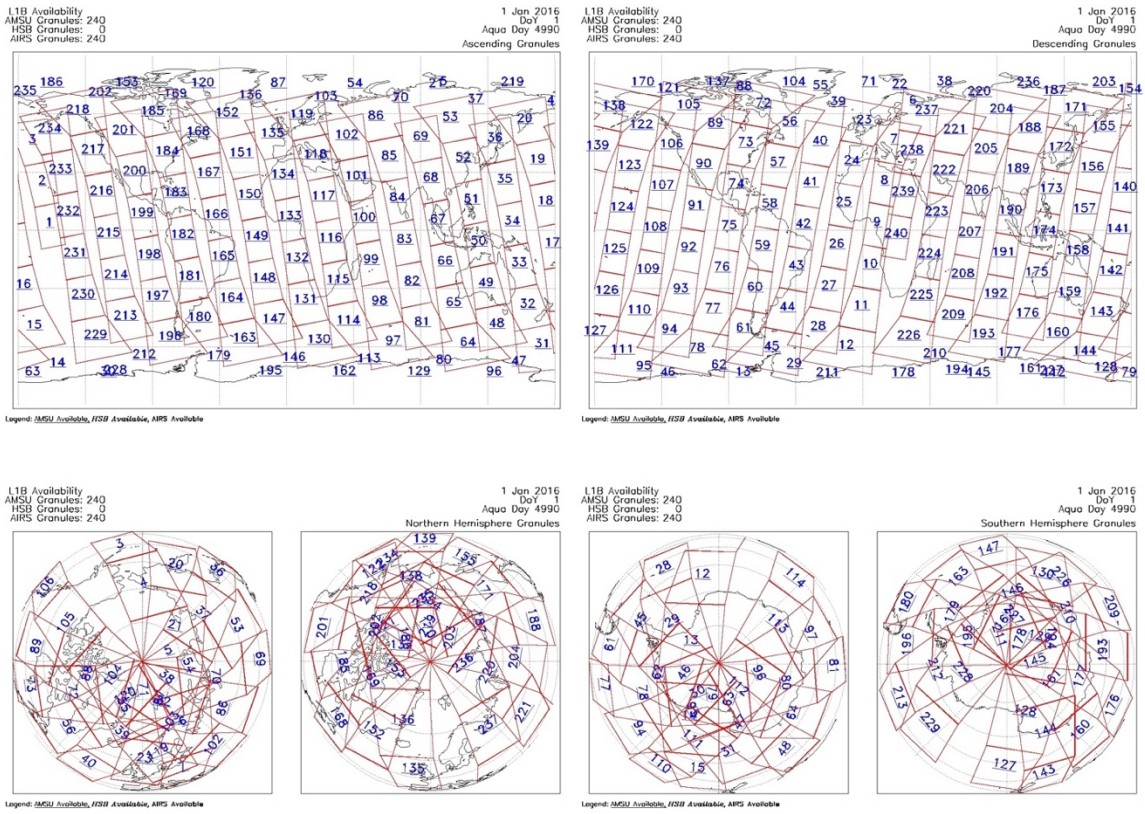

Figure 2.0.2: Granule maps for 1 January 2016. Displayed are the ascending nodes (top-left); descending nodes (top-right); North Polar view (bottom-left); and South Polar view (bottom-right). Each granule is given a number from 1–240 every 24 hours. Credit: NASA/JPL-Caltech

Granule data are arranged in a rectangular array consisting of 45 atmospheric profiles per column in the along-track direction and 30 atmospheric profiles per row in the across-track direction, for a total of 1350 atmospheric profiles per granule. The spatial resolution of the data product is given by the distance between the atmospheric profiles. Profiles are approximately 45-50 km apart in the along-track direction. In the across-track direction, distances between profiles range from 45-50 km at the nadir of Aqua and increase to slightly above 100 km between profiles toward the lateral edges of the AIRS granules. Each granule also has dimensions of approximately 2250 km by 1650 km in the along-track and across-track directions respectively[5]. (Thrastarson et al. 2020; Thrastarson et al. 2021).

The primary challenge in observing features such as TPVs via a polar-orbiting satellite is the process of geolocating TPVs to incidental satellite overpasses. This process consists of using reanalysis data to locate an appropriate TPV at a given timestep (day and hour) and seeking the corresponding granule(s) at that date which intercepts the TPV. This can be done manually for single TPV cases. However, manual coordination of TPVs to satellite overpasses becomes unwieldly for large sample sizes, necessitating automated methods.

[5] Further information can be found at https://airs.jpl.nasa.gov/data/about-the-data/granules/.

Section 2.1: Tropopause polar vortex tracking

The geolocation of TPVs and the tracking of their trajectories was performed using the TPVTrack Version 1.0[6] software developed by Szapiro and Cavallo (2018) on the ERA5 High-Resolution hourly reanalysis dataset by the European Centre for Medium-Range Weather Forecasts (ECMWF) (Hersbach et al. 2020). TPV tracking was conducted on an ERA5 2 PVU single level at a 0.25˚-by-0.25˚ longitude-latitude resolution, with the potential temperature and the u- and v-wind components taken as the input variables. TPVTrack was developed prior to the release of ERA5 and had been tested with ERA Interim (Szapiro and Cavallo 2018; Dee et al. 2011), although testing with ERA5 is ongoing. One software setting was modified from its default value to account for the higher spatial and temporal solution of ERA5 with respect to ERA Interim[7].

A one-year observed period from 1 September 2015, through 31 August 2016 was selected for this study. This period covers the twelve most recent full months before the AMSU had degraded to a point in which JPL deemed it no longer useable on September 24th, 2016[8] (Thrastarson et al. 2021; Thrastarson et al. 2020). While a period over multiple years could have been analyzed, this study was limited to a single year due to computational and time limitations. Tracking, however, was conducted over a two-year period from 2015 through 2016. This was done so that TPV tracks whose lifetimes span beyond the starting or ending points of the observation period would be detected[9].

At each hourly timestep, TPVTrack identifies 2-PVU potential temperature minima using a watershed segmentation image processing technique (Szapiro and Cavallo 2018). This segmentation method identifies candidates for TPVs at each timestep; these entities are referred to as "basins" (owing to the context of the watershed segmentation method) and occupy a 2-dimensional geographic extent over latitude-longitude grid cells. Each basin is associated with a basin "center", which is the longitude and latitude of the potential temperature minimum in each basin. Basins have further attributes including "area", (calculated by summing the areas of each grid cell occupied by a given basin), "amplitude" (the difference in potential temperature between the center and the edge of the basin), and "equivalent radius" (calculated by taking the square root of the area divided by π for each feature). TPVTrack then tracks the horizontal motion of the basins and their associated centers over the course of the basin's lifetime[10]. The trajectory of each basin center over the course of the basin's lifetime is referred to as a "track".

The identified tracks of the TPVTrack output were then postprocessed to include only those that meet the criteria for TPV identification: having lifetimes of at least 48 hours and spending at least 60% of their lifetime poleward of the respective 65˚ North and South parallels

---

[6] The GitHub page can be found at https://github.com/nickszap/tpvTrack. Default software settings can be found under *my_settings.py*.

[7] Another observational TPV study (Borg et al., 2020) was the first to implement TPVTrack on ERA5, where (after consulting with the developer) the parameter *segRestrictPerc* (see footnote 6) was modified from 10 (default) to 5. All other settings retained their default values. This study assumes this same parameter change utilized in Borg et al. (2020).

[8] The AIRS/AMSU product covers from 30 August 2002 through 24 September 2016. A separate AIRS-only product covers from 30 August 2002 to the present.

[9] Only the portions of their lifetimes residing within the bookends of the observation period were included.

[10] The watershed segmentation and correspondence algorithms of the TPVTrack software will not be discussed further as they are beyond the scope of this study.

as per precedent (Hakim and Canavan 2005). Tracks that did not meet these criteria were excluded from this study. These specifications were implemented to approximate features that are sufficiently separated from the polar jet stream. All tracks and associated basins that satisfied these criteria were considered TPVs.

Section 2.2: Collocation of tracking basins to satellite swaths

This process discussed in this section utilized the Environmental Systems Research Institute (ESRI) ArcGIS Desktop 10.8.1 software (Esri 2011) on multiple Microsoft Windßows operating system desktop computers that were run simultaneously over several days[11]. TPVTrack basin output was postprocessed to many NetCDF files, one file for each hourly timestep. These files were then imported to GIS software as raster data. The TPV basins at each timestep were then converted from raster data to polygon features. Each step was conducted iteratively. The TPV centers from the tracking output were imported separately into the GIS software as point features. For the corresponding satellite geolocation data, the longitudes and latitudes of the AIRS/AMSU profiles from each granule were imported as point features before being collectively converted into a polygon feature representing the AIRS/AMSU granule (**Figure 2.2**). This was also conducted iteratively.

Table 2.2: AIRS/AMSU granules are represented by granule numbers 1–240 for each calendar date. Only a subset are shown here (left column). Each granule represents six minutes of data collection. The start time of each granule is shown (center column). The end time of each granule would be the start time of the subsequent granule. To make AIRS/AMSU granules compatible with ERA5 hourly data, each granule was associated to its nearest whole hour in UTC (right column).

Granule Number	Granule Start Time (UTC) (hh:mm:ss)	Nearest ERA5 hourly timestep (UTC)
240	23:59:22	00
1	00:05:22	00
2	00:11:22	00
3	00:17:22	00
4	00:23:22	00
5	00:29:22	01
6	00:35:22	01
7	00:41:22	01
8	00:47:22	01
9	00:53:22	01
10	00:59:22	01
20	01:59:22	02
30	02:59:22	03
60	03:59:22	06
120	11:59:22	12

[11] For this reason, this method is (in hindsight) not recommended for collocating TPVs with satellite overpasses.

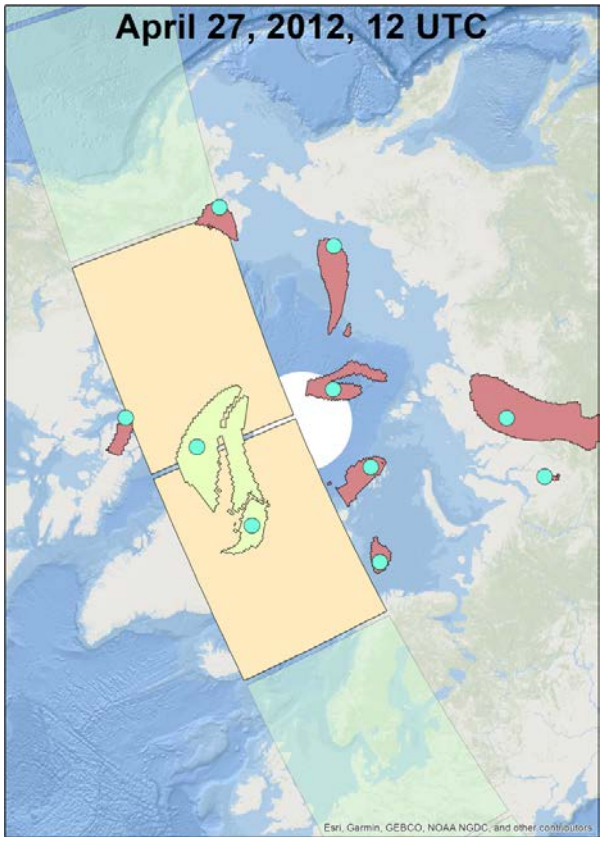

Figure 2.2: TPVTrack output for a single timestep on 12 April 2012 (Note that this is outside the study period). TPV basins (centers) are represented by dark pink/light green shapes (cyan circles). Basins associated with tracks not meeting TPV criteria (Hakim and Canavan 2005) have been filtered out in this illustration. All qualifying TPV basins and centers output from TPVTrack are shown here regardless of amplitude or equivalent radius. The rectangles represent AIRS granules. The two highlighted TPVs residing completely within the AIRS swath are highlighted. These TPVs would be provisionally included as TPV samples unless further restrictions are implemented (e.g., minimum amplitude, minimum equivalent radius). The AIRS granules intersecting the highlighted TPVs are also highlighted. Illustration was created using ESRI ArcMap 10.8.1

TPV output data is reported at the same longitude-latitude resolution (0.25˚-by-0.25˚) and timestep (hourly) as ERA5. To acquire TPV cases, TPVTrack output basins at each hourly timestep were geographically and temporally superimposed over any AIRS granules ± 30 minutes of that timestep, i.e., granules after 1130 UTC and before 1230 UTC would correspond with the 12 UTC timestep (**Figure 2.2**, **Table 2.2**).

Only TPV basins that resided entirely within the geographic domain of a given AIRS overpass were included as satellite-observed cases for this study (**Figure 2.2**). Those that partially overlapped the overpass were excluded. TPVs spanning two consecutive granules but remained within the lateral boundaries of the satellite overpass were included unless the two granules were assigned to different timesteps. For example, one granule that temporally spans approximately 12:24–12:30 is assigned to the 12 UTC timestep, while the next granule that temporally spans from 12:30–12:36 is assigned to the 13 UTC timestep (see **Table 2.2**).

Section 2.3: Case selection

Once a database of satellite-observed TPV samples had been compiled, TPV cases were further subset by amplitude and equivalent radius. Since the vertical and horizontal resolutions for the AIRS/AMSU V7 L2 Product are ~1 km and ~50 km, respectively (Thrastarson et al. 2020), smaller and/or weaker TPVs may not be sufficiently resolved by AIRS/AMSU. Therefore, TPVs were selected by the following criteria:

1) TPV cases with a minimum amplitude of 10 K were selected as a conservative approximation for 1 km in the vertical direction, assuming a dry adiabatic lapse rate of 9.8 K/km.
2) Selected TPV cases also had a minimum equivalent radius of 200 km. While this value is arbitrary, it was chosen so that the horizontal structure within the TPV can be easily viewable in granule data by the human eye.

The geographic distributions of TPVs over each hemisphere are given in **Figures 2.3.1 and 2.3.2**, and corresponding sample sizes are given in **Tables 2.3.1 and 2.3.2**. Distributions of amplitude and equivalent radius are given in **Figures 2.3.3 and 2.3.4**. Note that TPV samples are highly dependent on one another, as it was not uncommon for the same TPV to be observed under the Aqua satellite in two or more consecutive orbits. However, there is expected to be at least as many independent samples as there are unique tracks (**Tables 2.3.1 and 2.3.2**).

Table 2.3.1: Sample sizes and unique tracks in the Northern Hemisphere for all TPVs output by TPVTrack (top row) and TPVs observed completely within an AIRS/AMSU swath (bottom row). Samples are dependent due to temporal autocorrelation. The effective sample size in each category is expected to be between the number of unique tracks and the number of dependent TPV samples for that category.

NH	All amplitudes All radii	Amplitudes ≥ 10 K Radii ≥ 200 km
All TPVs	90531 (samples) 838 (unique tracks)	23451 (samples) 368 (unique tracks)
TPVs under AIRS	12125 (samples) 838 (unique tracks)	*2378 (samples)* *272 (unique tracks)*

Table 2.3.2: As in **Table 2.3.1**, except for the Southern Hemisphere.

SH	All amplitudes All radii	Amplitudes ≥ 10 K Radii ≥ 200 km
All TPVs	97686 (samples) 981 (unique tracks)	18767 (samples) 473 (unique tracks)
TPVs under AIRS	14884 (samples) 978 (unique tracks)	*2312 (samples)* *345 (unique tracks)*

Local maxima of TPV density in the Northern Hemisphere occur over the Canadian Archipelago, the northern coast of Greenland, and the region north of the Siberian coast. In the Southern Hemisphere, one local maximum occurs over the Ross Ice Shelf, and two more maxima occur over the East Antarctic interior along an imaginary straight line spanning from the Ronne-Filchner Ice Shelf to the Amery Ice Shelf. This is true for TPVs of all amplitudes and equivalent radii and for TPVs with amplitudes (equivalent radii) of at least 10 K (200 km).

Due to the incline of Aqua's orbit being slightly less than 90˚ relative to the equatorial plane, coverage of TPVs under AIRS/AMSU exhibits a ring-shaped domain surrounding each pole. As a result, AIRS coverage does not perfectly collocate with TPV density maxima (**Figures 2.3.1 and 2.3.2**).

For the rest of this section and for the rest of Chapter 2, all TPVs mentioned will refer to only those with a minimum amplitude of 10 K and a minimum equivalent radius of 200 km. For each hemisphere, the distributions of the amplitudes and equivalent radii of TPV cases that were selected for observation by AIRS/AMSU were compared to the population of TPVs output by TPVTrack. The probability distribution functions for amplitude (**Figure 2.3.5**) and equivalent radius (**Figure 2.3.6**) between TPVs under AIRS and all TPVs output by TPVTrack were plotted and overlaid for visual comparison.

Under visual inspection, the amplitude histograms between the TPVTrack TPVs and AIRS TPVs are generally consistent with one another. This is the true for both hemispheres, although there may be few minor discrepancies for individual bins, such as the 10–12 K bin for the Southern Hemisphere (**Figure 2.3.5**). On the other hand, the histograms for equivalent radius visibly differ between the TPVTrack TPVs and AIRS TPVs. The Northern Hemisphere histograms have a prominent discrepancy where there are proportionally more TPVs with equivalent radii of less than 300 km for TPVs observed under AIRS/AMSU versus all TPVs from TPVTrack. Additionally, the Northern (Southern) Hemisphere histogram also exhibits slightly less (slightly more) AIRS TPVs with equivalent radii of approximately 350–600 km (approximately 400–600 km) than the TPVTrack TPVs whose equivalent radii fall within the same interval (**Figure 2.3.6**).

Following-up the above visual inspection, further determination of whether the TPVs under AIRS/AMSU can be considered a random sample of all TPVs output by TPVTrack was implemented using the two-sample Kolmogorov-Smirnov test between the paired distributions (**Table 2.3.3**). In both hemispheres, TPVs under AIRS can be considered a random sample for all TPVs with respect to amplitude, but TPVs under AIRS cannot be considered a random subset of all TPVs with respect to equivalent radius, as their corresponding distributions are significantly different at the 99% confidence interval.

Differences in equivalent radii between AIRS TPVs and a random subset with the same sample size of TPVTrack TPVs is likely due to the geographic coverage of AIRS swaths over polar regions. For example, a geographic maximum TPV density north of Greenland is apparent from the TPVTrack output. However, this maximum density region lies at the northern latitudinal extent of the AIRS swaths, so most of the basins of these large radius/high amplitude TPVs from this region are not likely to fall entirely within a given AIRS/AMSU swath (**Figure 2.3.1**). This may account for the large discrepancy between TPVTrack TPVs and AIRS TPVs for bins below 300 km in the Northern Hemisphere (**Figure 2.3.5**). Similar yet not immediately obvious geographic effects may also explain differences in bins exceeding ~350–400 km between TPVTrack TPVs and AIRS TPVs for both hemispheres (**Figures 2.3.5 and 2.3.6**).

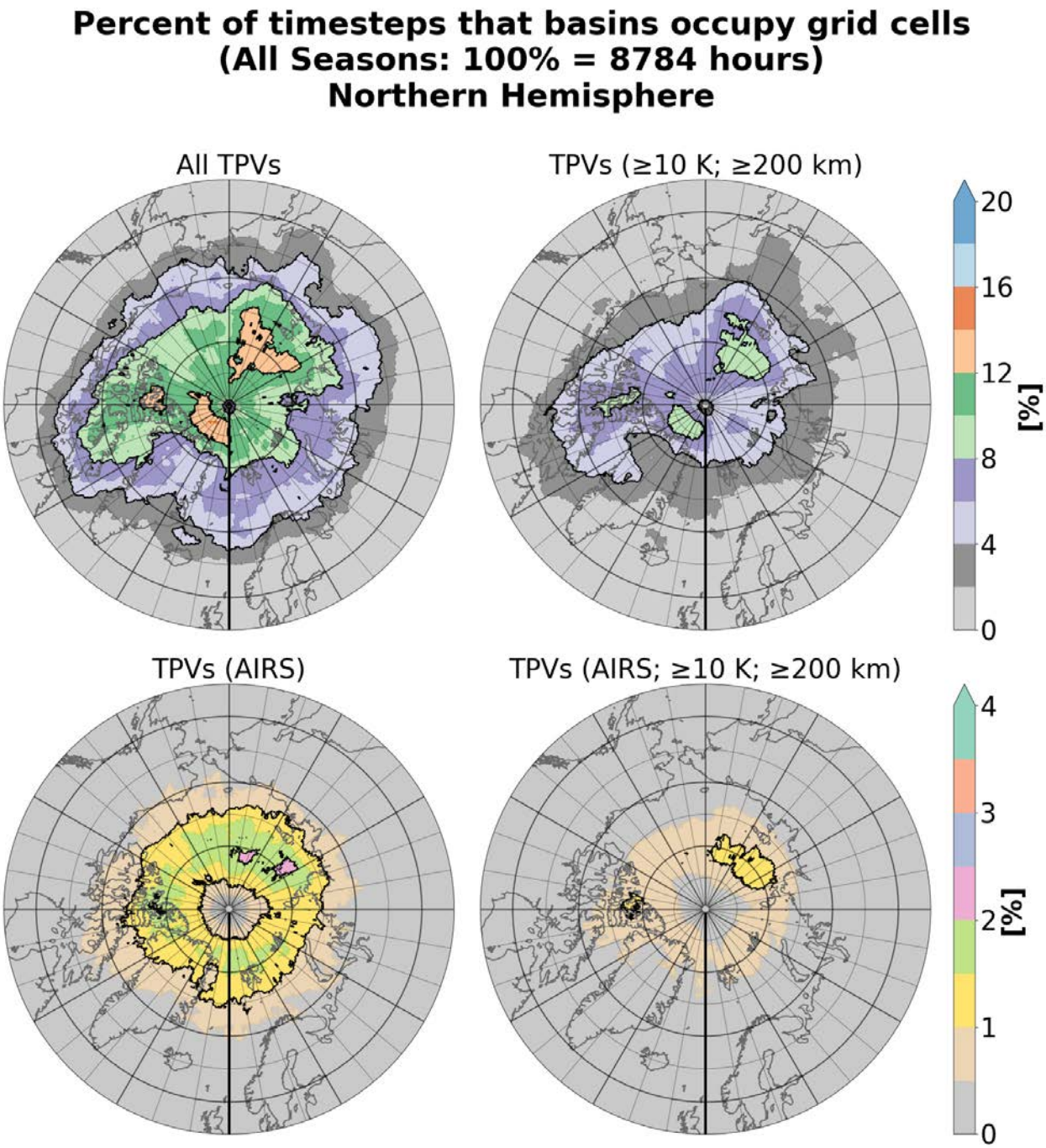

Figure 2.3.1: Geographic distribution of TPV basins in the Northern Hemisphere. TPV basins occupy several grid cells. Illustrated is the percentage of timesteps over one year that each grid spends within a TPV basin. (Top-left) All TPVs output by TPVTrack. (Top-right) As with top-left, except filtered for TPVs satisfying ≥10 K amplitude and ≥200 km equivalent radius. (Bottom-left) As with top-left, except for all AIRS/AMSU-observed TPVs only. (Bottom-right) As with top-right, except for AIRS/AMSU-observed TPVs only. These are the cases selected for this study.

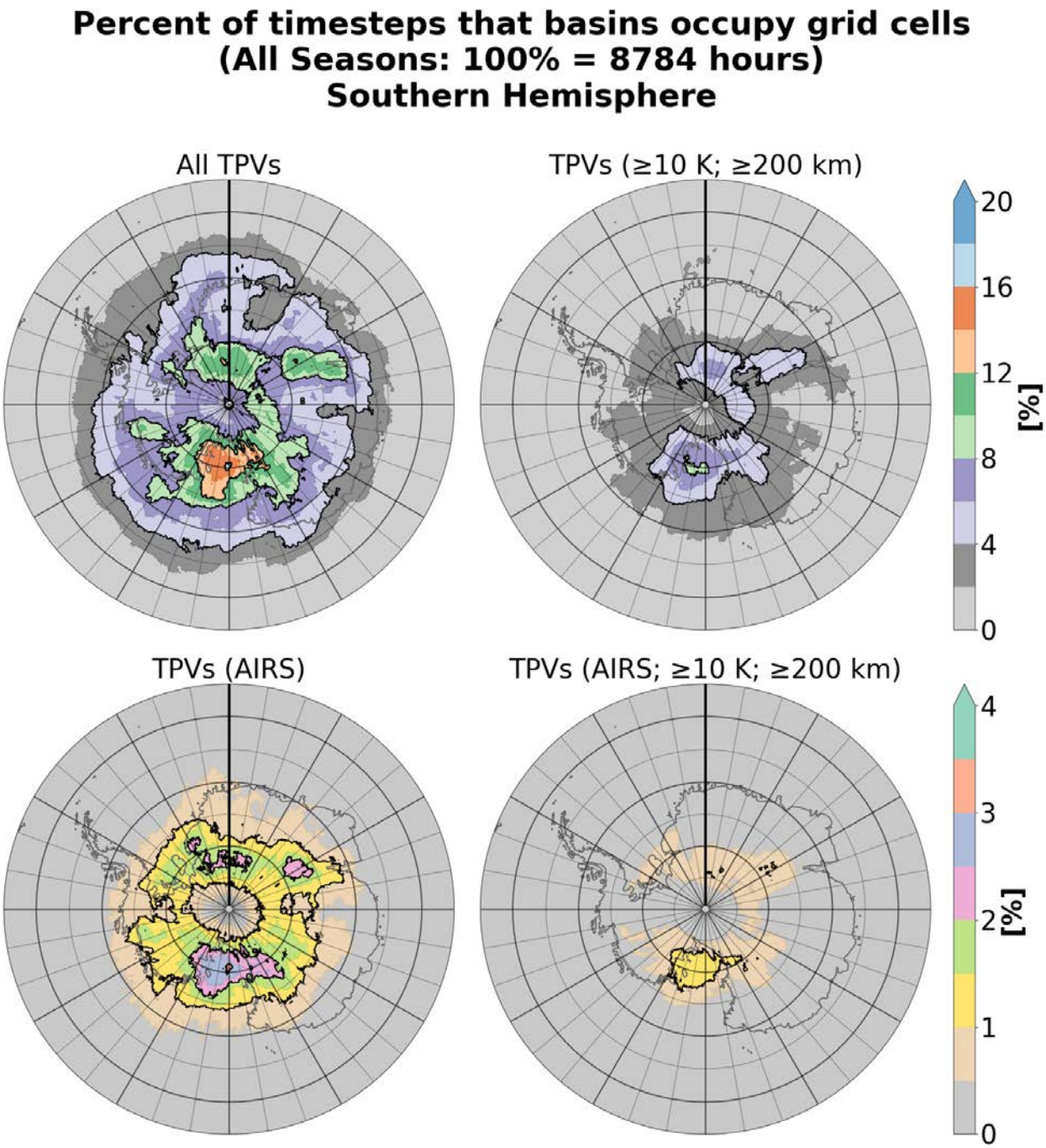

Figure 2.3.2: As with **Figure 2.3.1**, but for the Southern Hemisphere.

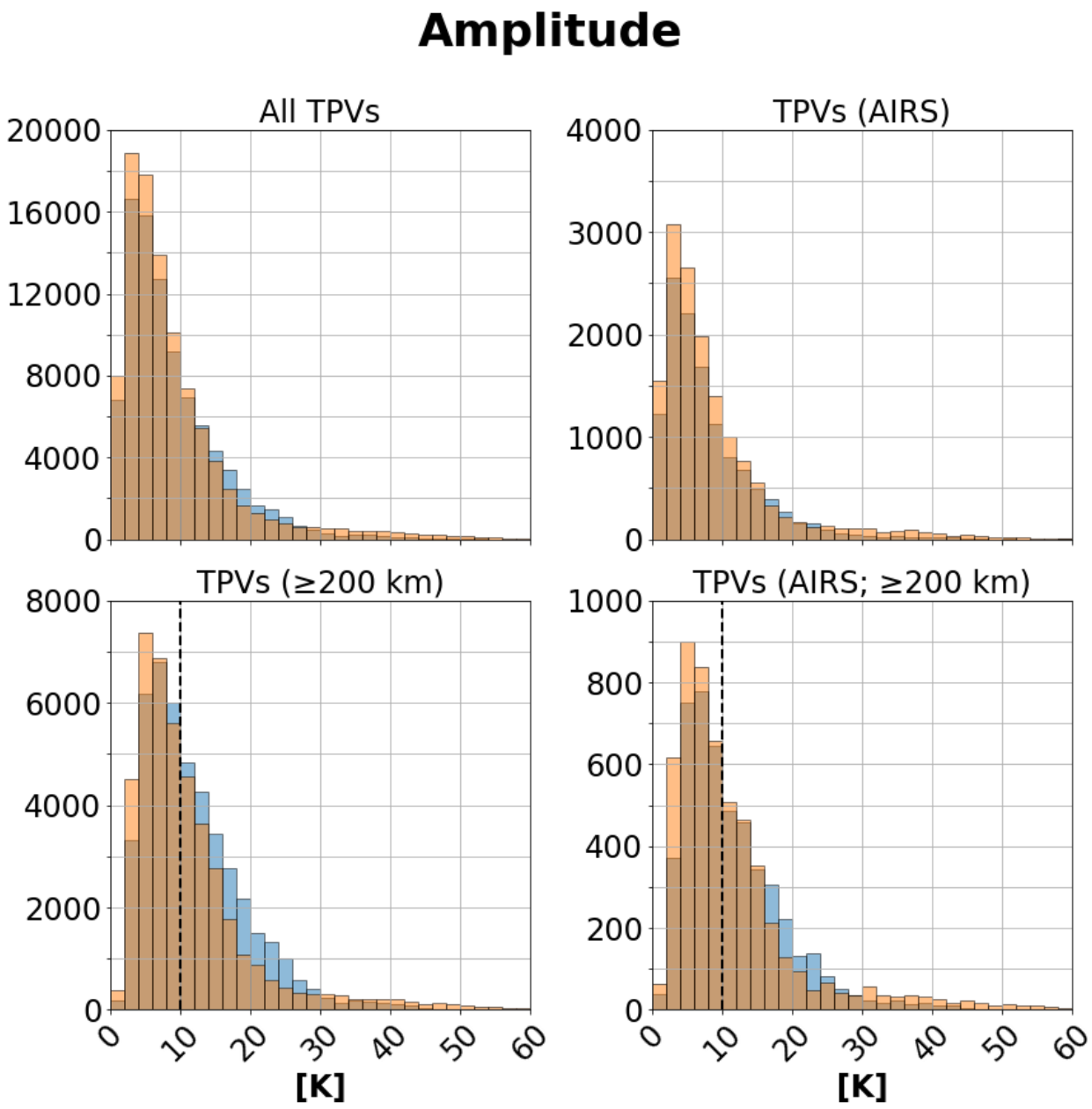

Figure 2.3.3: Amplitude distributions for TPVs output by TPVTrack (left column) and AIRS/AMSU-observed TPVs (right column). Amplitude distributions for TPVs of all equivalent radii (top row) and for only TPVs with equivalent radii of at least 10 K (bottom row). TPV cases with both amplitudes of ≥10 K and equivalent radii of ≥200 km are represented by the portion of the bottom row distributions to the right of the dashed black line. Orange (blue) bars represent the Southern (Northern) Hemisphere. The bin size is 2 K.

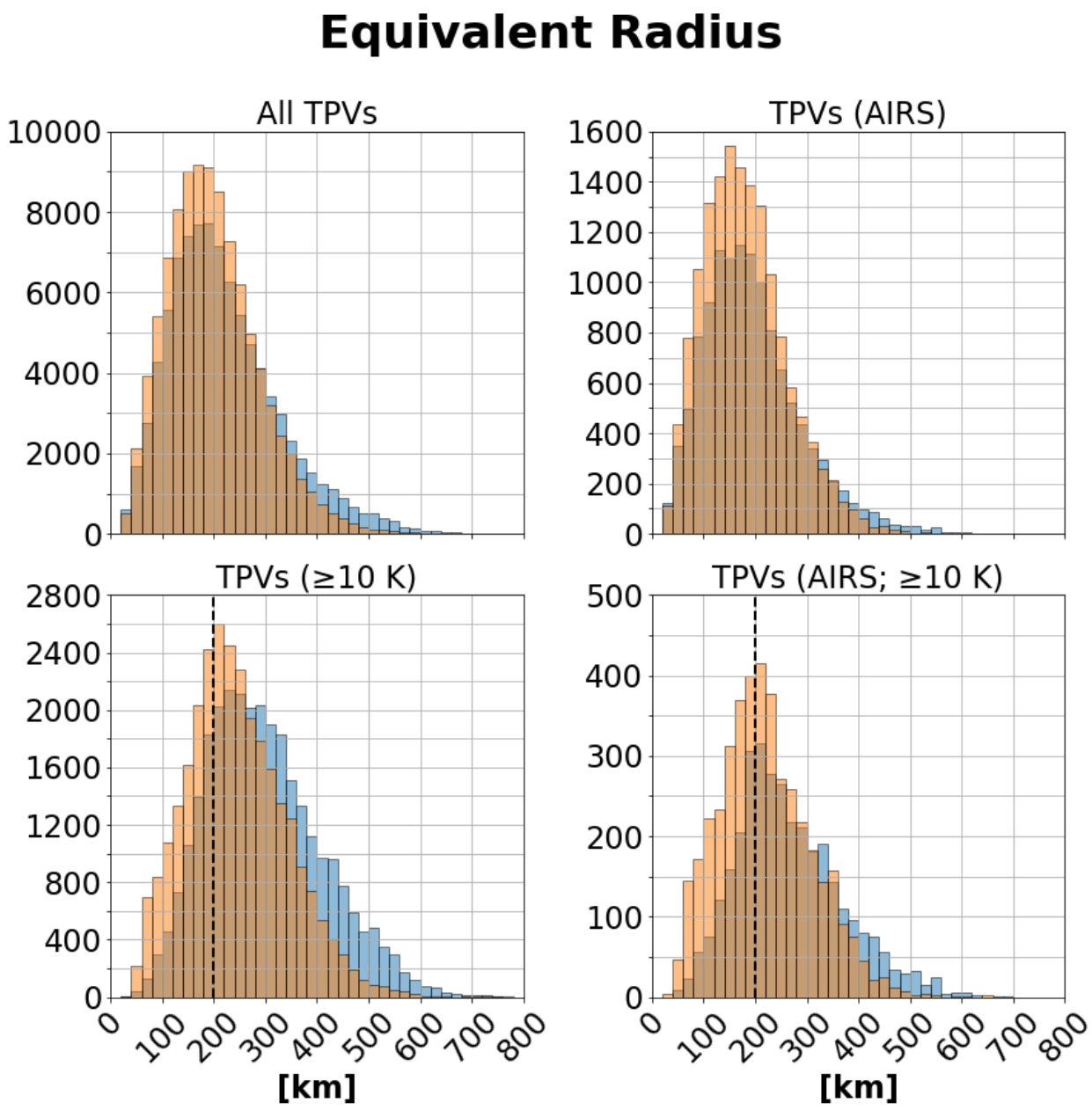

Figure 2.3.4: Equivalent radius distributions for TPVs output by TPVTrack (left column) and AIRS/AMSU-observed TPVs (right column). Equivalent radius distributions for TPVs of all amplitudes (top row) and for only TPVs with amplitudes of at least 10 K (bottom row). TPV cases with both amplitudes of ≥10 K and equivalent radii of ≥200 km are represented by the portion of the bottom row distributions to the right of the dashed black line. Orange (blue) bars represent the Southern (Northern) Hemisphere. The bin size is 20 km.

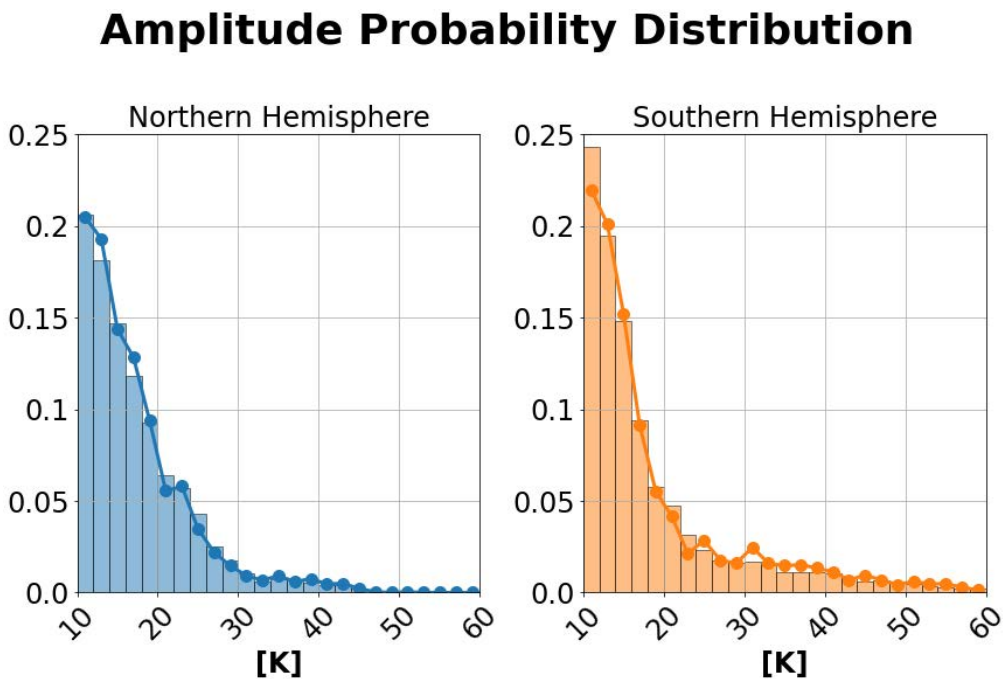

Figure 2.3.5: Histograms for the amplitude of TPVs output by TPVTrack (bars) and AIRS/AMSU-observed TPVs (circles). Only TPVs with both amplitudes of ≥10 K and equivalent radii of ≥200 km are included (this corresponds to the portions of the bottom-row distributions in **Figure 2.3.3** to the right of the respective dashed lines). The bin size is 2 km.

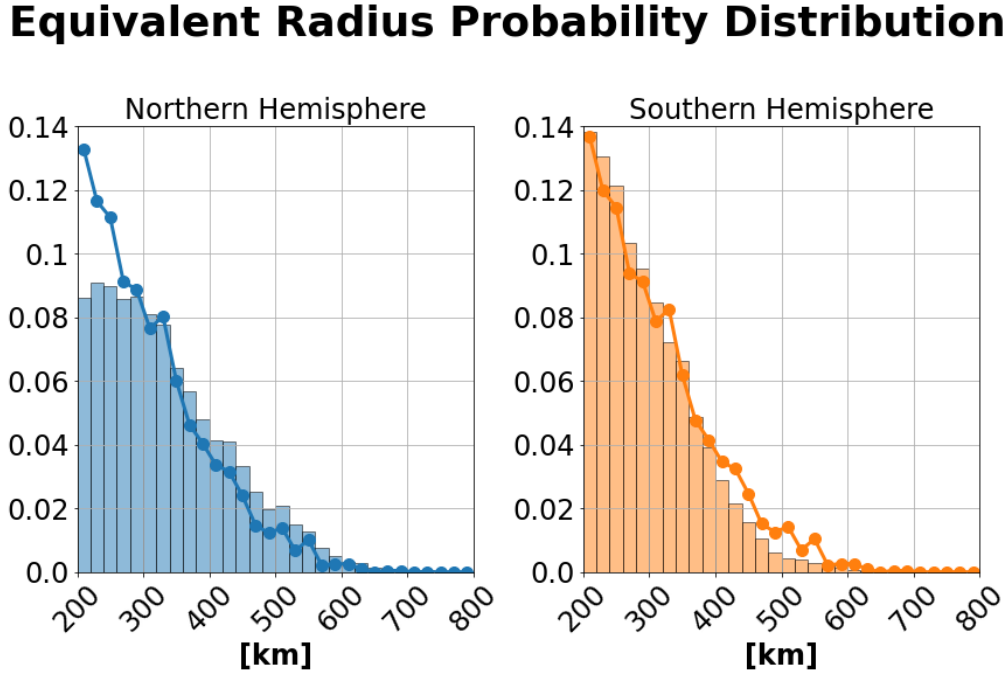

Figure 2.3.6: Histograms for the equivalent radius of TPVs output by TPVTrack (bars) and AIRS/AMSU-observed TPVs (circles). Only TPVs with both amplitudes of ≥10 K and equivalent radii of ≥200 km are included (this corresponds to the portions of the bottom-row distributions in **Figure 2.3.4** to the right of the respective dashed lines). The bin size is 20 km.

Table 2.3.3: (Rows 1–2) The K-S test was performed between the amplitude distribution of TPVs under AIRS and the total distribution off amplitude of all TPVTrack TPVs. The K-S test was likewise performed for equivalent radius distributions row. (Rows 3–4) For robustness, the procedure was then repeated using a Monte Carlo approach by randomly selecting TPVs from the TPVTrack (the number of samples equal to the sample size of the TPVs under AIRS), and then performing the two-sample K-S test between the randomly selected TPVs from TPVTrack and the TPVs under AIRS. This was performed for 10000 iterations, and the average p-values are reported below (the 10000-iteration procedure was itself performed multiple times with consistent results).

K-S test between distribution of TPVs under AIRS and:	Sample Size	p-value (amplitude distributions)	p-value (equivalent radius distributions)
Total population distribution from TPVTrack (NH)	2378 (AIRS) 23451 (All)	0.25	1.0×10^{-20}
Total population distribution from TPVTrack (SH)	2312 (AIRS) 18767 (All)	0.011	3.1×10^{-12}
Subsampled distribution from TPVTrack (NH)	2378 (AIRS) 2378 (randomly selected)	0.45–0.46 (average)	$\sim 1 \times 10^{-9}$ (average)
Subsampled distribution from TPVTrack (SH)	2312 (AIRS) 2312 (randomly selected)	0.11–0.12 (average)	$\sim 5 \times 10^{-6}$ (average)

Section 2.4: Interpolation of cases to a common grid projection

A total of 2378 TPV cases in the Northern Hemisphere and 2312 TPV cases in the Southern Hemisphere have been considered in the analysis. Data for each AIRS granule is reported on a satellite-relative 45 × 30 grid. For each hemisphere, all cases have been interpolated to a common vortex-centered grid with a grid spacing of 50 km in the x- and y-directions, with the +y direction pointing North and ± x direction aligned to the geodesic perpendicular to the y-axis (i.e., false easting and false northing). The common grid extends ± 2000 km in each coordinate direction, resulting in a 41 × 41 grid (**Figure 2.4**; the common grid in projection coordinates is visible in the right panel).

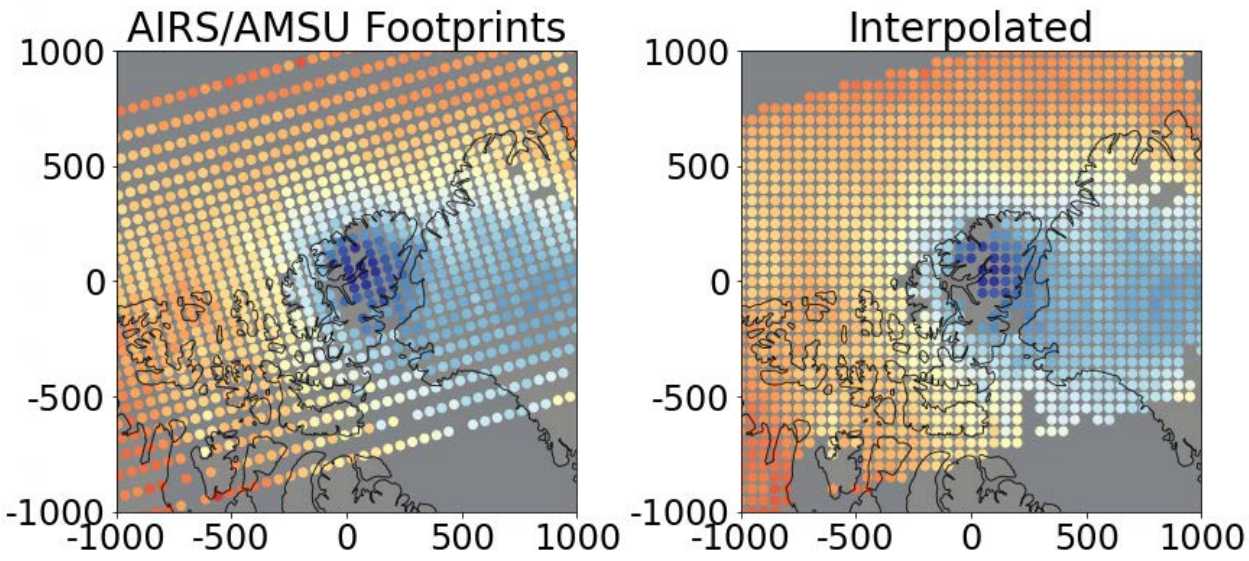

Figure 2.4: A single observed TPV on 2 June 2016 at approximately 12 UTC. Color represents temperature at 500 hPa. Colors range from 245–260 K. (Left) Each dot in the left panel represents a single AIRS/AMSU profile. (Right) Linear barycentric interpolation from AIRS/AMSU profiles to a grid on a TPV-centered oblique stereographic projection. Note that the masked values (missing dots) are propagated through interpolation. Errors of interpolated values are determined using interval propagation.

For each TPV case, interpolation of variables such as temperature from granule profiles to the vortex-centered common grid was performed using a barycentric linear spline. Since the AIRS-relative 45 × 30 grid is non-analytic, methods such as bilinear interpolation were not used.

The AIRS/AMSU V7 L2 Product contains quality control information for each variable (Thrastarson et al. 2020). At a given pressure level, sometimes a retrieval for a given AIRS/AMSU profile fails to converge, or sometimes the location of the profile at that pressure level is below topography, which commonly occurs close to the surface and over high elevations such as Greenland and East Antarctica. Profiles for in these cases are then masked. If one or more of the profiles used to linearly interpolate to a given grid point is masked, then that interpolated point is also masked (**Figure 2.4**).

The AIRS/AMSU V7 L2 Product includes observation errors for some, but not all, variables. The errors of the AIRS/AMSU granule profiles were propagated to the interpolated grid points when applicable. It was assumed that the AIRS/AMSU profiles used to linearly interpolate a variable to a given grid point were close enough in proximity with one another that observation error would also vary linearly between them. With this assumption, interval arithmetic was used to propagate the errors from the profiles to the grid points, which can be referred to as interval propagation. For a variable such as T = temperature with error ΔT, it is assumed that if $(T - \Delta T) \leq T \leq (T + \Delta T)$ for each atmospheric profile involved, then it would also hold true that $(T - \Delta T)_{interpolated} \leq T_{interpolated} \leq (T + \Delta T)_{interpolated}$ for each interpolated grid point. For three-dimensions, the interpolation and error propagation process was iteratively performed in two dimensions at each pressure level for each variable in each TPV case.

Section 2.5: Compositing methods

The resulting two collections (one for each hemisphere) of TPV cases under AIRS/AMSU can each be thought of as a 4-D "cube" with coordinates i = TPV cases sorted chronologically, x = false easting, y = false northing, and p = pressure. False easting and false northing correspond to the x- and y-coordinates for a given map projection with units in "meters", which become equivalent to actual meters if there is no distortion (scale factor $k_0 = 1$).

Direct composites for variables such as temperature were conducted by taking the average for each grid point on the common grid along the "i-axis". Where applicable, error estimates for the direct composites were conducted by taking the root sum squared (RSS) of the error value for each grid point along the "i-axis". Composites for each season (i.e., MAM, JJA, SON, DJF) were also conducted separately.

All instances where a grid point for a given TPV case is masked were simply excluded from the averages. For example, the temperature average for each grid point (x, y, p) was taken to be $T_{\text{average at (x,y,p)}} = \Sigma\, x_{(i \neq \text{NaN})} / N_{(i \neq \text{NaN})}$. Regarding sample size, each grid point can have a theoretical maximum of N = 2378 samples in the Northern Hemisphere (2312 samples in the Southern Hemisphere). However, this would no longer be true if that data point is missing for one or more TPV cases, so the actual number of TPV samples for each grid point would be $N \leq$ 2378 samples ($N \leq 2312$ samples).

Anomaly composites were conducted by first calculating the background for each case. This was done by averaging over a 15-day window (t = –7 days to t = +7 days) centered on each TPV case at t = 0 days (**Figures 2.5.1 and 2.5.2**) and doing so for all cases (i.e., each TPV case has a unique background). Background errors were taken to be the RSS of the variable errors over the 15 days. Anomalies were then taken by subtracting from each TPV case its corresponding background (**Figure 2.5.3**). Anomaly errors were computed by taking the RSS of the variable error of the TPV case and the variable error of background.

In addition to the anomalies, changes relative to the background are also studied for some variables (e.g., mixing ratio). The relative change (or percent change if multiplied by 100%) for variable x with error Δx is taken to be:

$$\text{Relative change}\left(x,\, x_{background}\right) = \frac{x - x_{background}}{x_{background}}. \tag{4}$$

and the relative change error is:

$$\Delta Relative\ change\left(x,\, x_{background}\right) = |x| \sqrt{\left(\frac{\Delta x}{x}\right)^2 + \left(\frac{\Delta x_{background}}{x_{background}}\right)^2}. \tag{5}$$

In the following chapter, the primary focus will be on TPV anomalies and relative change, while direct composites will see very limited treatment. However, direct composite averages for TPVs can be visited in Appendix A.

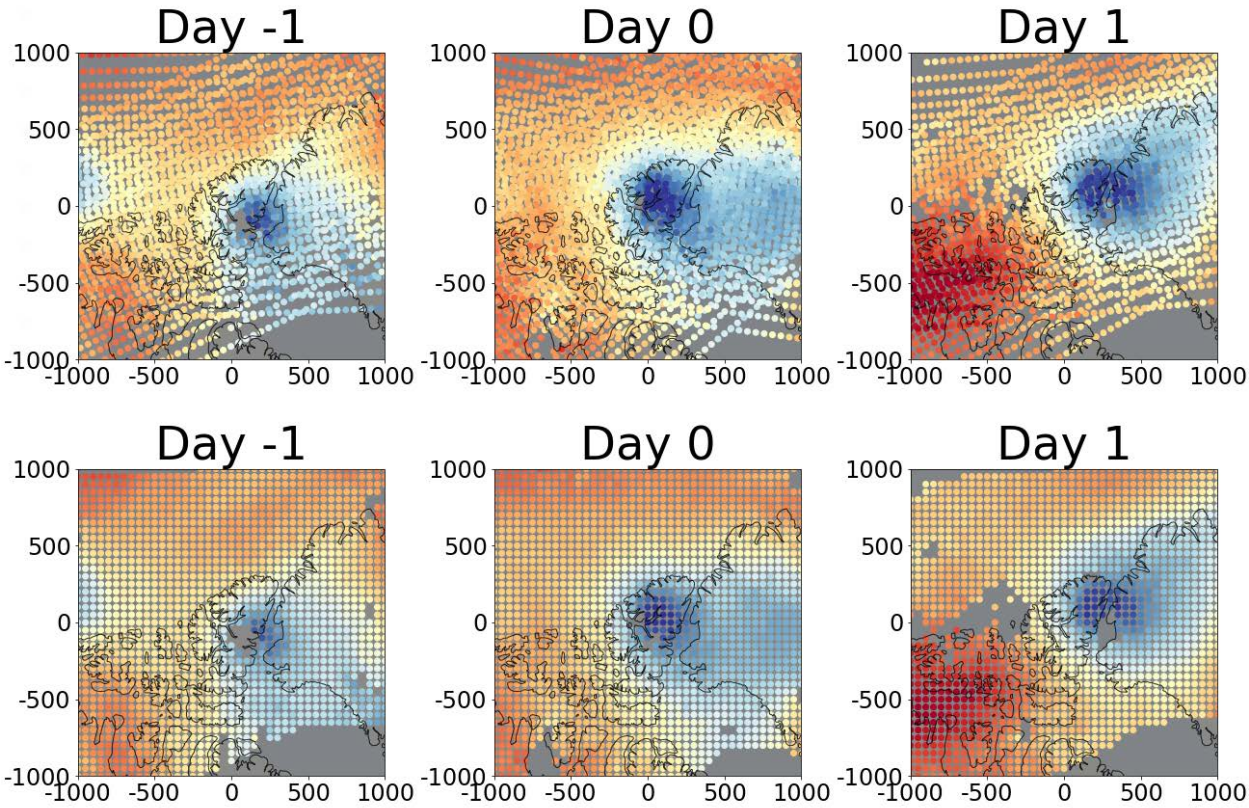

Figure 2.5.1: The background for each TPV case is calculated from the 2–3 closest Aqua overpasses (to increase coverage over the domain) in approximately 24-hour intervals from -7 days to +7 days; only -1 days to +1 days are illustrated. (Top-row) AIRS/AMSU profiles prior to the interpolation of the 2–3 successive overpasses for days -1 to +1. (Bottom row) Days -1 to +1 after linear barycentric interpolation. Color represents temperature at 500 hPa. Colors range from 245–260 K. For each day, each overpass is interpolated separately, and then the 2–3 overpasses of that day are averaged together. Likewise, for each day, errors are interval-propagated for each overpass separately in the interpolation step. Then, the root sum squared (RSS) is taken across the 2–3 successive overpasses of that day to reach the final error value for each grid point for that day. *Note: TPVs observed during the ascending (descending) node of Aqua will have their backgrounds calculated using only granules from the ascending (descending) node on the other days over the 15-day window. This becomes less relevant for TPVs close to the poles (i.e., at the transition "between" the ascending and descending nodes).*

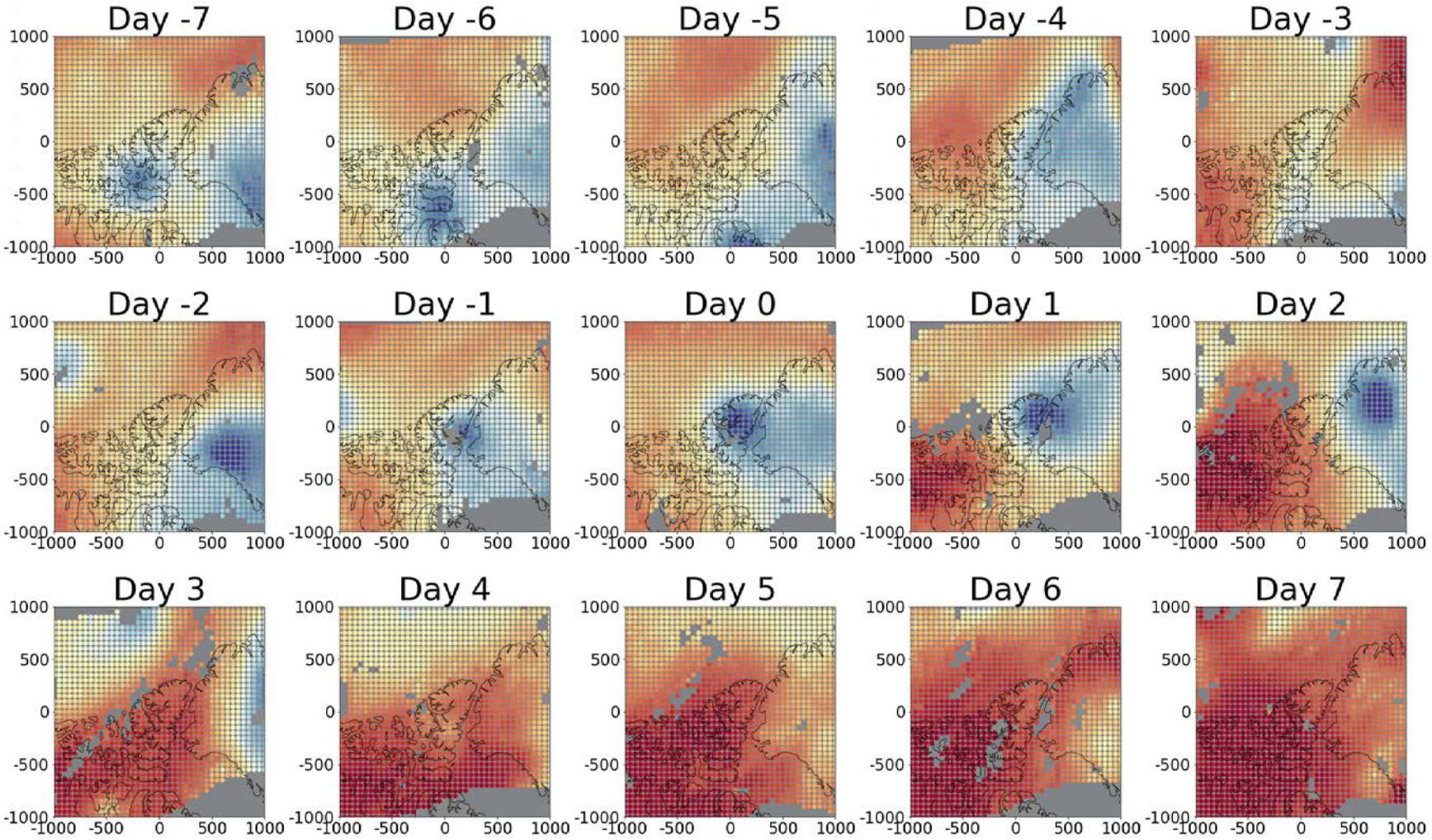

Figure 2.5.2: As with **Figure 2.5.1**, except only interpolated values are shown for days -7 to +7. Unlike the averaging performed in **Figure 2.5.1**, averaging across this 15-day window requires existing values at all timesteps (no masked values) at each grid point. This is done to keep a consistent frequency response across all case anomalies. This comes with the trade-off of reducing the number samples per grid point for the anomaly calculations. Dates here range from 26 May 2016 to 9 June 2016. Each day in this specific example contains data collected over a 1.7–3.3-hour period centered on 12 UTC.

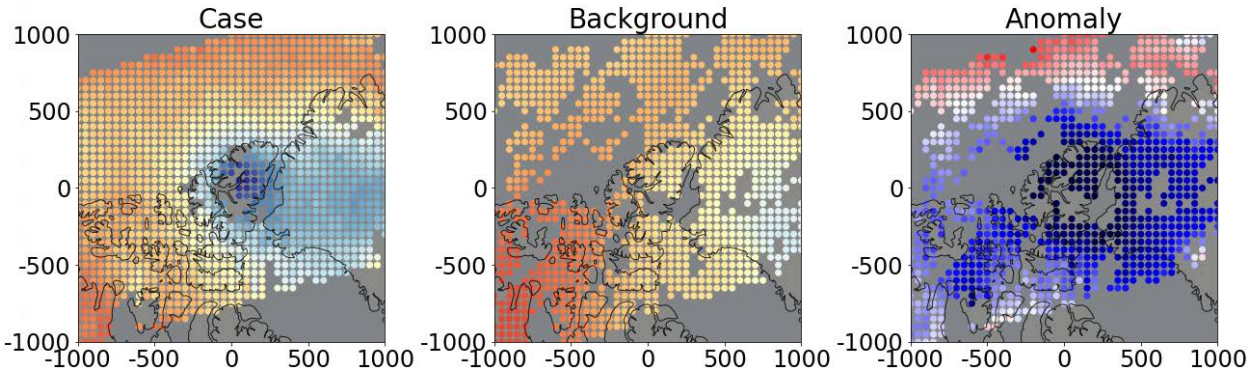

Figure 2.5.3: (Left) Linear barycentric interpolation to a grid of temperature values of a single TPV case on 2 June 2016 at approximately 12 UTC. Color represents temperature at 500 hPa, ranging from 245–260 K. (Center) Averaged background calculated from the 15-day window illustrated in **Figure 2.5.2**. (Right) Temperature anomaly at 500 hPa. Colors range from -5 K to 5 K.

Chapter 3

Results

Chapter 3 covers the resultant TPV composites under AIRS/AMSU over the one-year observation period from 1 September 2015 to 31 August 2016. The temperature and dewpoint profiles of the TPV centers will first be reported and compared with the corresponding profiles in Cavallo and Hakim (2010). This will be followed by TPV vertical cross-sections for temperature, water vapor mass mixing ratio (referred hereinafter as simply "mixing ratio"), relative humidity, and ozone volume mixing ratio (ozone VMR). Composites will also be presented for each season separately for each variable prior to being presented for the year-long study period. While both horizontal and vertical variability of TPV structure will be illustrated, emphasis will be placed on resultant composite vertical structure.

Two vertical grids are used in displaying variables from the AIRS/AMSU V6/V7 L2 Standard Product. All variables are available at constant pressure levels (e.g., 500 hPa). Temperature and relative humidity are available only as level quantities. Some variables such as mixing ratio and ozone VMR are given as layers between levels as the default (e.g., 400–500 hPa); the level quantities given in the product are vertical interpolations from the original layer quantities. A side effect is that level quantities sometimes exhibit strange behavior of mixing ratios close to the surface (Thrastarson et al. 2020).

Direct composite (non-anomaly) averages for TPV temperature, mixing ratio, relative humidity, and ozone VMR are not included in the results of this study because they are not the primary focus for comparison to past literature; however, they are presented in Appendix A. In this study, mixing ratio and ozone VMR anomalies will be illustrated as layer quantities. Temperature and relative humidity anomalies will be expressed in level quantities. The vertical levels used in the AIRS/AMSU product, which are also the boundaries for layers, are given on all mandatory pressure levels from 1000 hPa to 1.0 hPa, with additional levels at 600 hPa, 15 hPa, and 1.5 hPa.

Certain caveats must be noted regarding certain variables. AIRS is not sensitive to mixing ratios below ~0.015–0.02 g/kg (Thrastarson et al. 2020). This consequently results in a degradation of water vapor retrievals beginning at altitudes above the 300 hPa level, and there is no retrieval anymore once reaching 100 hPa. Moreover, mixing ratio profiles containing errors exceeding half of the mixing ratio at any layer needed to be removed prior to compositing analysis as recommended by Thrastarson et al. (2020). Mixing ratio errors exceeding half of the mixing ratio value imply that unphysical negative mixing ratios lie within the margin of error.

AIRS also loses reliability for ozone VMRs below 100 parts per billion volume (ppbv) as well as at altitudes lower than the 300 hPa level. Ozone retrievals also lose accuracy when surface skin temperatures are less than 250 K; such profiles needed to be removed before compositing. In addition, there may be biases of ozone volume mixing ratio between approximately 80–300 hPa that have yet to be characterized (Thrastarson et al. 2020).

Previous studies of composite TPV anomaly structure have been conducted in the Canadian Arctic using a forecast model (Cavallo and Hakim 2010) and ground-based remote-sensing observations in Summit Station, Greenland (Borg, Cavallo, and Turner 2020). **Table 3** is displayed here for reference and summarizes the temperature and relative humidity anomalies compiled from both studies.

When conducting temperature and water vapor composites, only sample sizes of $N \geq 20$ will be considered. For $N < 20$, errors for composite temperature and temperature anomaly begin to exceed ~0.5–0.6 K, errors for composite mixing ratio and mixing ratio anomaly begin to exceed ~0.1–0.3 g/kg, and errors for composite mixing ratio relative change begin to exceed ~5–10%, depending on season and hemisphere. The minimum sample size is also applied to composite ozone (Appendix A). For composite ozone anomaly and relative change, no minimum sample size is implemented because sample sizes for these composites are very low.

Table 3: Temperature (T) and relative humidity (RH) anomalies at the TPV center are compiled here from Figures 6b, 9a, 9d, and 14a–d from Cavallo and Hakim (2010), referred here as CH10, and Figure 9a–b from Borg, Cavallo, and Turner (2020), referred here as BTC20. Only vertical extents, and not horizontal (CH10) nor temporal (BCT20) extents, at the vortex center are listed here. The heights above ground level for the time-height composites in BCT20 were approximated to pressure levels using the elevation of Summit Station, Greenland, and geopotential height data from AIRS/AMSU (not shown).

In the Canadian Arctic forecast model TPV composites (CH10), the positive (+) and negative (–) T and RH anomalies are comparable between the annual and summer, except that the +RH maximum increases approximately twofold in the summer. The winter ±T and ±RH anomaly extrema are relatively weaker than those of the annual and summer composites. Anomaly extrema are also generally lower in altitude in the winter months.

The Summit Station TPV composite (BCT20) indicates weaker ±T anomaly extrema than those in CH10. The –RH anomaly minima between the BCT20 and CH10 annual composites are similar in magnitude; the +RH anomaly present in the CH10 composites is absent in the BCT20 composite. Both the –T and the –RH anomaly minima are higher in altitude in BCT20 than those in CH10.

	Annual (BCT20)	Annual (CH10)	Summer (CH10)	Winter (CH10)
+T Anomaly	~ +3 K at ~250 hPa	+5.5 K at 250 hPa	+6.5 K at 200 hPa	+2.5 K at 300 hPa
–T Anomaly	slightly <–2 K at ~500 hPa	–8.5 K at 700 hPa	< –8 K between ~500–850 hPa	–6 K to –7 K at ~675–1000 hPa
–RH Anomaly	~ –25% between ~200–250 hPa	< –25% at 375 hPa	< –27% between ~275–350 hPa	< –18% near ~400–450 hPa
+RH Anomaly	Absent	+12–15% at 800 hPa	+24–27% near ~750–800 hPa	+3–6% around ~800 hPa

Section 3.1: Vortex-centered and background temperature and dewpoint profiles

The composite temperature and dewpoint profiles from AIRS/AMSU of the TPV vortex centers are presented separately for each season (i.e., MAM, JJA, SON, DJF) in the Northern (**Figure 3.1.1**) and Southern (**Figure 3.1.2**) Hemispheres over the one-year study period. Dewpoints were calculated from the AIRS/AMSU saturation mixing ratios using Equation 10 from Bolton (1980). Temperature and dewpoint profiles from Figure 7 in Cavallo and Hakim (2010) are also superimposed in **Figure 3.1.1** for comparison.

The TPV-centered AIRS/AMSU temperature profiles are generally consistent with Cavallo and Hakim (2010) for the summer season and from the 400 hPa level and upwards for the spring and fall seasons, with differences of no more than 1–2 K. AIRS/AMSU temperature vortex-center profiles are comparatively warmer elsewhere, except for the winter season in which they are comparatively colder for altitudes at and above the 500 hPa level.

The comparison of background temperature profiles under AIRS/AMSU are generally either consistent with or slightly cooler than those in Cavallo and Hakim (2010) for the spring, fall, and from the 400 hPa level downwards in the winter. The largest differences occur in the summer at nearly all levels and in the winter at altitudes above the 400 hPa level.

Comparisons between the vortex-centered dewpoint profiles of AIRS/AMSU and Cavallo and Hakim (2010) are consistent in the summer at the 500 hPa level and below, as well as 400–500 hPa in the wintertime. Elsewhere, the AIRS/AMSU TPV-center composite profiles have generally higher dewpoints than those in Cavallo and Hakim (2010) at altitudes below the 300 hPa or 400 hPa level.

The AIRS/AMSU composite background dewpoint profiles generally have slightly lower dewpoints than those in Cavallo and Hakim (2010) with up to a ~5 K difference, with exceptions at altitudes below the 500 hPa level in the autumn and above the 200 hPa level in the winter. No comparison can be made for the summer background dewpoint profile. The background dewpoint profiles agree the most in the winter season and the least in the spring season.

Southern Hemisphere TPV-centered and background profiles are shown in **Figure 3.1.2**. Temperatures and dewpoints for the TPV centers and backgrounds are generally lower than that of the Northern Hemisphere throughout the entire profile. Differences between hemispheres are generally greatest in the lower (upper) atmosphere in the summer (spring). Differences are smallest between hemispheres in the lower (upper) atmosphere in the winter (autumn).

Total composites of AIRS/AMSU temperature and dewpoint profiles for TPV centers and the background are given in **Figure 3.1.3**, with superimposed profiles adapted from Figure 6a in Cavallo and Hakim (2010) for the Northern Hemisphere. Samples between seasons are not equally distributed, resulting in some seasons being more heavily weighted than others (this will be treated further in later sections).

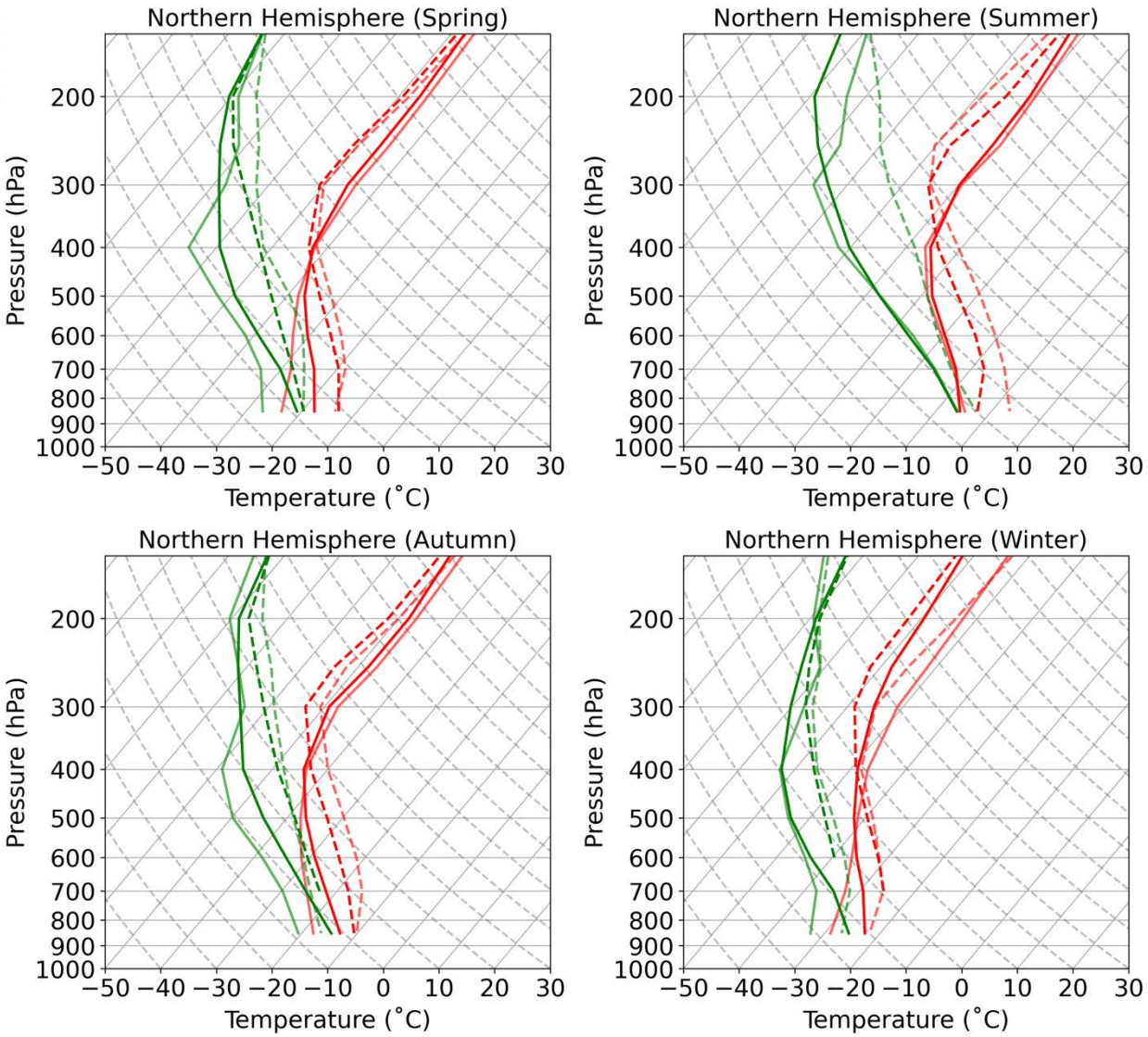

Figure 3.1.1: Skew-T log-p diagrams for composite profiles for the center of the TPV (solid) and the background (dashed) for each season in the Northern Hemisphere. Semi-transparent lines are adapted from Figure 7 in Cavallo and Hakim (2010). Superimposed opaque lines represent the TPVs in this study under under AIRS/AMSU. Only pressure levels at 150, 200, 250, 300, 400, 500, 600, 700, and 850 hPa are included. Data points with sample sizes of less than 20 were not plotted. Note that this results in some gaps in the AIRS/AMSU profiles, including the summer background dewpoint profile being entirely absent.

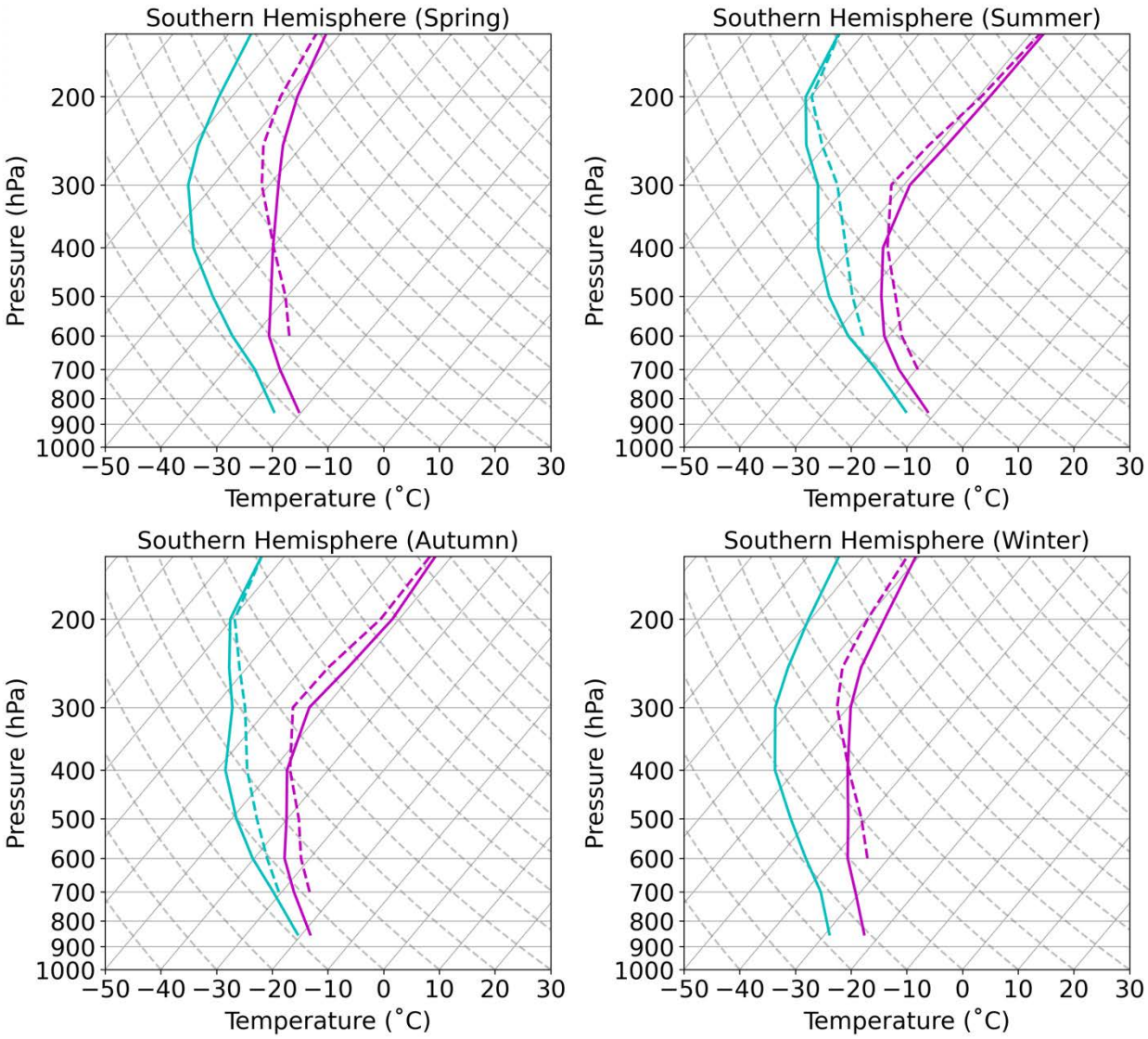

Figure 3.1.2: Skew-T log-p diagrams for composite profiles under AIRS/AMSU for the center of the TPV (solid) and the background (dashed) for each season in the Southern Hemisphere. Only pressure levels at 150, 200, 250, 300, 400, 500, 600, 700, and 850 hPa are included. Data points with sample sizes of less than 20 were not plotted, resulting in gaps, particularly for the background profiles.

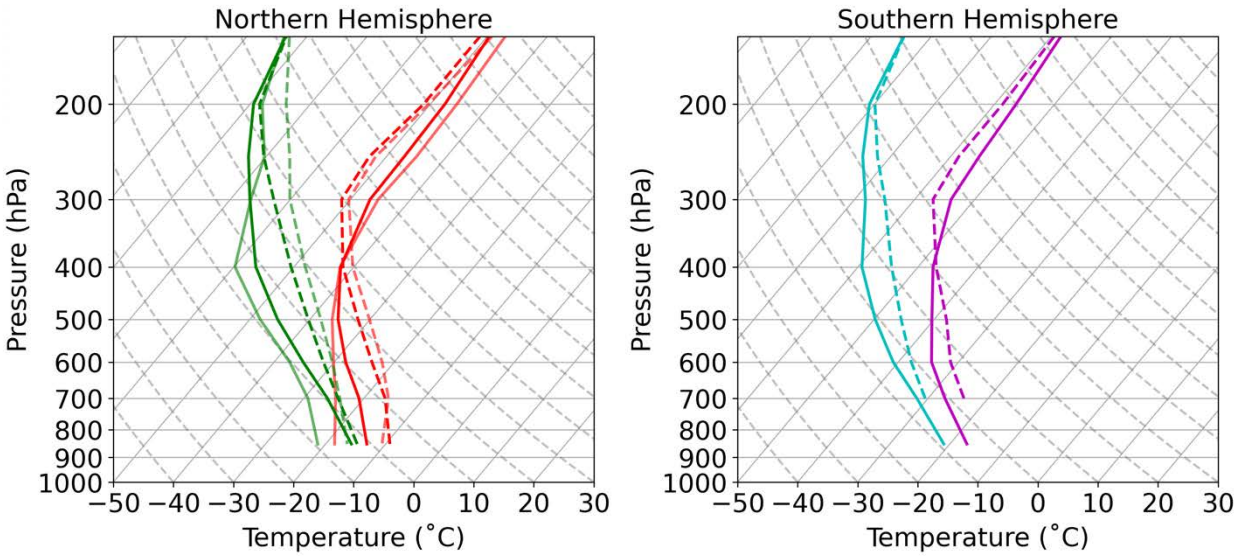

Figure 3.1.3: Skew-T log-p diagrams for composite profiles under AIRS/AMSU averaged over the 1-year-long study period for the center of the TPV (solid) and the background (dashed). Semi-transparent lines are adapted from Figure 6a in Cavallo and Hakim (2010). Only pressure levels at 150, 200, 250, 300, 400, 500, 600, 700, and 850 hPa are included. Data points with sample sizes of less than 20 are not plotted.

Section 3.2: Temperature anomalies

Temperature anomalies from a 15-day mean background for each season and hemisphere are shown in **Figure 3.2.1**. TPV temperature anomalies have the characteristic "dipole" with a cold (warm) anomaly in the troposphere (stratosphere). In the Northern Hemisphere, the magnitudes of the warm temperature anomalies are greatest in the summer, followed by autumn, spring, then winter (**Figures 3.2.1 and 3.2.7**).

The cold anomaly magnitudes follow the same pattern, except autumn and spring have approximately the same magnitudes. The maximum warm temperature anomaly resides at the 250 hPa level for summer, autumn, and winter, and closer to 300 hPa in the spring. The minimum cold temperature anomalies reside at the 600 hPa level for the summer and autumn seasons. For spring, the level of the cold anomaly minimum is not distinguishable between the 700, 850, and 950 hPa pressure levels, as their errors overlap. The winter cold anomaly minimum is also not discernible between the 600 hPa and 700 hPa levels; there is insufficient information at altitudes below the 700 hPa level in the winter. The temperature anomalies cross 0 K near the 400 hPa level for all seasons.

In the Southern Hemisphere, the magnitudes of the warm temperature anomalies lie between +3 K and +4 K for all seasons (**Figures 3.2.1(b) and 3.2.7**). The warm temperature anomaly maximum resides at the 250 hPa for the autumn, winter, and spring, and closer to 300 hPa in the summer. The vertical profiles of the cold temperature anomalies with sample sizes of $N \geq 10$ indicate increasingly cold anomalies toward the surface for all seasons except autumn; however, the cold anomalies between the 600 hPa and 700 hPa levels are not distinguishable from one another in the summer and autumn seasons. The lowest temperature anomalies are found in the spring season.

Temperature anomaly sample sizes per x–y–pressure-level grid point are not distributed evenly between seasons. In the Northern Hemisphere, there are fewer samples in the winter than the other seasons (**Figure 3.2.2(a)**). In the Southern Hemisphere, there are fewer samples in the winter and spring than the summer and autumn (**Figure 3.2.2(b)**). Temperature anomaly errors increase rapidly when approaching the surface, beginning at ~700–850 hPa in the Northern Hemisphere (**Figure 3.2.3(a)**) and ~600–700 hPa in the Southern Hemisphere (**Figure 3.2.3(b)**). The greatest discernibility (i.e., largest occurrence of non-overlapping error bars) between the TPV temperature and the background temperature are collocated with the temperature anomaly extrema in both hemispheres (**Figure 3.2.4**).

The temperature anomaly composites for the full year-long study period in the Northern and Southern Hemispheres are shown in **Figure 3.3.5** with corresponding sample size in **Figure 3.3.6**. It is noted that the sample sizes for each grid point are not evenly distributed between seasons for both hemispheres (**Figure 3.2.2**). The spring, summer, and autumn seasons contribute more to the Northern Hemisphere TPV composite than the winter season; likewise, the summer and autumn seasons of the Southern Hemisphere TPV contribute more than the winter and spring seasons. Overall, temperature anomalies in Northern Hemisphere TPVs have larger magnitudes than Southern Hemisphere TPVs (**Figure 3.2.5** and **Figure 3.2.7**). The range of TPV temperature anomaly extrema in the Northern Hemisphere are also larger between seasons than those of the Southern Hemisphere.

The negative temperature anomaly minima of Northern Hemisphere TPVs under AIRS/AMSU are generally lesser in magnitude than those in Cavallo and Hakim (2010) for the respective annual, winter, and summer composites; and greater in magnitude than those in Borg, Cavallo, and Turner (2020) for the annual composite. The warm anomaly maximum of the Northern Hemisphere TPV composite is approximately equal to that in Cavallo and Hakim (2010) and of greater magnitude than that in Borg, Cavallo, and Turner (2020) for the annual composite; the warm anomaly maxima for the summer and winter seasons are of greater magnitude than those in Cavallo and Hakim (2010).

(a)

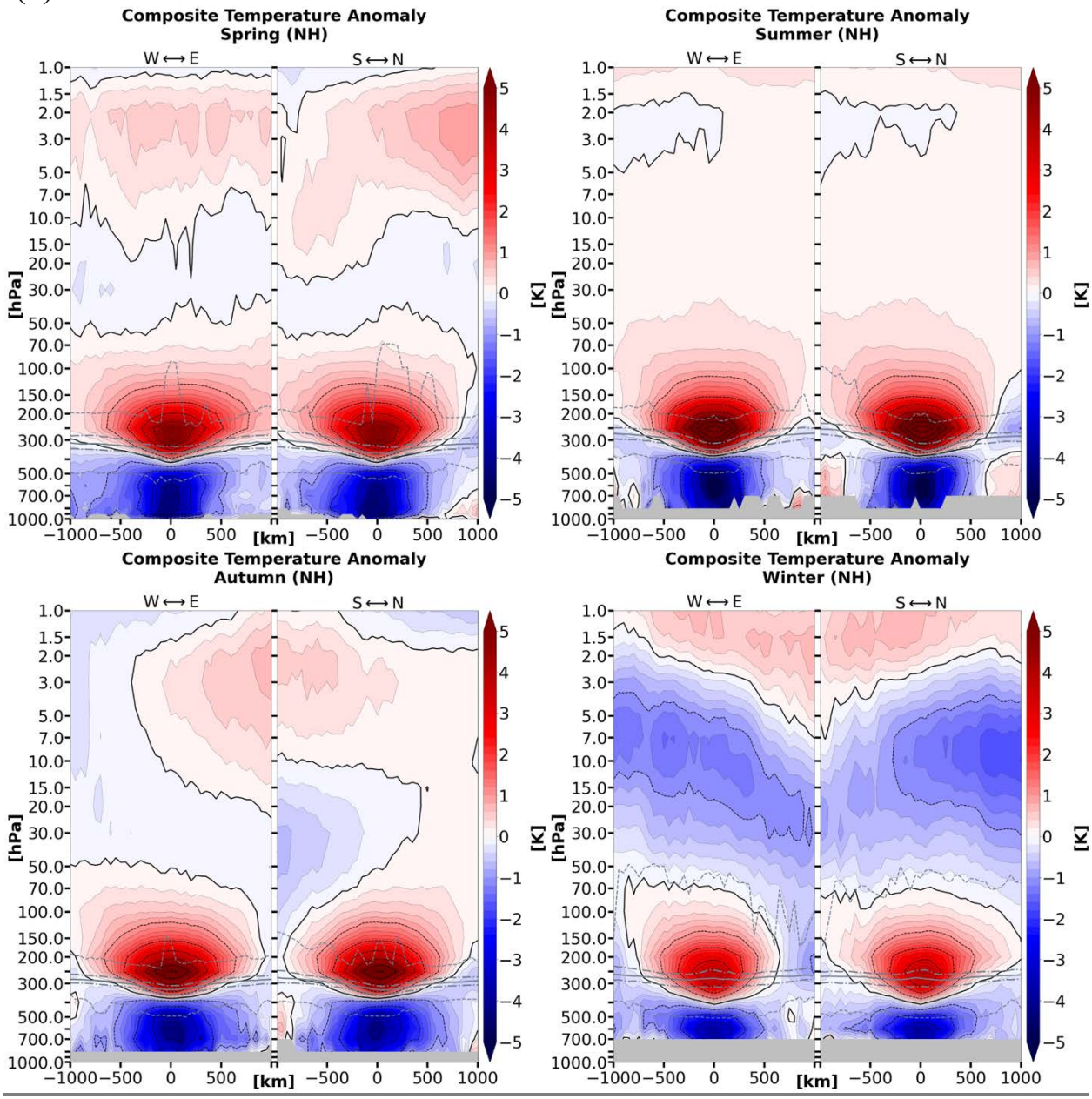

Figure 3.2.1: Composite temperature anomaly cross-sections by season for TPVs in (a) the Northern Hemisphere and (b) the Southern Hemisphere under AIRS/AMSU. The left half of each seasonal panel is oriented along a geodesic of the ellipsoid (and not along latitude lines), converging to the west-to-east direction at the origin. The geodesic in right half of each panel simplifies to the south-to-north direction (along longitude lines). Anomalies are with respect to a 15-day mean background. Data points with less than 20 samples are excluded. The grey solid line indicates the thermal tropopause median; the long (short) dashed grey lines indicate the thermal tropopause interquartile range (minima and maxima).

(b)

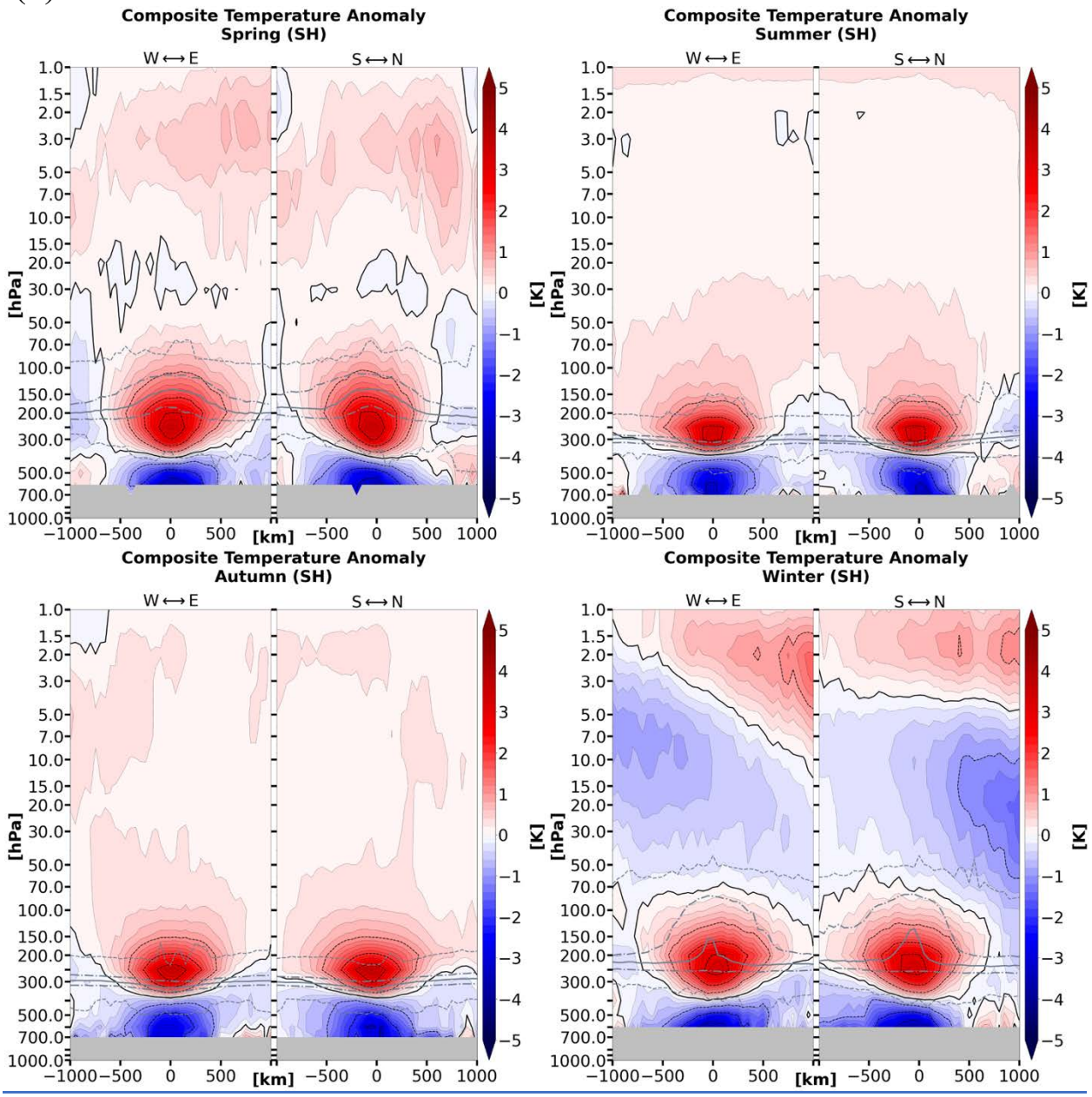

Figure 3.2.1 (continued)

(a)

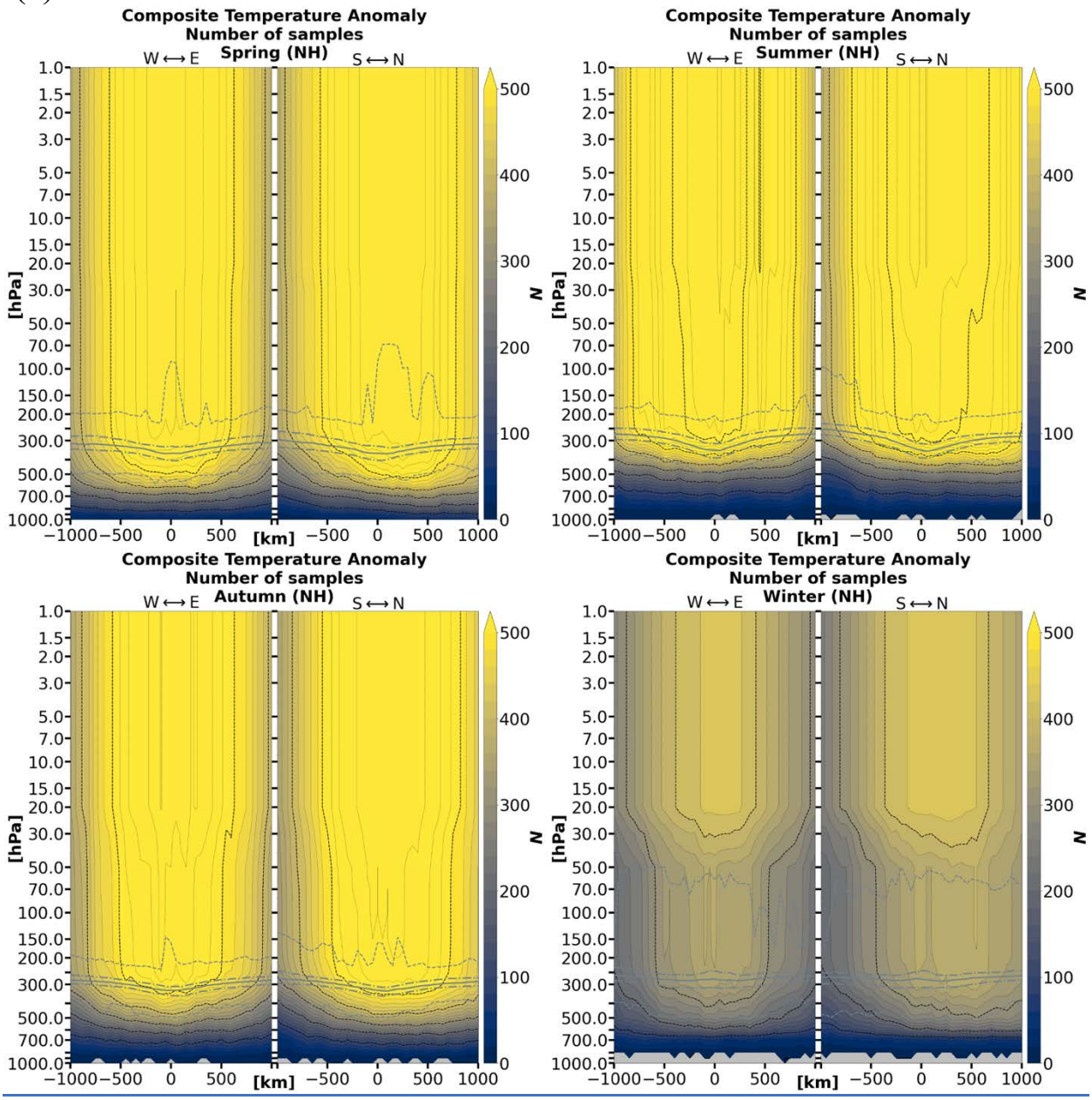

Figure 3.2.2: Sample size for each x–y–pressure-level grid point corresponding to (a) the Northern Hemisphere and (b) the Southern Hemisphere TPV temperature anomalies in **Figure 3.2.1**. Note that areas where N < 20 are masked in **Figures 3.2.1, 3.2.3, and 3.2.4**. The grey solid line indicates the thermal tropopause median; the long (short) dashed grey lines indicate the thermal tropopause interquartile range (minima and maxima).

(b)

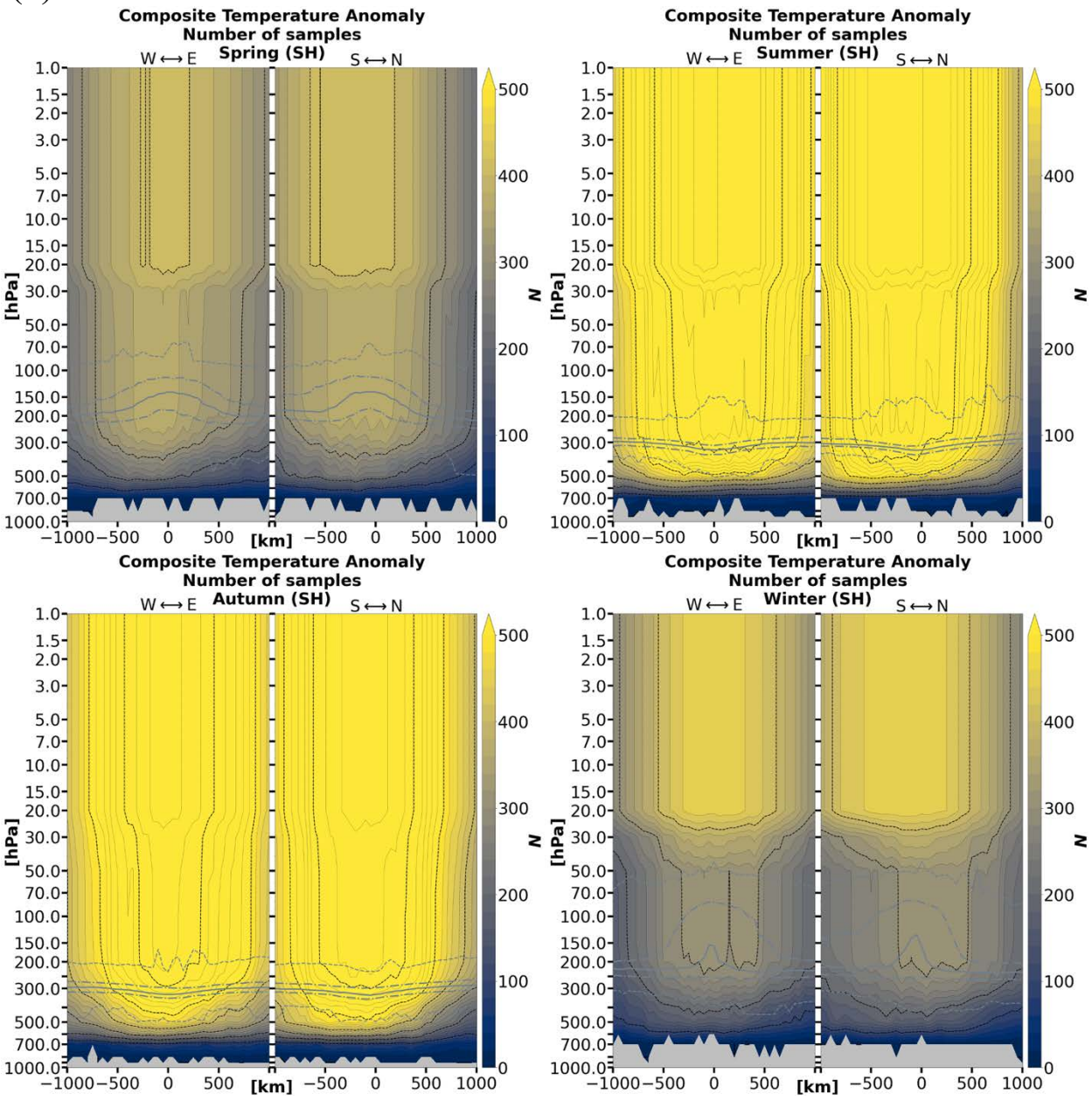

Figure 3.2.2 (continued)

(a)

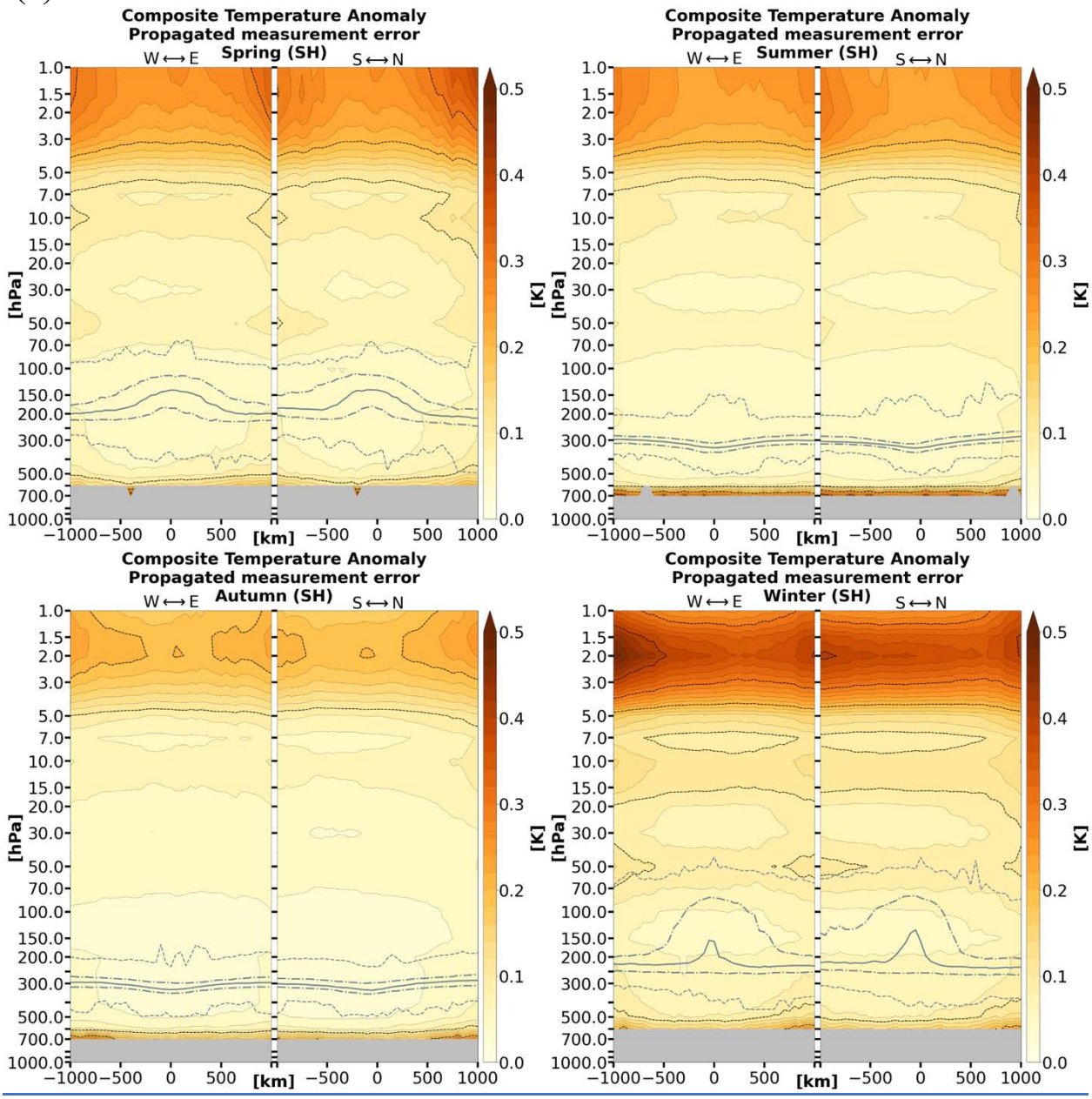

Figure 3.2.3: Cross-sections of (a) Northern Hemisphere and (b) Southern Hemisphere TPV composite temperature anomaly errors for each x–y–pressure-level grid point corresponding to the anomalies in **Figure 3.2.1.** Data points with less than 20 samples are excluded. The grey solid line indicates the thermal tropopause median; the long (short) dashed grey lines indicate the thermal tropopause interquartile range (minima and maxima).

(b)

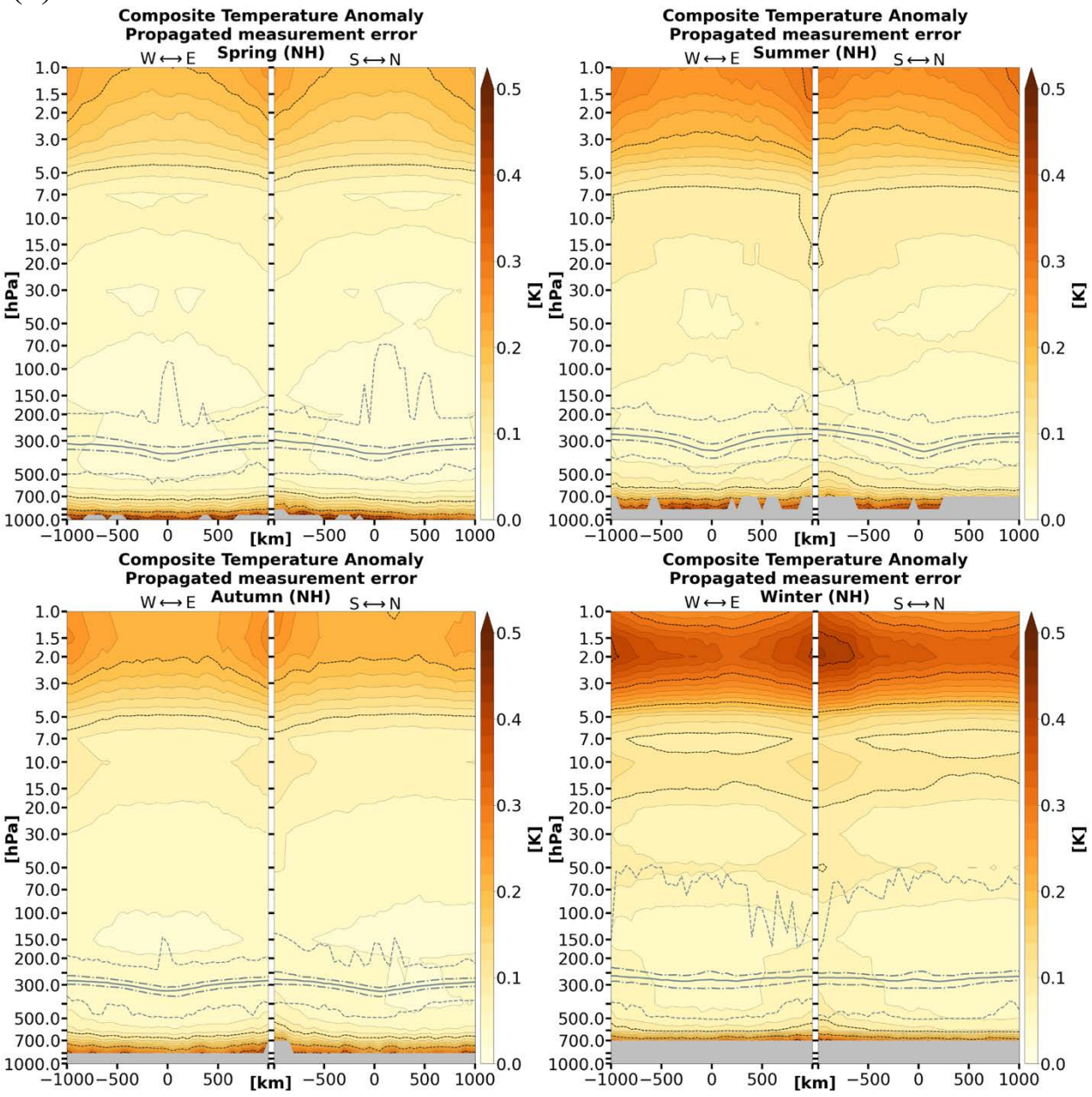

Figure 3.2.3 (continued)

(a)

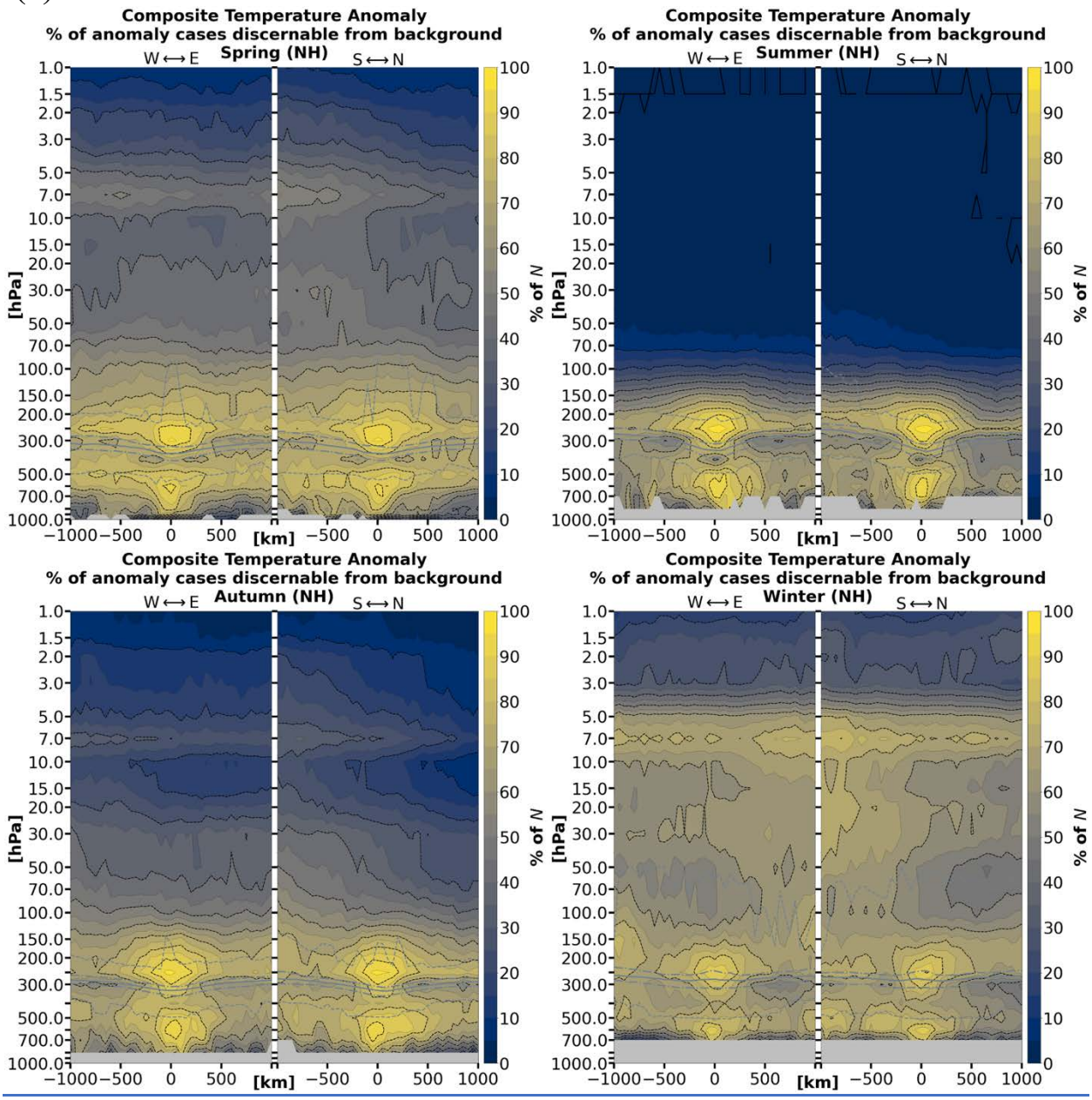

Figure 3.2.4: For each case at each valid grid point, there is a value and error for the TPV case (e.g., $T \pm \Delta T$) and a 15-day mean background value with the error taken as the RSS of the errors over the 15-day background (e.g., $T_{background} \pm \Delta T_{background}$). Shown here is the percentage of to (a) the Northern Hemisphere and (b) the Southern Hemisphere temperature anomaly samples at each grid point (i.e., fraction of **Figure 3.2.2**) where $T \pm \Delta T$ and $T_{background} \pm \Delta T_{background}$ are disjointed, that is, the instances in which the temperature error bars at a given grid point between the TPV case and the background do not overlap. Data points with less than 20 samples are excluded. The grey solid line indicates the thermal tropopause median; the long (short) dashed grey lines indicate the thermal tropopause interquartile range (minima and maxima).

(b)

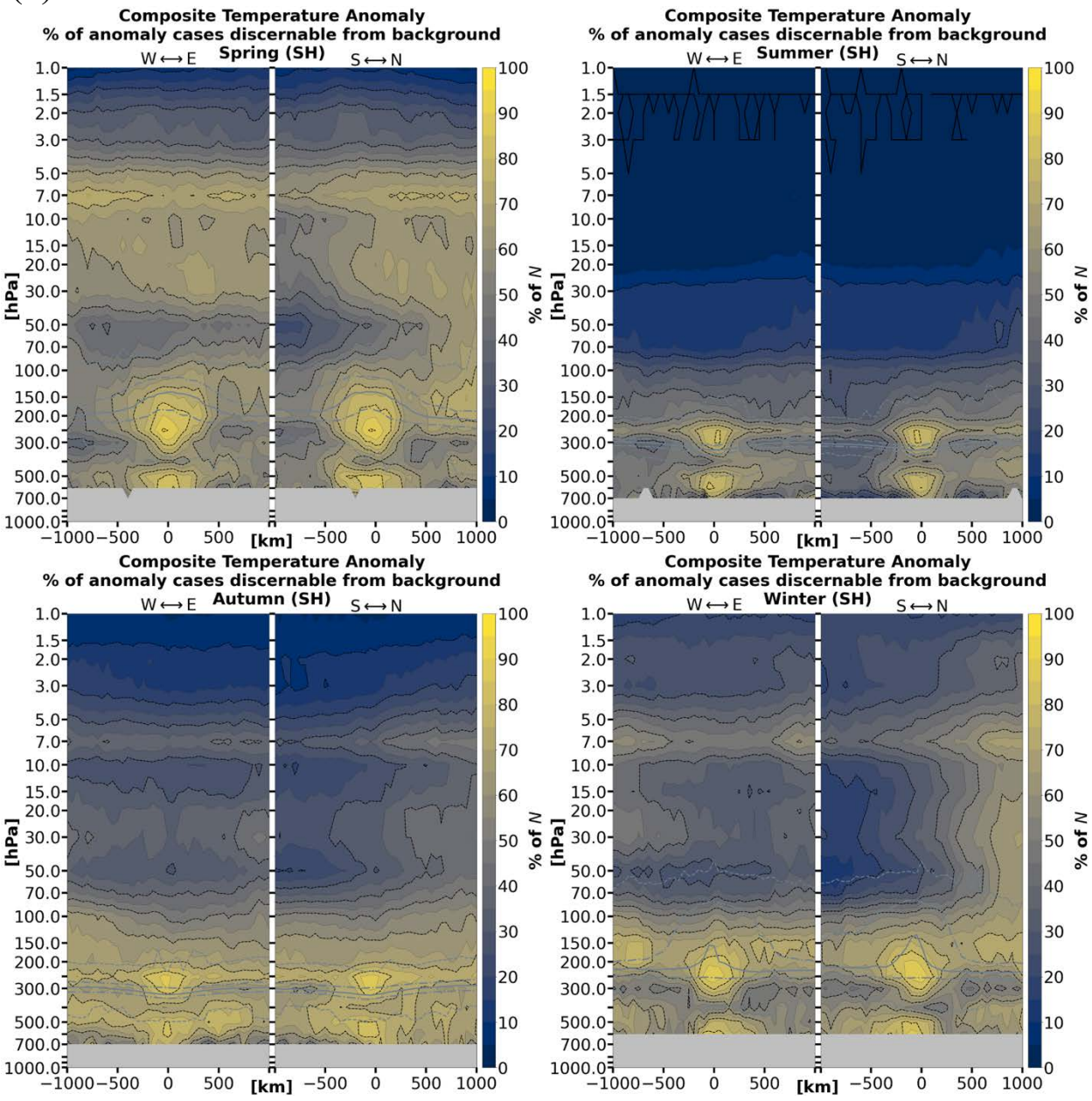

Figure 3.2.4 (continued)

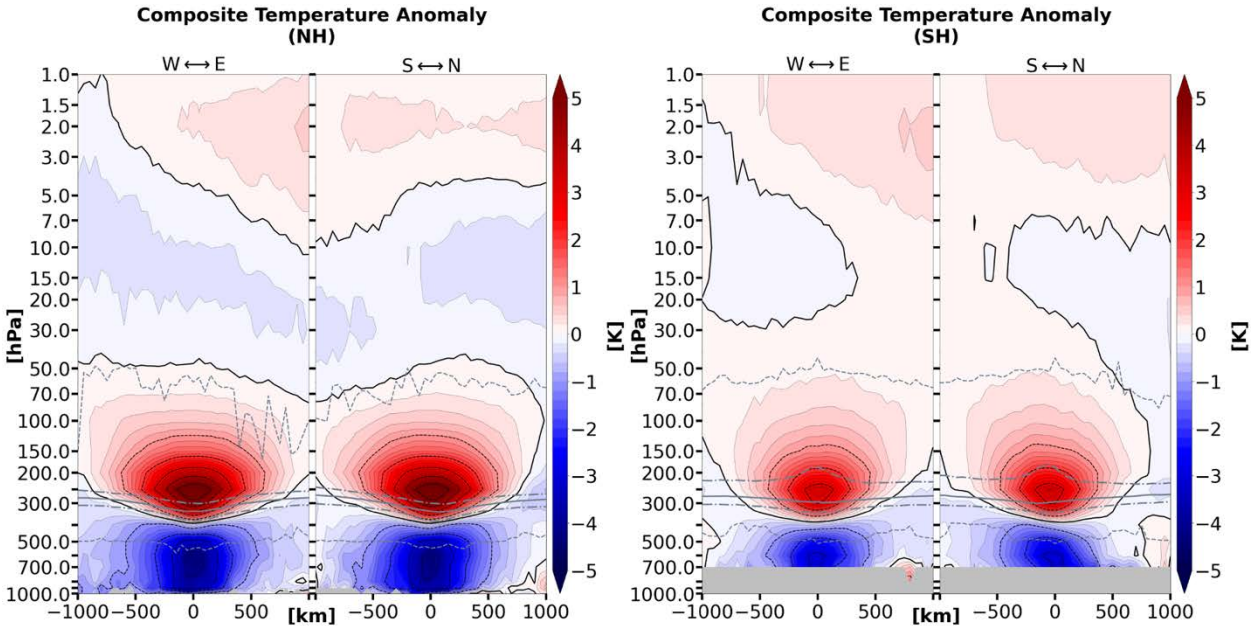

Figure 3.2.5: Composite temperature anomaly vertical cross-sections for the for TPVs under AIRS/AMSU averaged over the 1-year-long study period, separated by hemisphere. Each sample contributing to the composite temperature anomaly is weighted equally (i.e., seasons are not necessarily weighted equally; see **Figure 3.2.2**). Data points with less than 20 samples are excluded. The grey solid line indicates the thermal tropopause median; the long (short) dashed grey lines indicate the thermal tropopause interquartile range (minima and maxima).

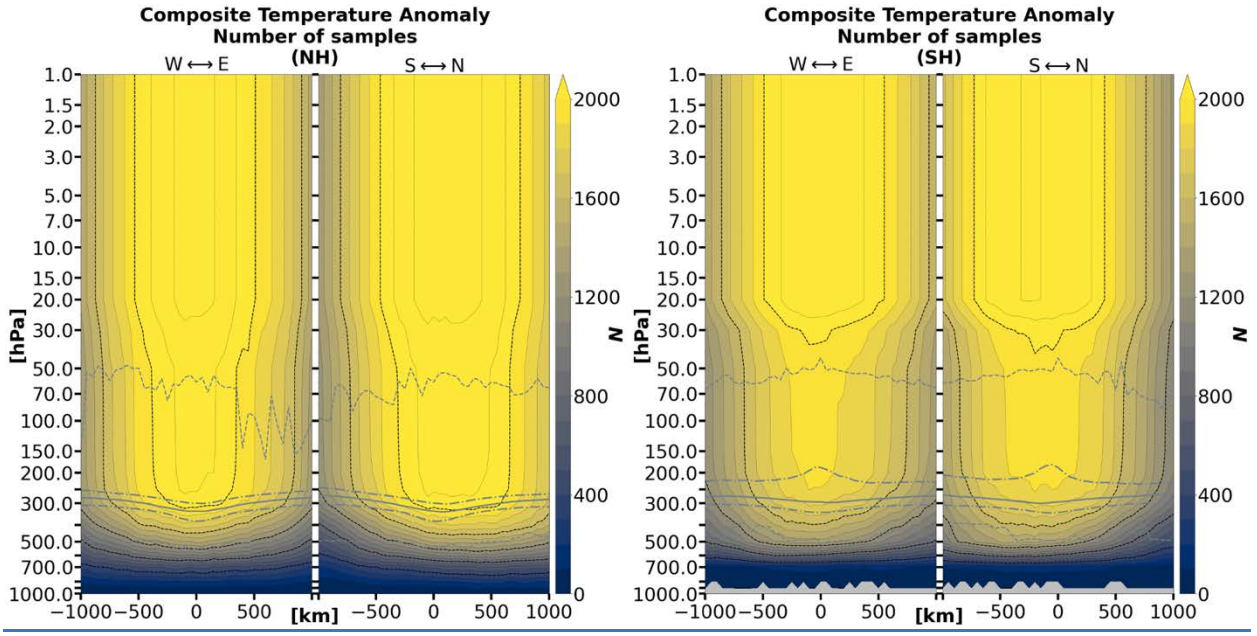

Figure 3.2.6: Sample size for each x–y–pressure-level grid point corresponding to **Figure 3.2.5** over the 1-year-long study period. Note that areas where N < 20 are masked in **Figure 3.2.5**. The grey solid line indicates the thermal tropopause median; the long (short) dashed grey lines indicate the thermal tropopause interquartile range (minima and maxima).

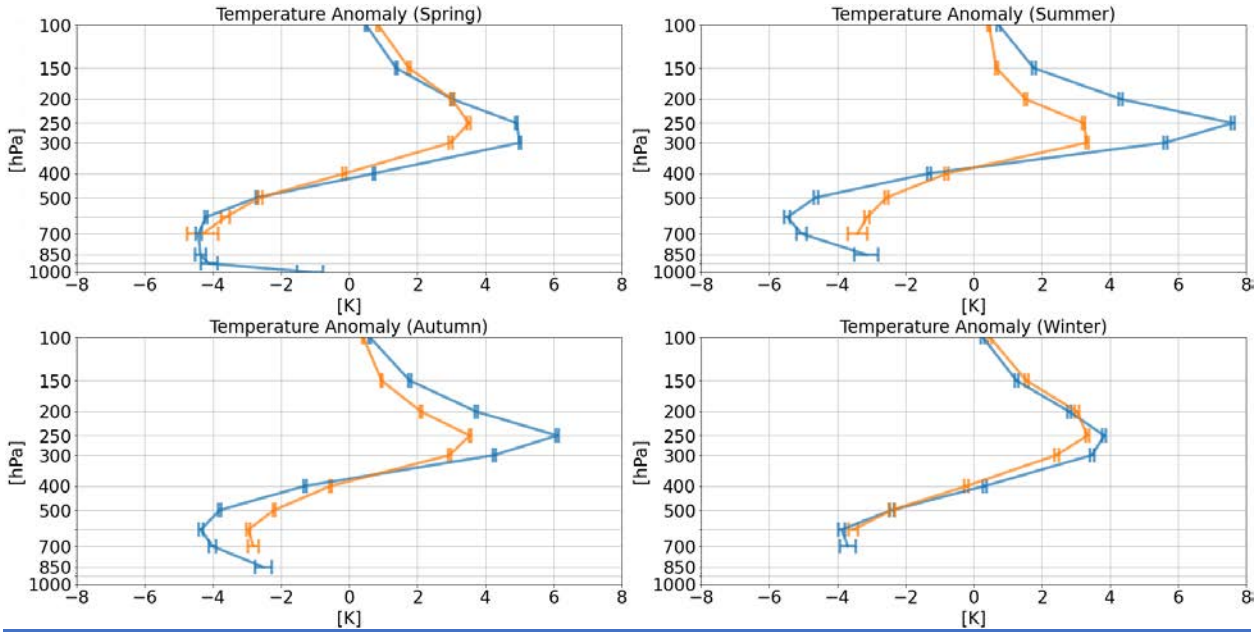

Figure 3.2.7: Composite temperature anomaly profiles of the TPV vortex center in the Northern (blue) and Southern (orange) Hemispheres separated by season. These profiles are equivalent to the vertical profiles along x = y = 0 km of **Figure 3.2.1**. Error bars correspond to the vertical of x = y = 0 km from **Figure 3.2.3**. Levels with less than 20 samples are excluded.

Section 3.3: Water vapor mass mixing ratio anomalies and relative change

TPVs exhibit a "monopole" pattern of dry mixing ratio anomalies. The minima of the negative mixing ratio anomalies occur at altitudes below 400 hPa (**Figures 3.3.1** and **3.3.10**). However, the mixing ratio anomalies of the layers starting from the 400–500 hPa layer to the surface (or at least where data is available) become non-discernible from one another in both hemispheres (**Figure 3.3.10**).

The distributions of TPV samples are highly skewed between seasons in both hemispheres. In the Northern Hemisphere, samples are heavily skewed to the spring season and very sparse during the summer (**Figure 3.3.2(a)**). In the Southern Hemisphere, samples are heavily skewed to the autumn season, and are almost completely absent in the winter season (**Figure 3.3.2(b)**). In both hemispheres, the mixing ratio anomaly errors increase with decreasing sample sizes (**Figure 3.3.3**) and increase when approaching the surface.

The discernibility of the corresponding mixing ratios between TPV cases and the background are generally greatest from 250–400 hPa (**Figure 3.3.4**) and are not collocated with the negative mixing ratio anomaly minima in **Figures 3.3.1**. However, they are approximately collocated with the regions where the mixing ratio relative change are most negative (**Figure 3.3.5**), as well as where the relative change errors are lowest (**Figure 3.3.6**).

(a)

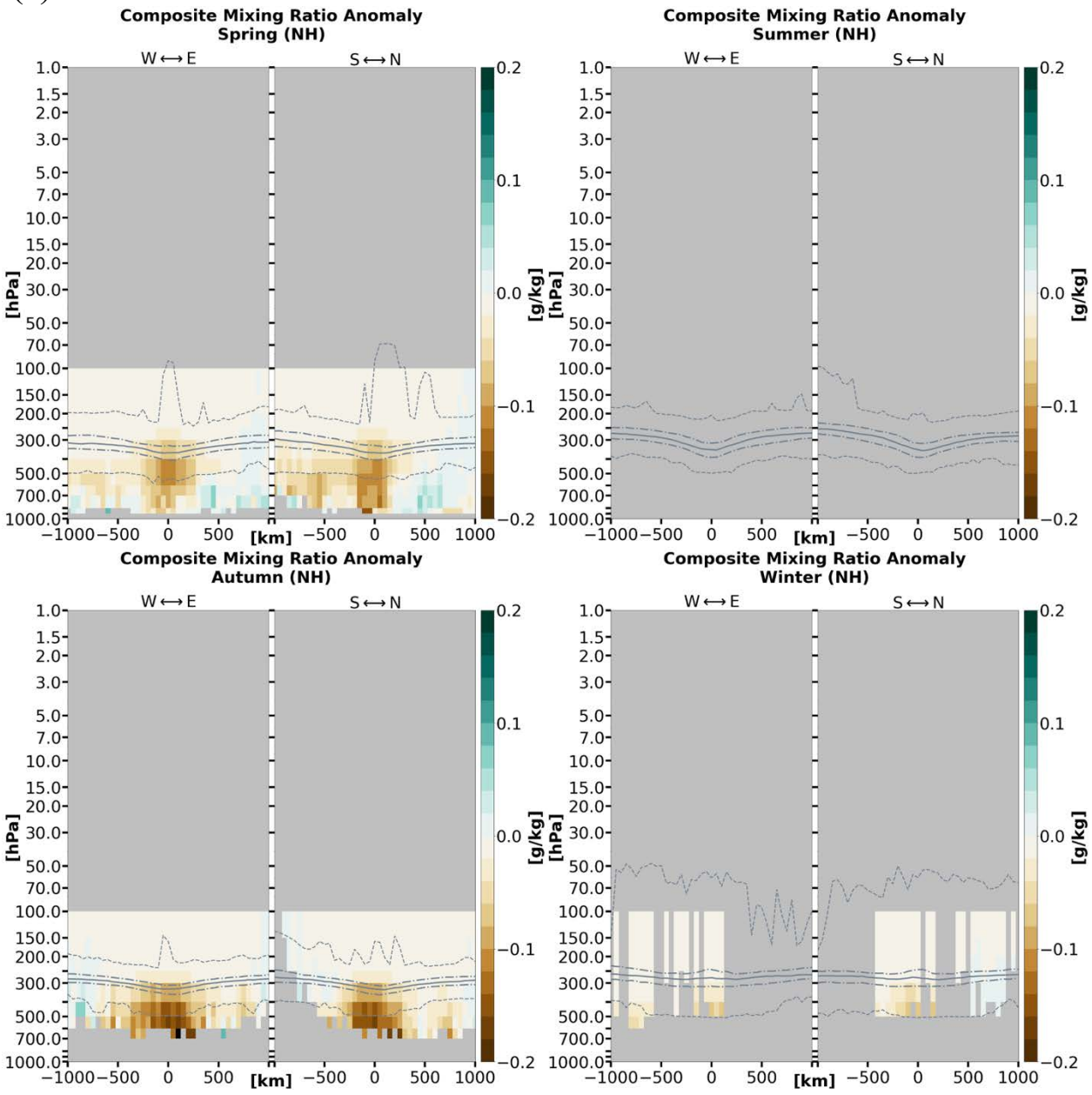

Figure 3.3.1: Composite water vapor mass mixing ratio anomaly cross-sections by season for TPVs in (a) the Northern Hemisphere and (b) the Southern Hemisphere under AIRS/AMSU. West-to-east and south-to-north directions are the same as described for the temperature anomalies in **Figure 3.2.1**. Anomalies are with respect to a 15-day mean background. Data cells with less than 20 samples are excluded. The grey solid line indicates the thermal tropopause median; the long (short) dashed grey lines indicate the thermal tropopause interquartile range (minima and maxima).

(b)

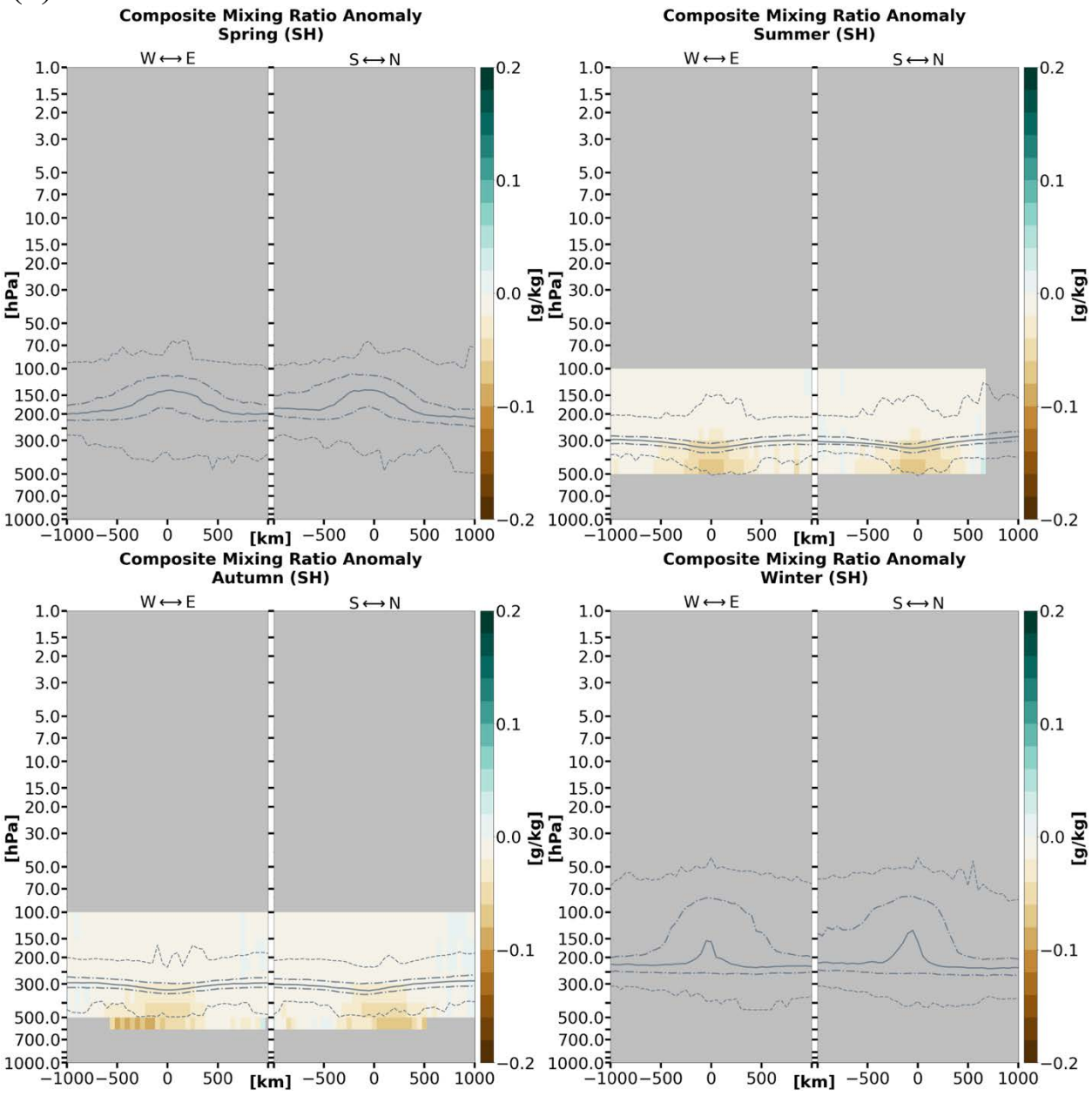

Figure 3.3.1 (continued)

(a)

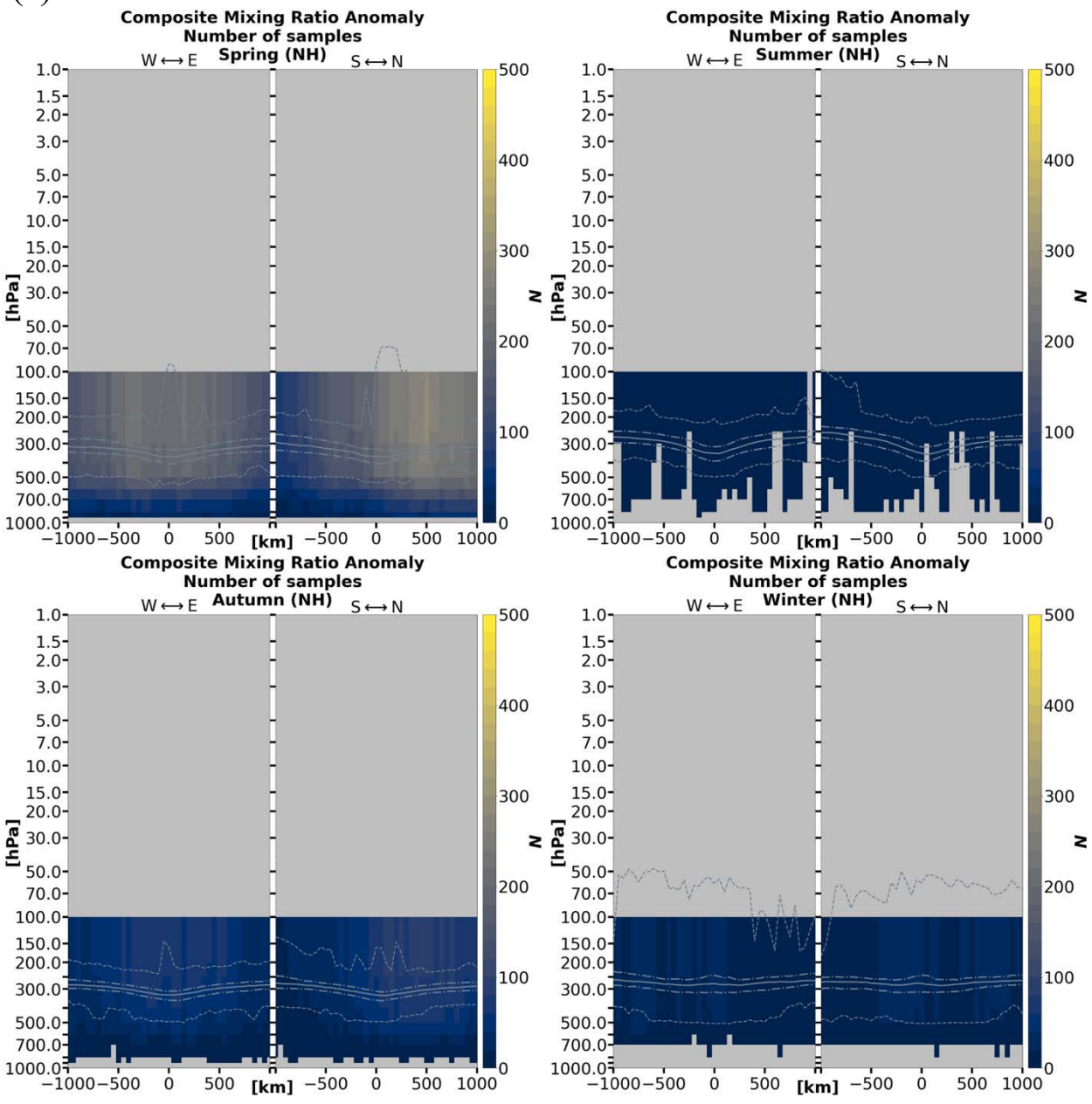

Figure 3.3.2: Sample size for each x–y–pressure-layer grid cell corresponding to (a) the Northern Hemisphere and (b) the Southern Hemisphere TPV mixing ratio anomalies in **Figure 3.3.1**. Sample sizes are identical for mixing ratio relative change. Note that areas where N < 20 are masked in **Figures 3.3.1, 3.3.3, 3.2.4, 3.3.5, and 3.3.6**. The grey solid line indicates the thermal tropopause median; the long (short) dashed grey lines indicate the thermal tropopause interquartile range (minima and maxima).

(b)

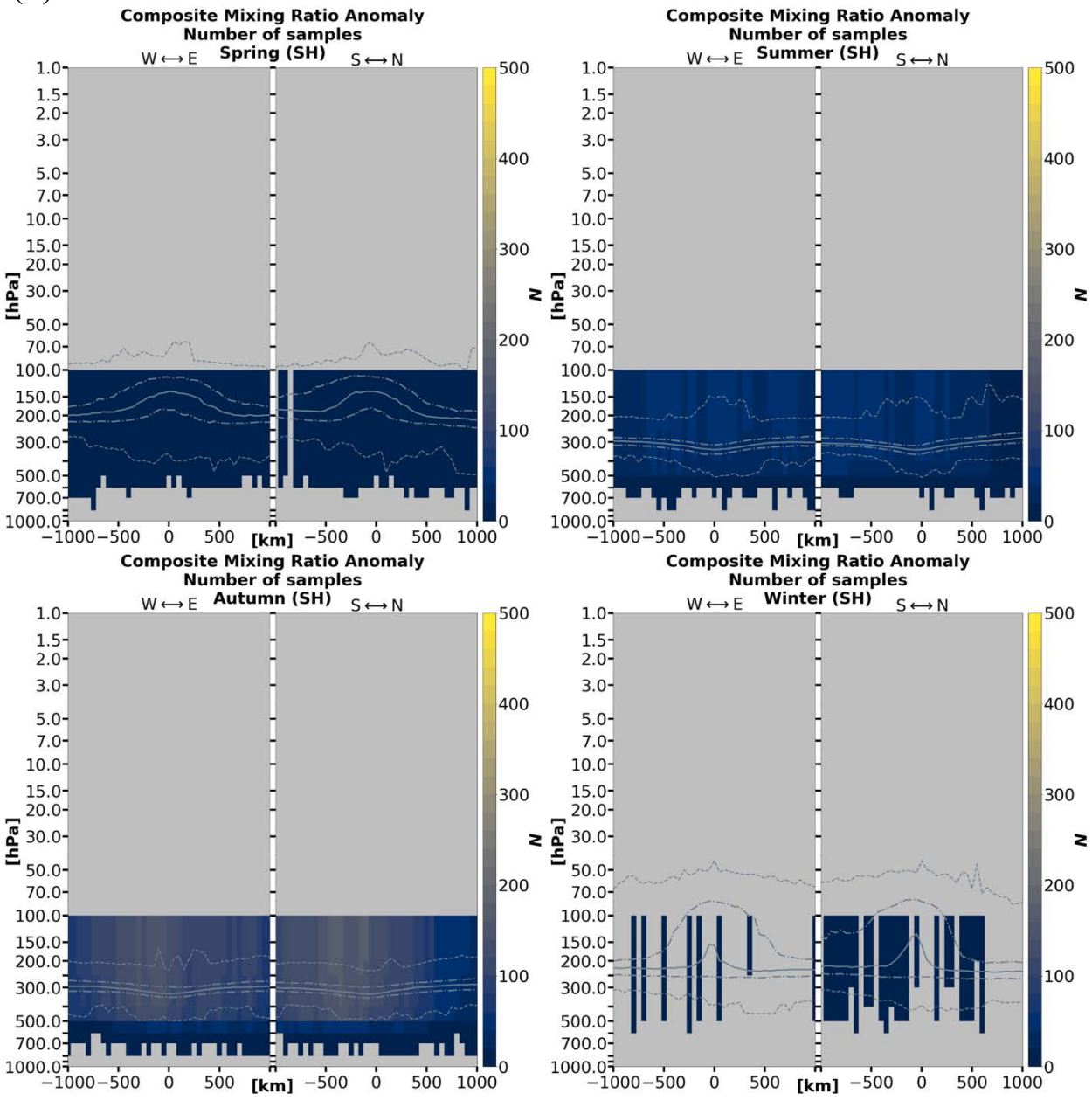

Figure 3.3.2 (continued)

(a)

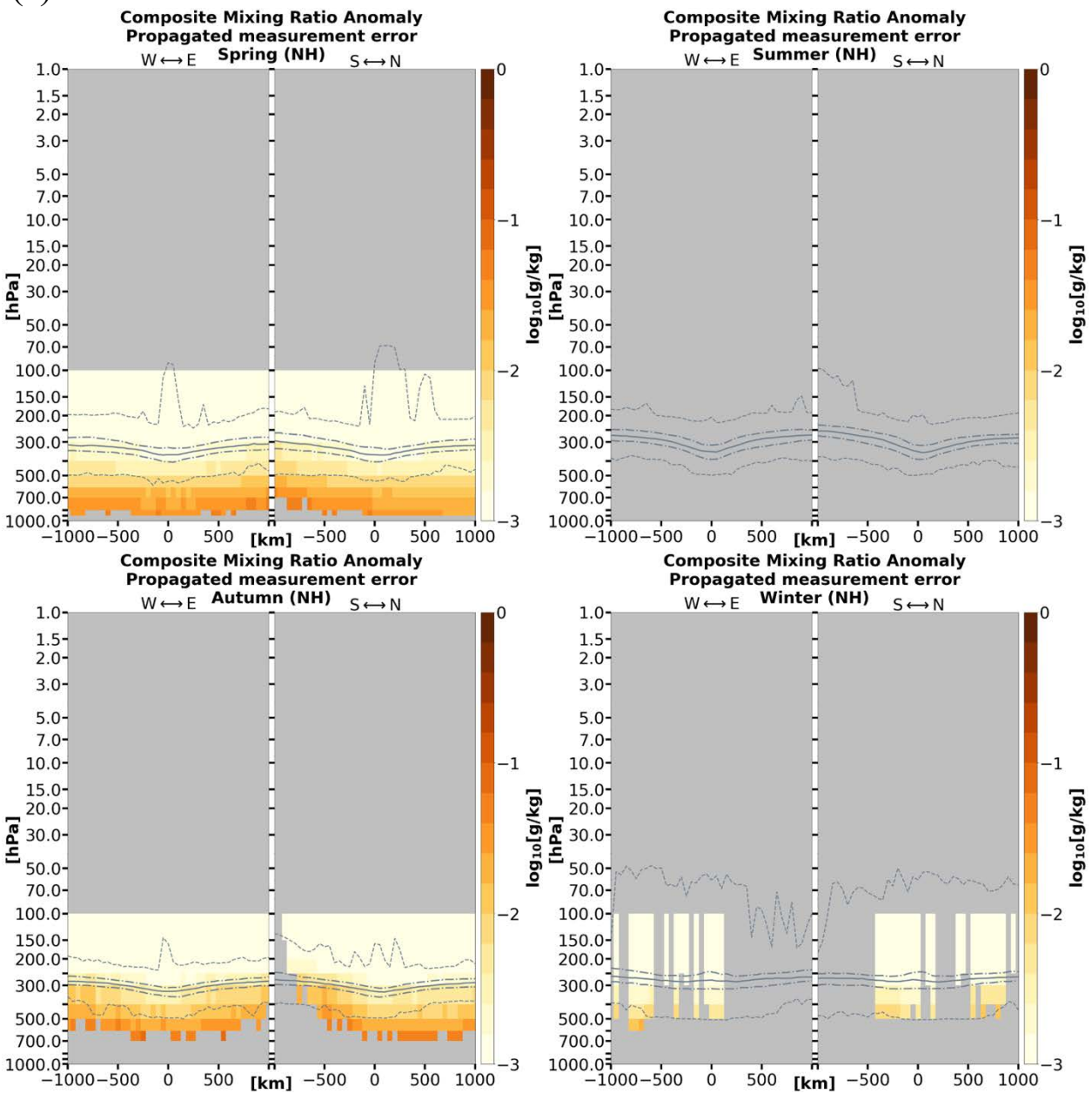

Figure 3.3.3: Cross-sections of (a) the Northern Hemisphere and (b) the Southern Hemisphere TPV water vapor mass mixing ratio anomaly errors for each x–y–pressure-layer grid cell corresponding to the anomaly values in **Figure 3.3.1.** Data cells with less than 20 samples are excluded. The grey solid line indicates the thermal tropopause median; the long (short) dashed grey lines indicate the thermal tropopause interquartile range (minima and maxima).

(b)

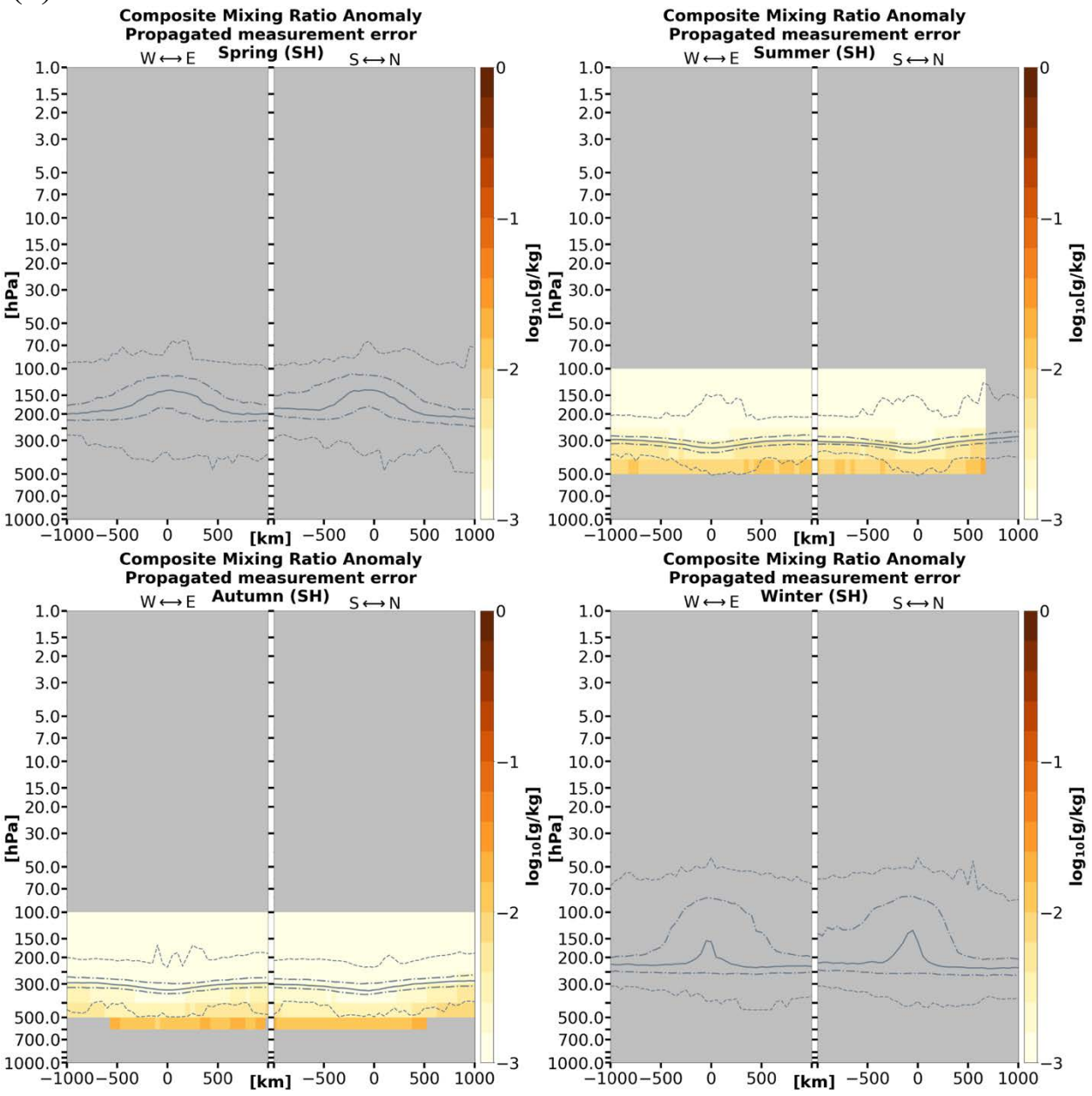

Figure 3.3.3 (continued)

(a)

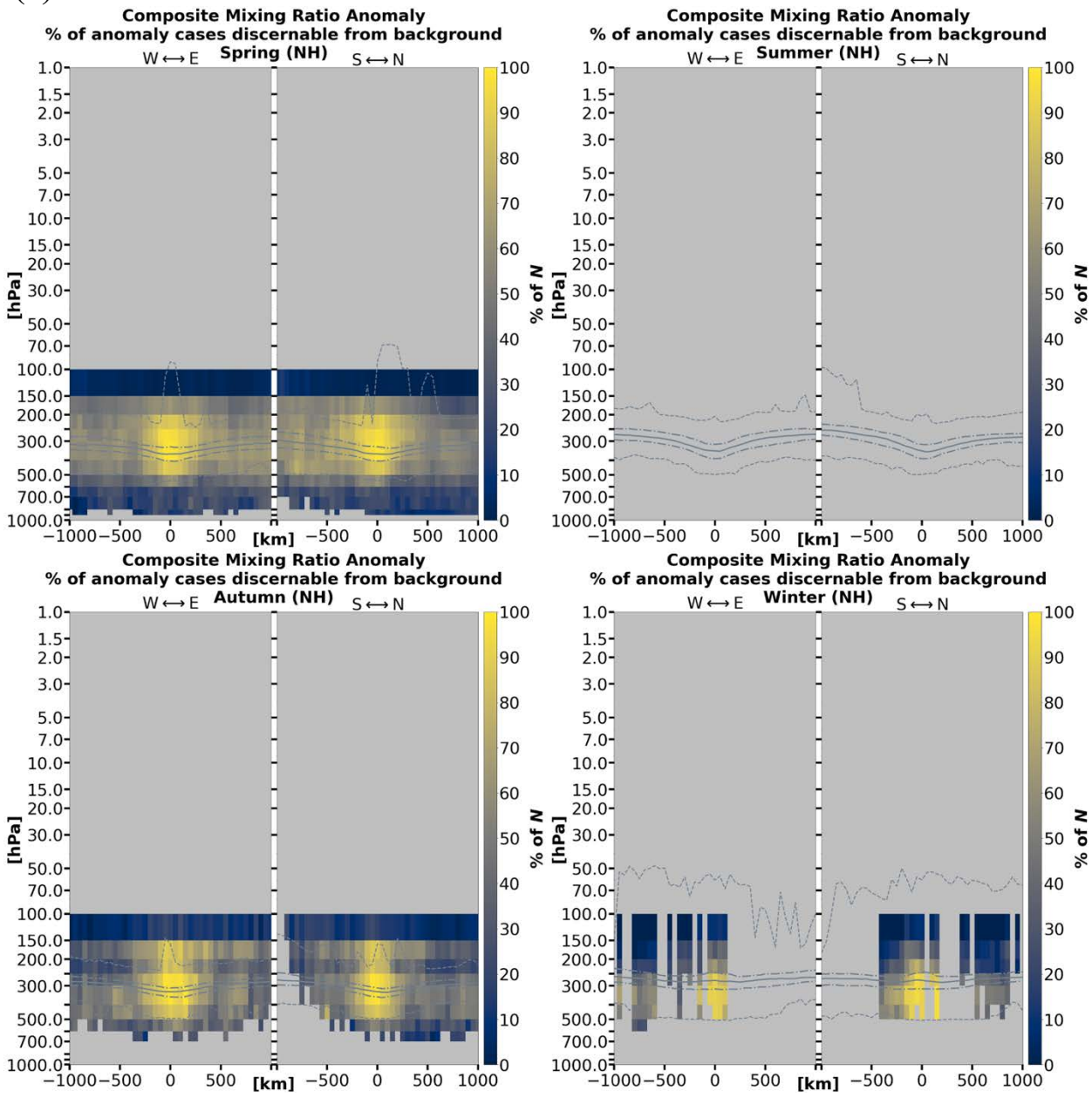

Figure 3.3.4: Percentage (i.e., fraction of **Figure 3.3.2**) of (a) Northern Hemisphere and (b) Southern Hemisphere TPV mixing ratio anomaly samples at each grid point where the mixing ratios between TPV cases and their corresponding 15-day backgrounds are discernible (i.e., non-overlapping error bars). Data cells with less than 20 samples are excluded. The grey solid line indicates the thermal tropopause median; the long (short) dashed grey lines indicate the thermal tropopause interquartile range (minima and maxima).

(b)

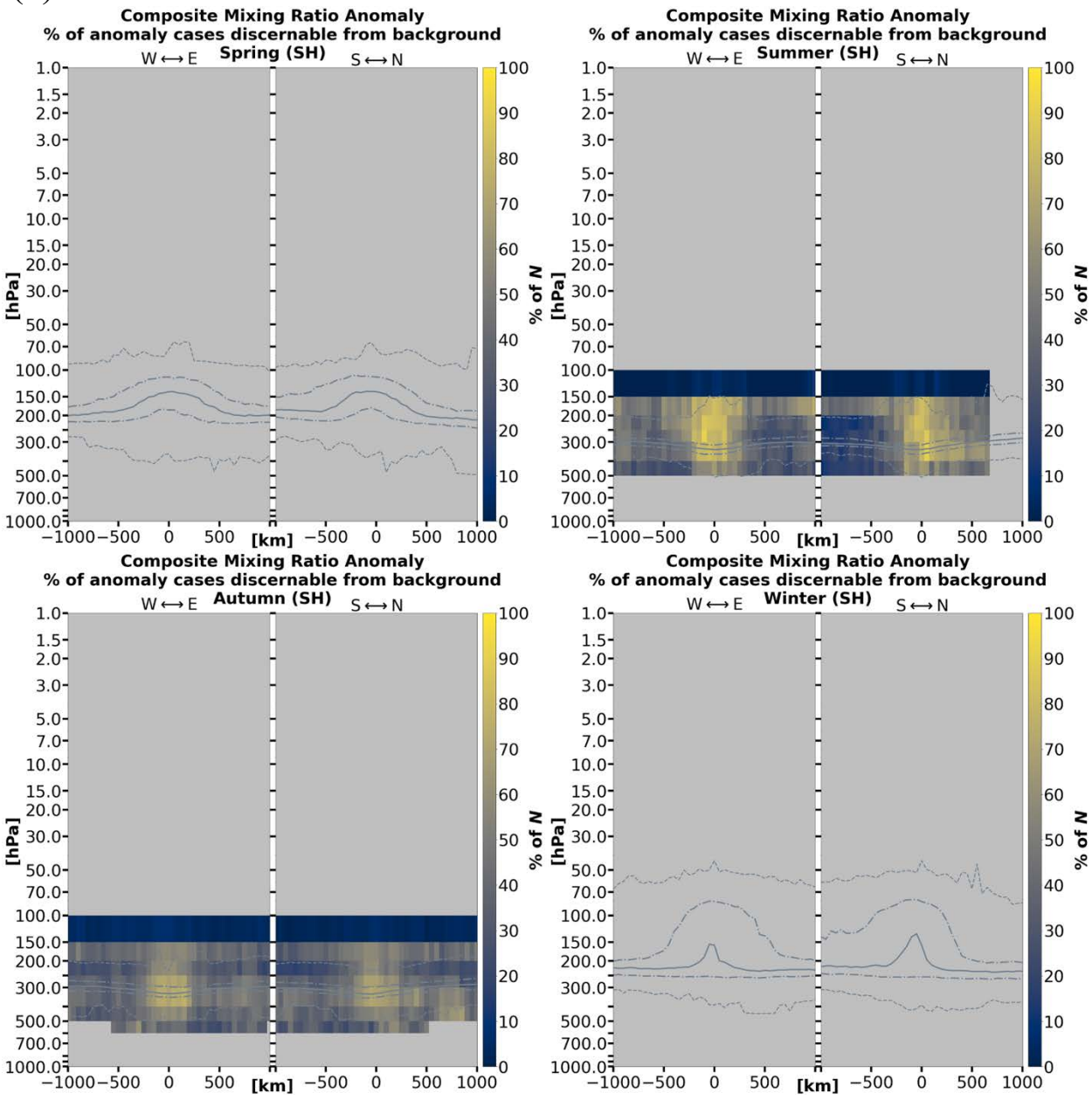

Figure 3.3.4 (continued)

(a)

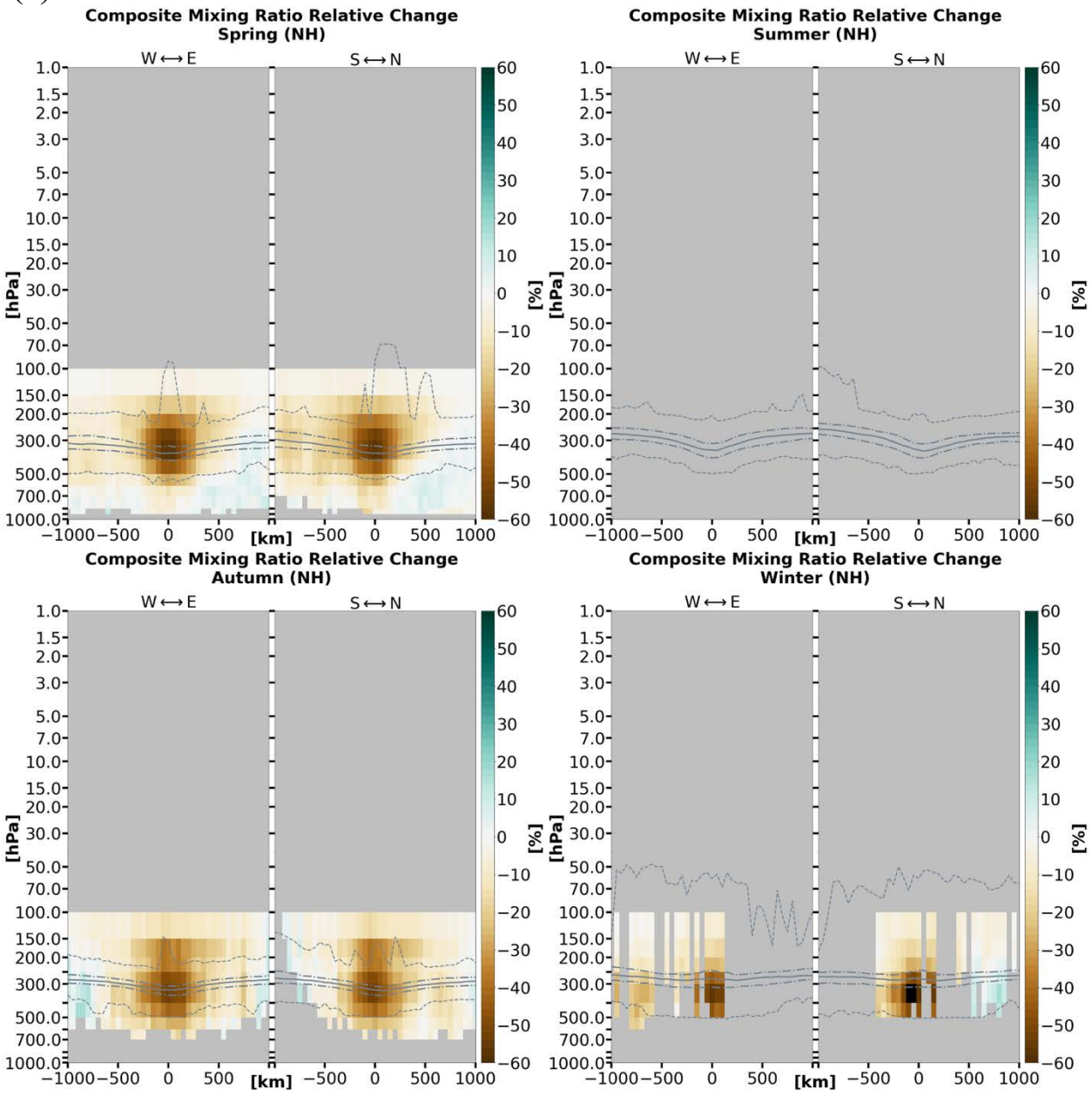

Figure 3.3.5: Composite water vapor mass mixing ratio relative change cross-sections by season for TPVs in (a) the Northern Hemisphere and (b) the Southern Hemisphere under AIRS/AMSU. Changes are expressed as a percentage relative to the 15-day background. Data cells with less than 20 samples are excluded. The grey solid line indicates the thermal tropopause median; the long (short) dashed grey lines indicate the thermal tropopause interquartile range (minima and maxima).

(b)

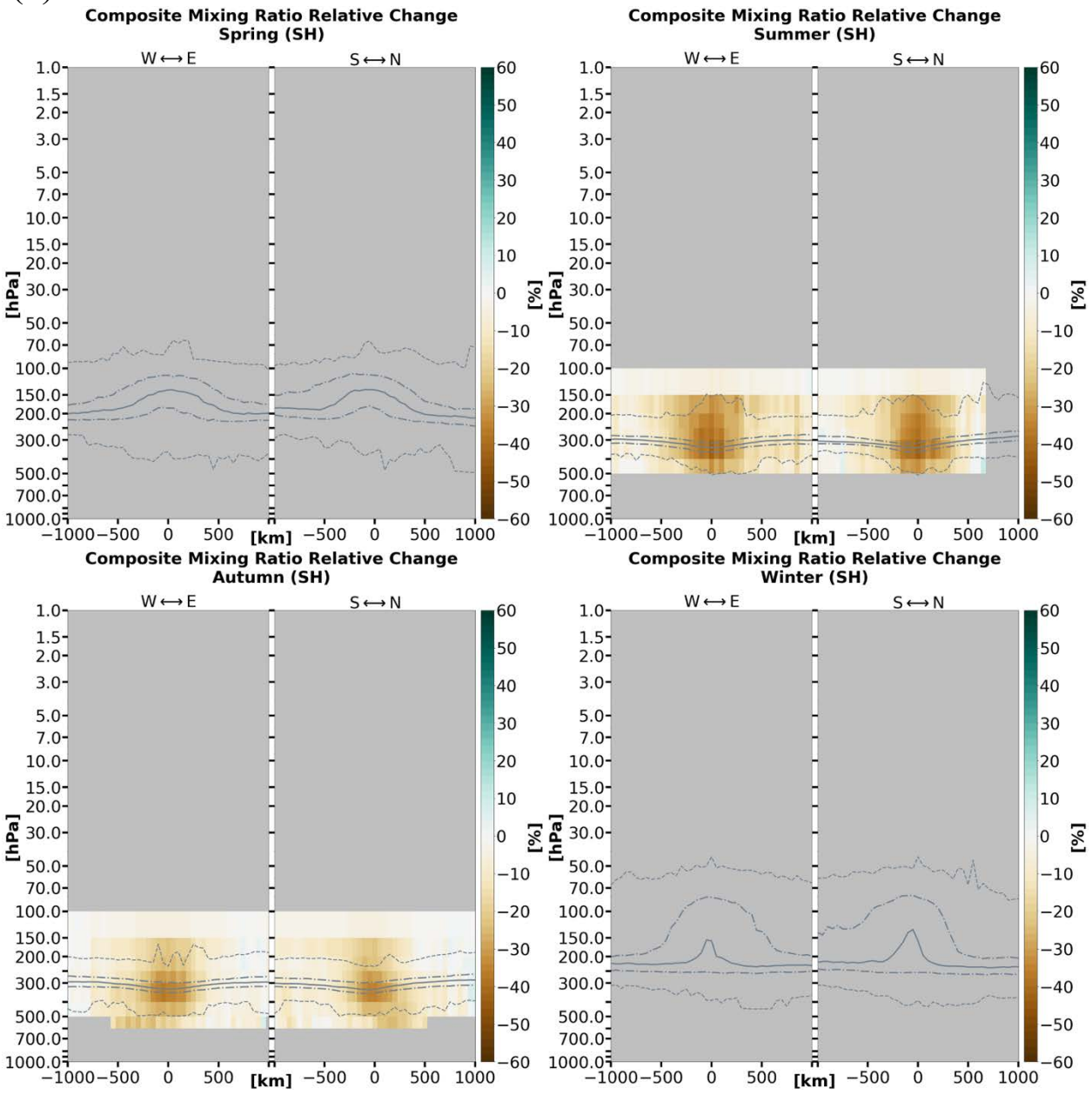

Figure 3.3.5 (continued)

(a)

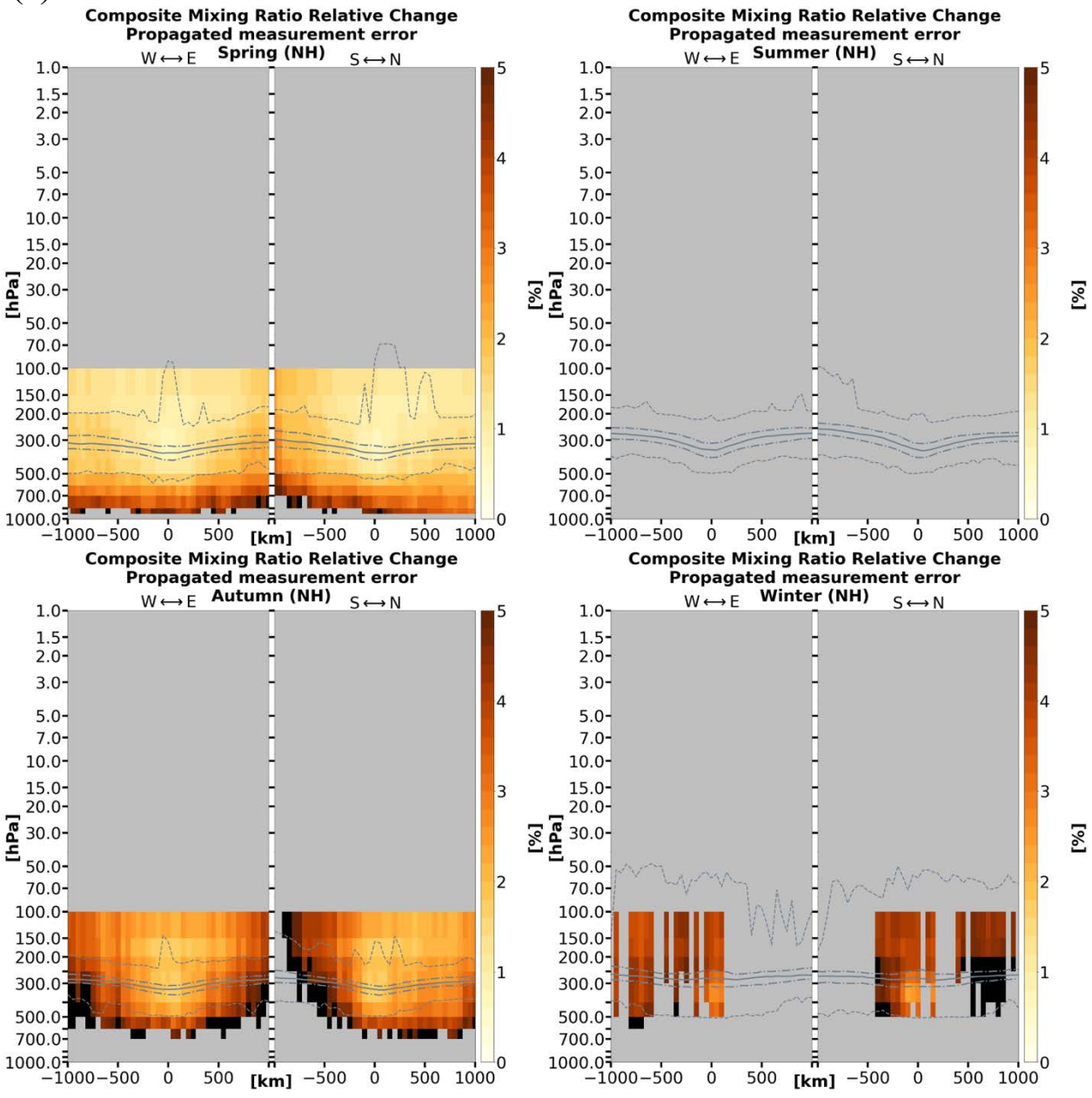

Figure 3.3.6: Cross-sections of (a) the Northern Hemisphere and (b) the Southern Hemisphere TPV mixing ratio relative change errors for each x–y–pressure-layer grid cell corresponding to the relative change values in **Figure 3.3.5.** Data cells with less than 20 samples are excluded. The grey solid line indicates the thermal tropopause median; the long (short) dashed grey lines indicate the thermal tropopause interquartile range (minima and maxima).

(b)

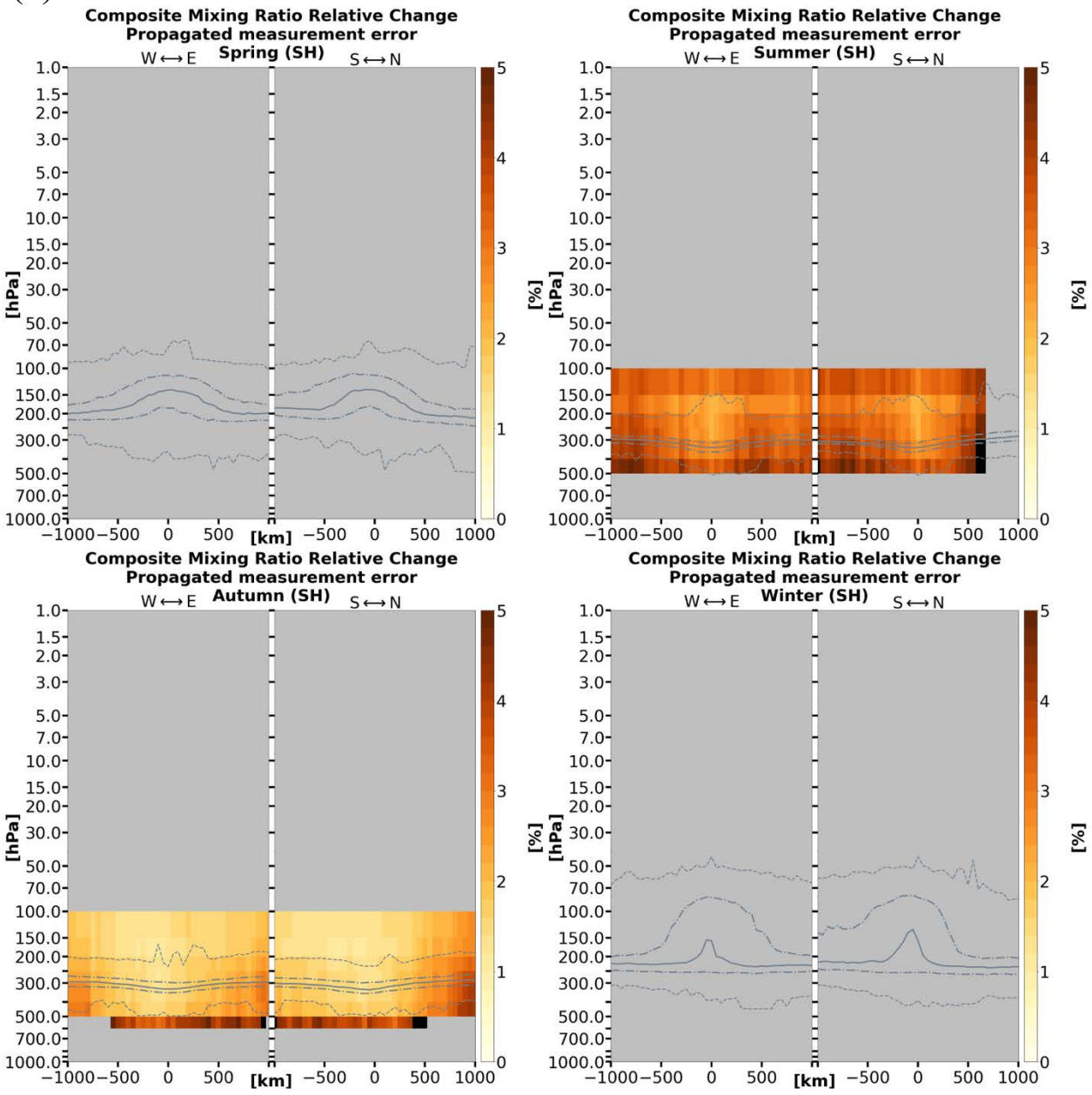

Figure 3.3.6 (continued)

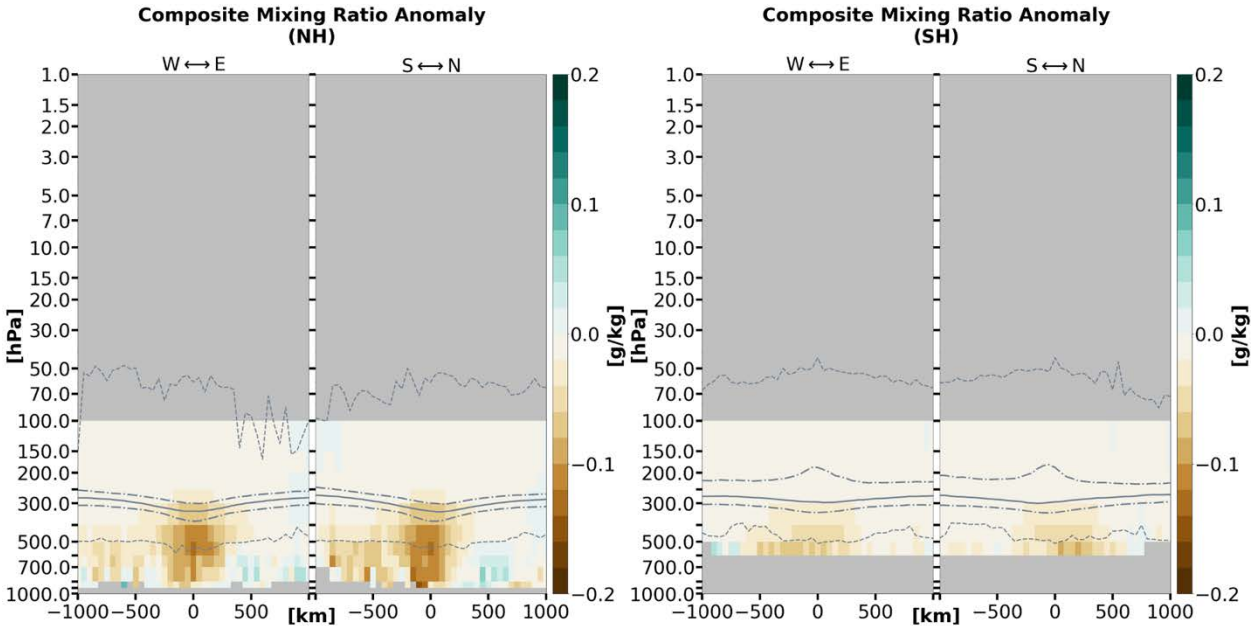

Figure 3.3.7: Composite water vapor mass mixing ratio anomaly cross-sections for TPVs under AIRS/AMSU averaged over the 1-year-long study period, separated by hemisphere. Each contributing sample is weighted equally (i.e., seasons are not weighted equally due to different sample sizes between seasons). Data cells with less than 20 samples are excluded. The grey solid line indicates the thermal tropopause median; the long (short) dashed grey lines indicate the thermal tropopause interquartile range (minima and maxima).

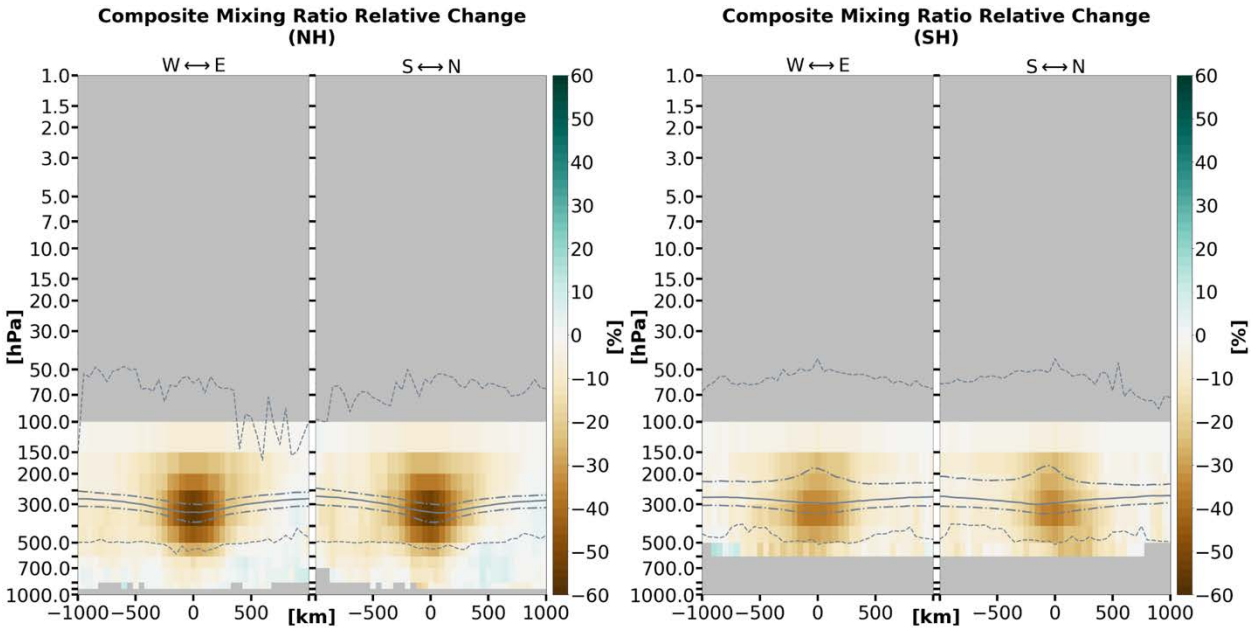

Figure 3.3.8: As in **Figure 3.3.7**, but for relative percent change.

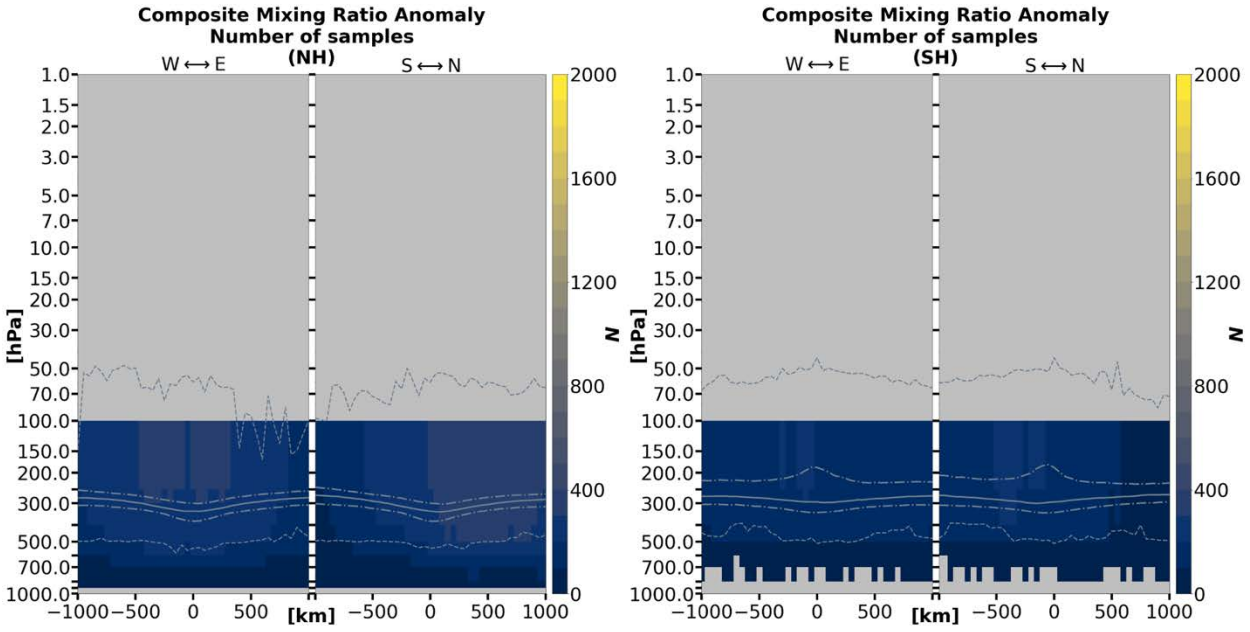

Figure 3.3.9: Sample size for each x–y–pressure-layer grid cell corresponding to **Figures 3.3.7 and 3.3.8** over the 1-year-long study period. Note that areas where N < 20 are masked in **Figures 3.3.7 and 3.3.8**. The grey solid line indicates the thermal tropopause median; the long (short) dashed grey lines indicate the thermal tropopause interquartile range (minima and maxima).

Mixing ratio relative change from the 15-day background (**Figure 3.3.5**) and associated errors (**Figure 3.3.6**) are also considered. The sample sizes for mixing ratio relative change are identical to the sample sizes for mixing ratio anomalies. The most negative percent change for mixing ratio is found in the 300–400 hPa layer for TPVs in the Northern Hemisphere (**Figure 3.3.11**) in the autumn, winter, and spring seasons (the summer season is unavailable), and in the Southern Hemisphere in the autumn season (the winter and spring seasons are unavailable). Neighboring layers between 150 hPa and 400 hPa for the Southern Hemisphere summer season are not distinguishable. However, the error bars of 300–400 hPa layer do not overlap with those of the 200–250 hPa layer, placing the most negative percent change somewhere between 250 hPa and 400 hPa.

Mixing ratio anomaly and relative change comparisons between the Northern and Southern Hemispheres are available for only the autumn season (**Figures 3.3.10 and 3.3.11**). Both the anomaly and relative change for mixing ratio are discernibly more negative for Northern Hemisphere TPVs than for Southern Hemisphere TPVs.

The total year-long composites for mixing ratio anomalies and relative change are illustrated respectively in **Figures 3.3.7 and 3.3.8**, with corresponding sample size in **Figure 3.3.9**. However, they are heavily weighted toward the spring (autumn) in the Northern (Southern) Hemisphere, with the summer (winter) seasons having almost no contribution to the year-long composites. Since **Figures 3.3.7 and 3.3.8** do not indicate an equivalent comparison between Northern and Southern Hemisphere TPVs, no conclusions are made here for the total composites.

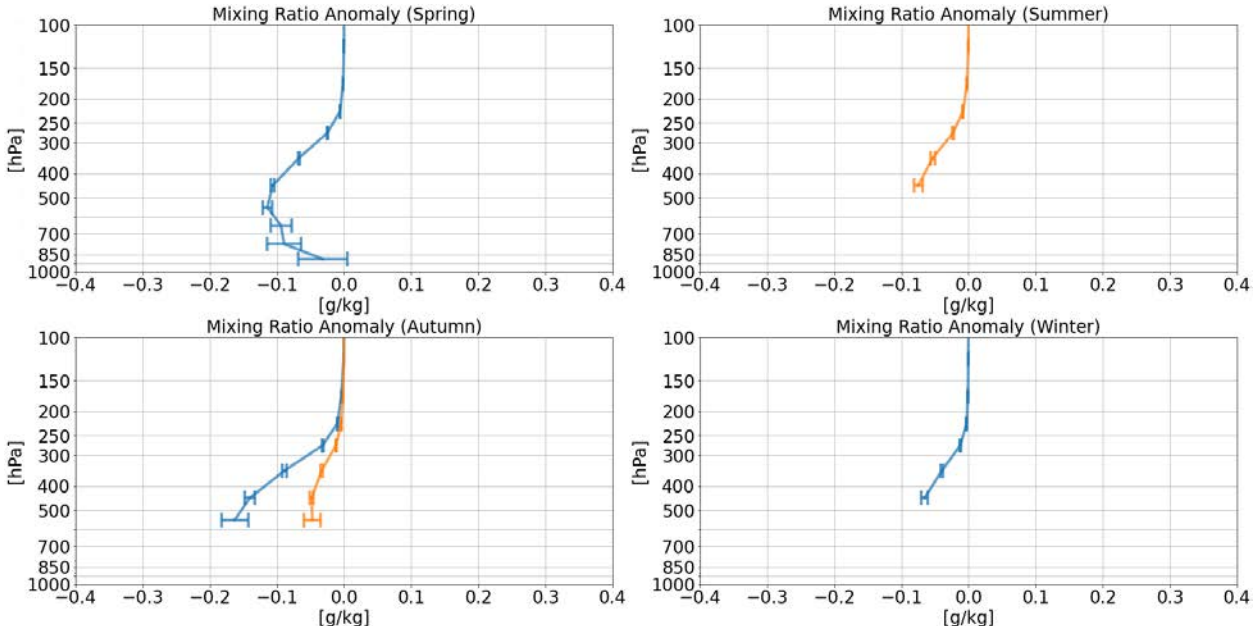

Figure 3.3.10: Composite water vapor mass mixing ratio anomaly profiles of the TPV vortex center in the Northern (blue) and Southern (orange) Hemispheres separated by season. These profiles are equivalent to the vertical profiles along x = y = 0 km of **Figure 3.3.1**. Error bars correspond to the vertical of x = y = 0 km from **Figures 3.3.3**. Layers with less than 20 samples are excluded. This results in the absence of some layers in the profiles, or even the absence of an entire profile in some cases.

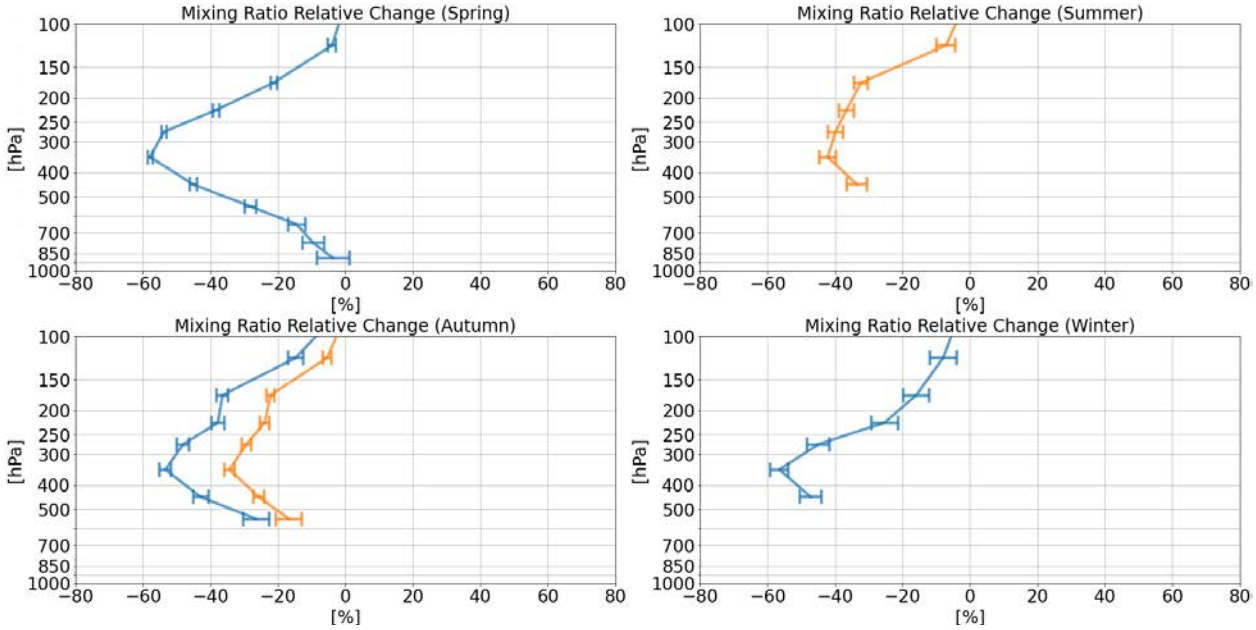

Figure 3.3.11: As in **Figure 3.3.10**, but for relative percent change.

Section 3.4: Relative humidity anomalies

Temperature and relative humidity variables are reported only as level quantities in the AIRS/AMSU V7 L2 Standard Product. The relative humidity values in the AIRS/AMSU product use the calculation for saturation water vapor pressure in Equation 10 from Murphy and Koop (2005) (Thrastarson et al. 2020). No error values for relative humidity are given in the product. Calculating errors were not attempted in this study because the sources of error in empirical equations are complex and difficult to quantify (Murphy and Koop 2005).

Relative humidity anomalies for the Northern and Southern Hemispheres are given in **Figure 3.4.1**. Sample sizes of relative humidity anomalies across seasons (**Figure 3.4.2**) mirror the same seasonal distributions as those for mixing ratios in the previous section (**Figure 3.3.2**).

The relative humidity anomaly "dipole" pattern is usually present in both hemispheres, although the signal from the stratospheric negative relative humidity anomaly dominates the pattern. The tropospheric positive relative humidity anomalies (where available) generally become obscured due to sampling noise and/or the absence of data in both hemispheres except for the Northern Hemisphere spring (**Figure 3.4.1(a)**), which has the largest sample sizes close to the surface (**Figure 3.4.2(a)**). TPVs in the Northern Hemisphere spring season are characterized with increasingly positive relative humidity anomalies when approaching the surface, exceeding +20% at and below the 850 hPa level.

Negative relative humidity anomalies generally range between ~ –30% to just above –40% (~ –25% to just under –35%) for TPVs in the Northern (Southern) Hemisphere. They are generally positioned at the 250 hPa or 300 hPa levels. TPVs in the Northern Hemisphere under AIRS/AMSU have a larger magnitude of negative anomalies than those in Cavallo and Hakim (2010) and Borg, Cavallo, and Turner (2020) when comparing with the year-long composite (**Figure 3.4.3**). The summer and winter TPVs in the Northern Hemisphere also have a larger magnitude of negative relative humidity anomalies than those in Cavallo and Hakim (2010). Note that the year-long composites for relative humidity have the same caveats regarding seasonal sample distribution as those for mixing ratio anomaly and relative change in the previous section (**Figures 3.3.7 and 3.3.8**). Corresponding sample size for the year-long composite (**Figure 3.4.3**) is shown in **Figure 3.4.4**, which mirrors the sample sizes for mixing ratio in **Figure 3.3.9**.

(a)

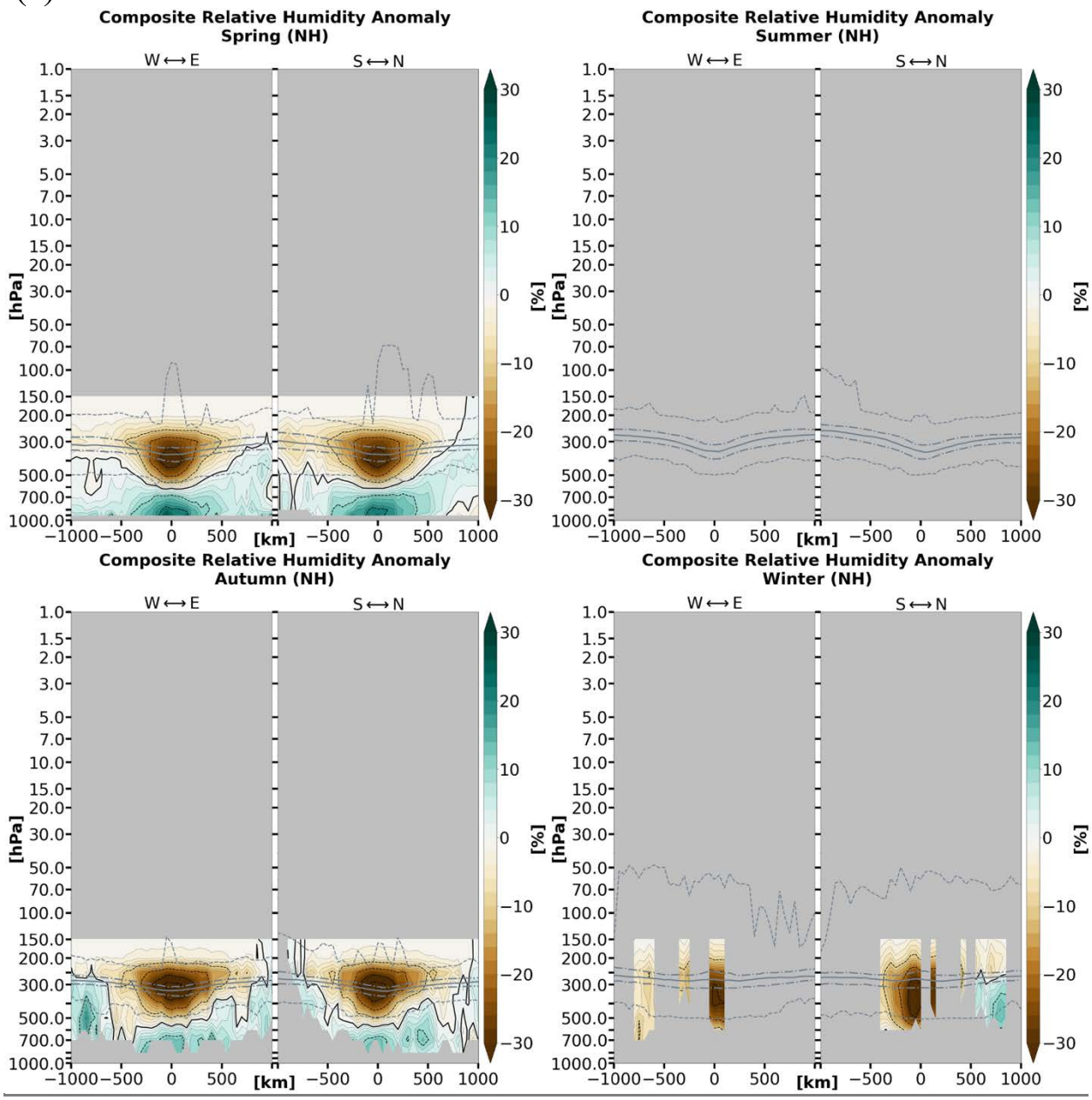

Figure 3.4.1: Composite relative humidity anomaly cross-sections by season for TPVs in (a) the Northern Hemisphere and (b) the Southern Hemisphere under AIRS/AMSU. Anomalies are with respect to a 15-day mean background. The grey solid line indicates the thermal tropopause median; the long (short) dashed grey lines indicate the thermal tropopause interquartile range (minima and maxima).

(b)

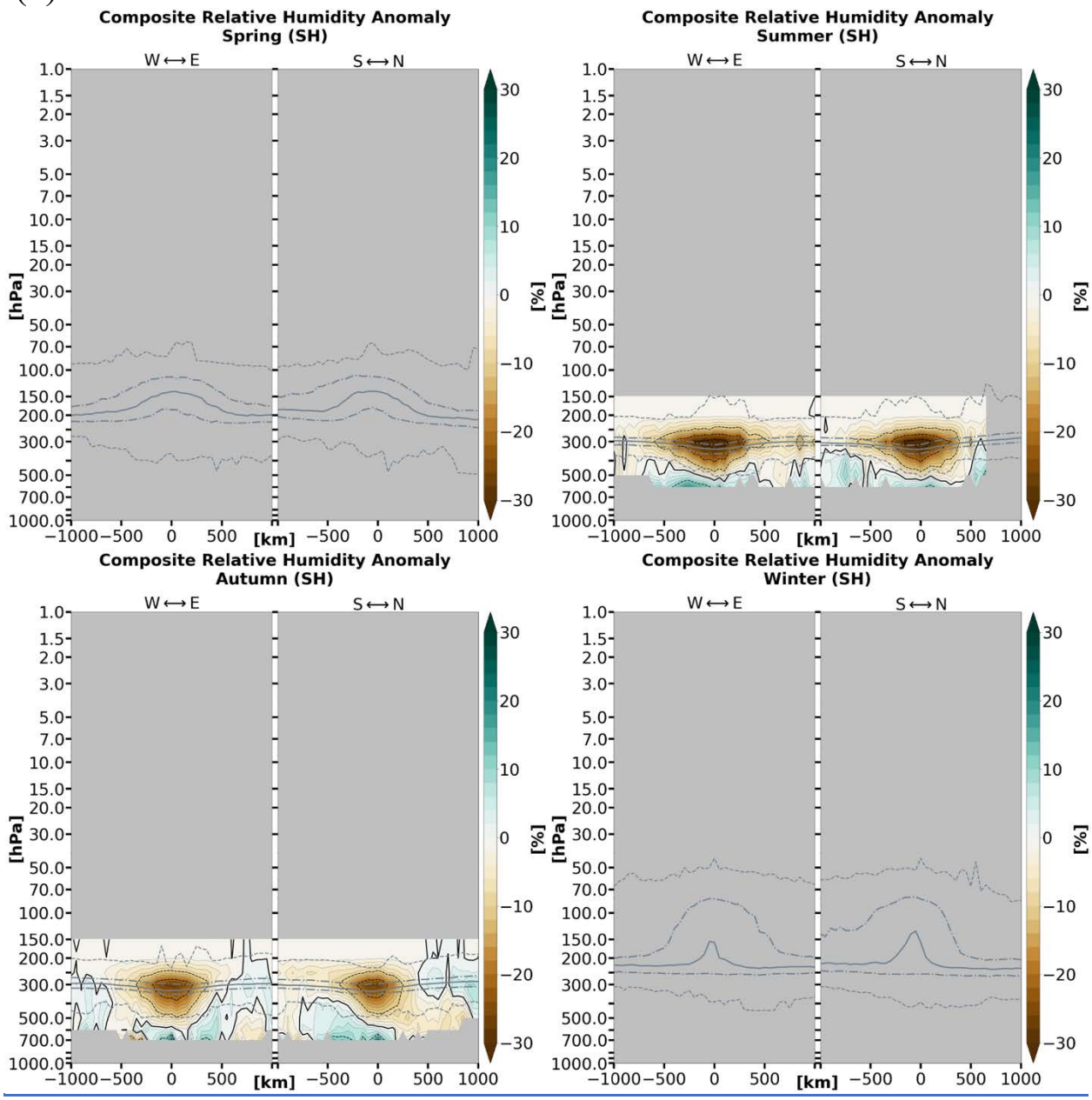

Figure 3.4.1 (continued)

(a)

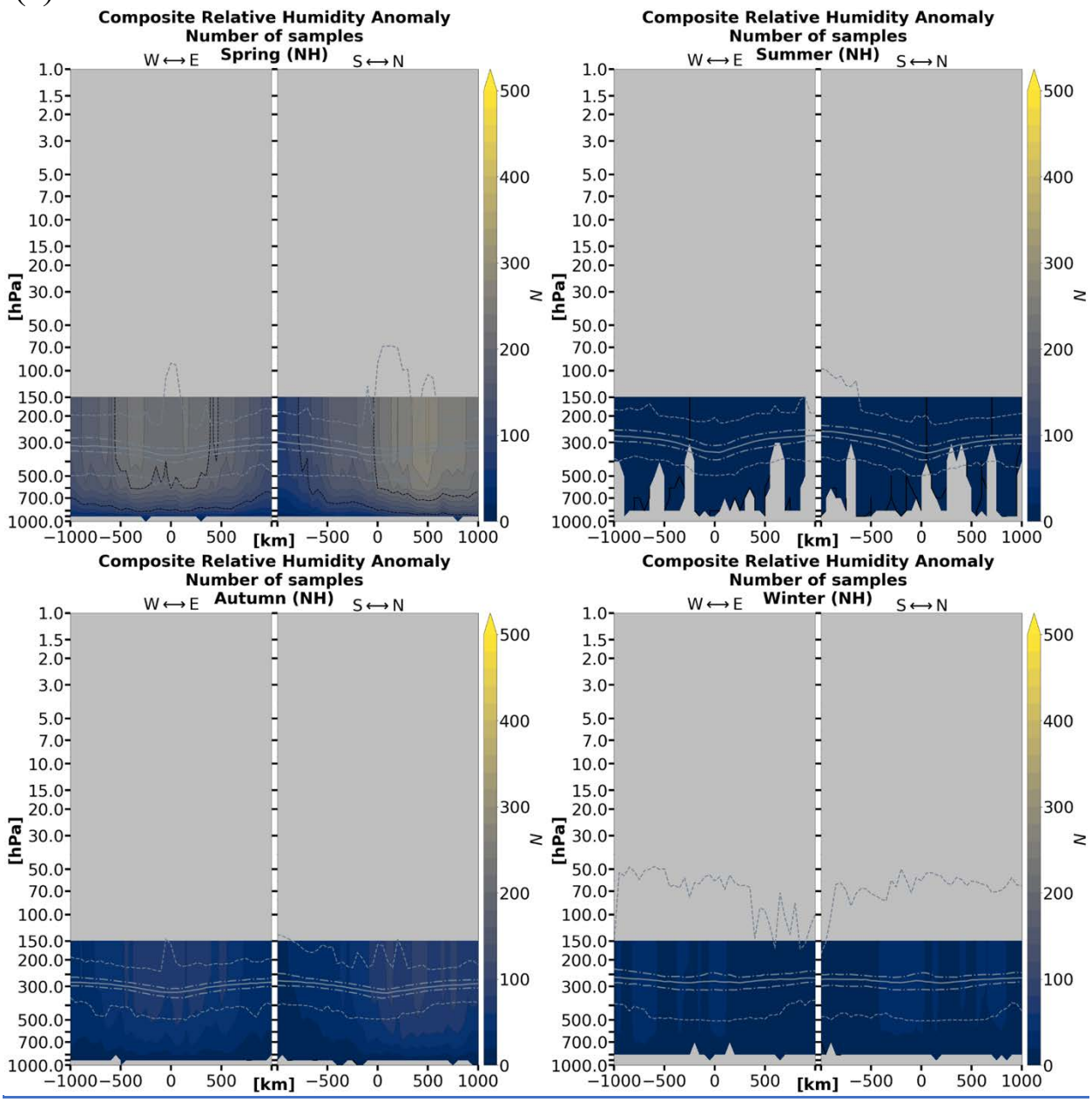

Figure 3.4.2: Sample size for each x–y–pressure-level grid point corresponding to (a) the Northern Hemisphere and (b) the Southern Hemisphere TPV relative humidity anomalies in **Figure 3.4.1.** The grey solid line indicates the thermal tropopause median; the long (short) dashed grey lines indicate the thermal tropopause interquartile range (minima and maxima).

(b)

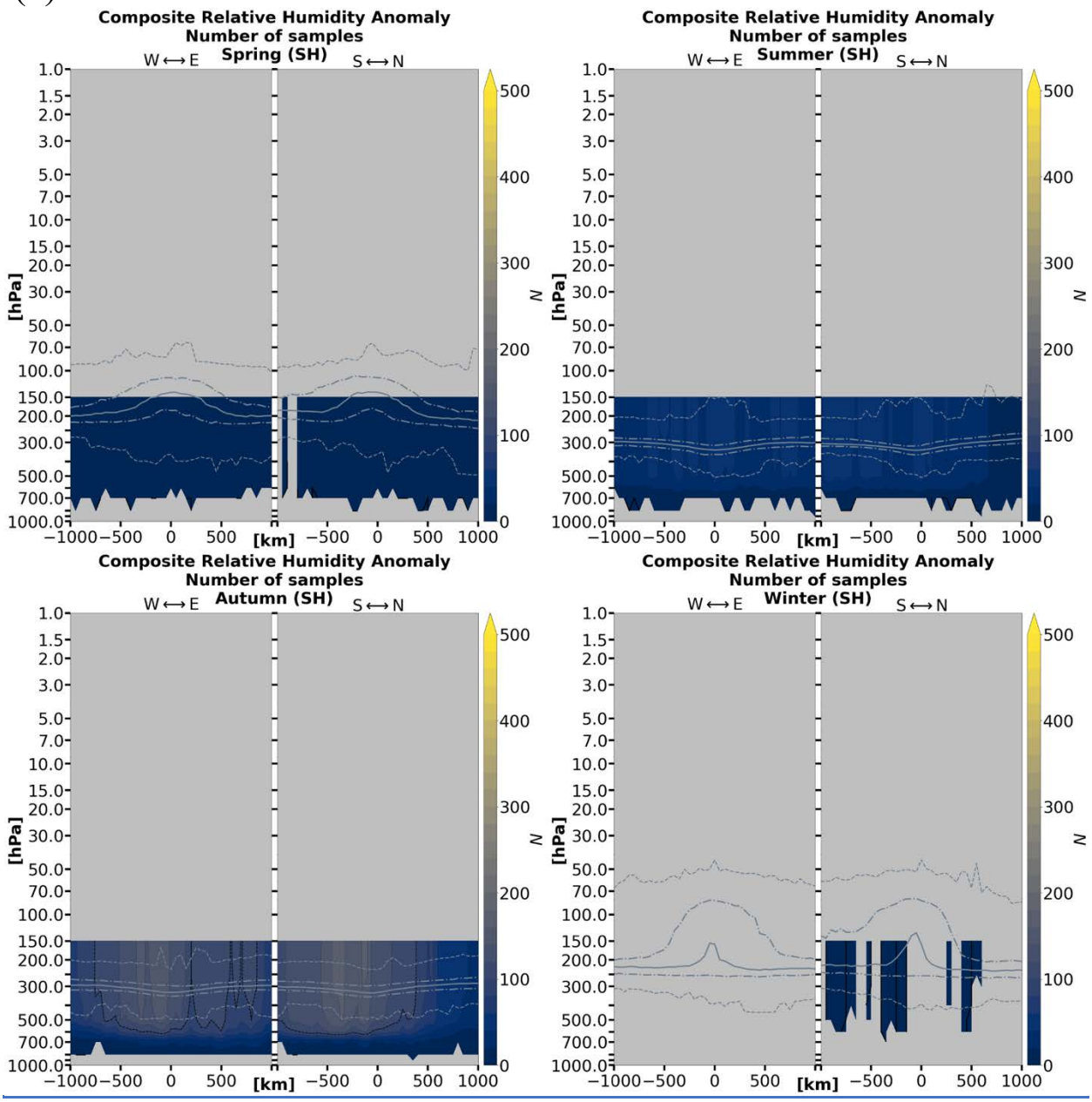

Figure 3.4.2 (continued)

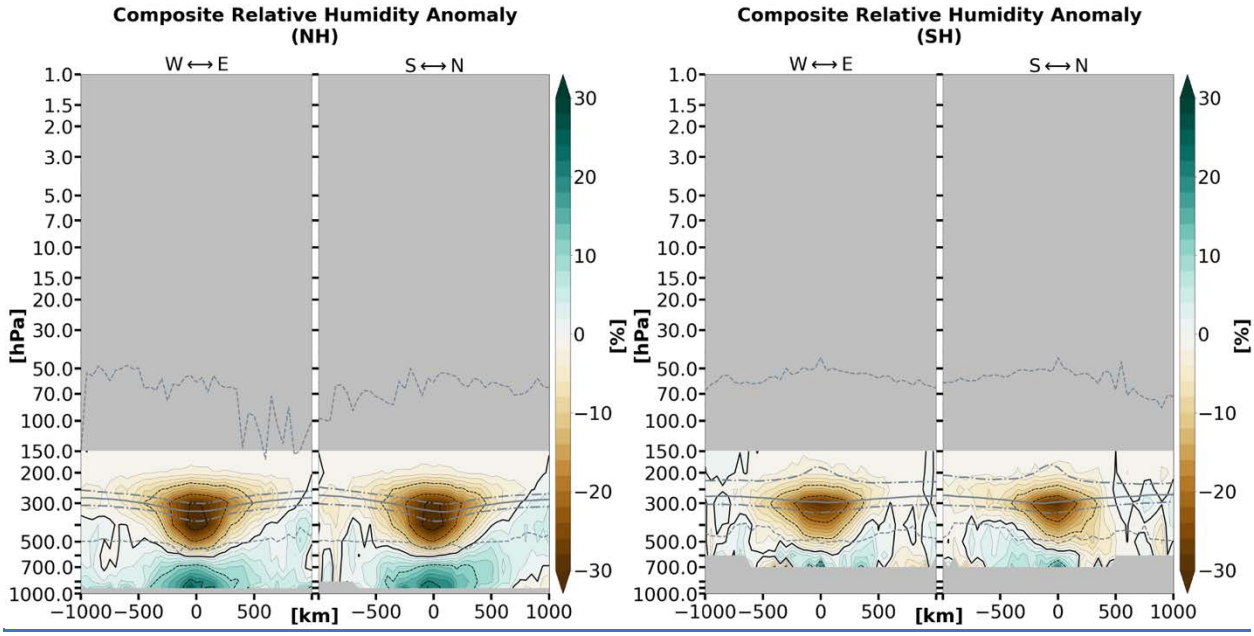

Figure 3.4.3: Composite relative humidity anomaly cross-sections for TPVs under AIRS/AMSU averaged over the 1-year-long study period, separated by hemisphere. Each contributing sample is weighted equally (i.e., seasons are not weighted equally due to different sample sizes between seasons). The grey solid line indicates the thermal tropopause median; the long (short) dashed grey lines indicate the thermal tropopause interquartile range (minima and maxima).

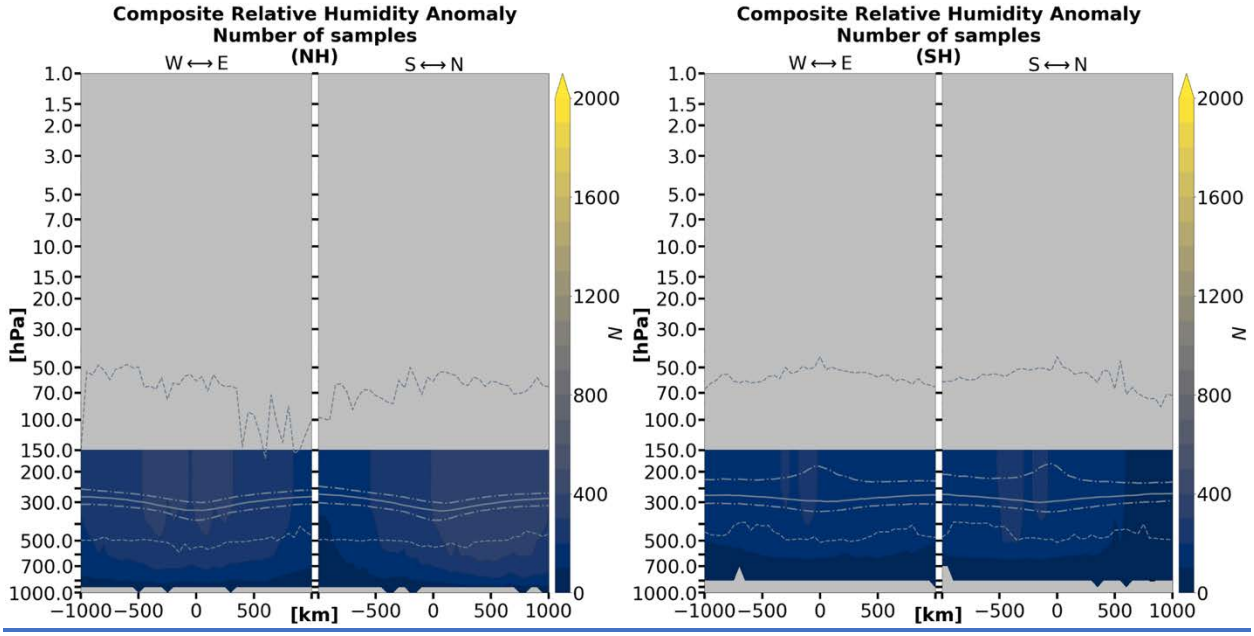

Figure 3.4.4: Sample size for each x–y–pressure-level grid point corresponding to **Figure 3.4.3** over the 1-year-long study period. Note that areas where N < 20 are masked in **Figure 3.4.3**. The grey solid line indicates the thermal tropopause median; the long (short) dashed grey lines indicate the thermal tropopause interquartile range (minima and maxima).

Section 3.5: Ozone volume mixing ratio anomalies and relative change in the Northern Hemisphere

The ozone VMR anomalies, relative change, and sample sizes for Northern Hemisphere TPVs are shown in **Figures 3.5.1, 3.5.2,** and **3.5.3**. Errors are not available for ozone VMR in the AIRS/AMSU L2 product, but ozone profiles have a general percent error of 15% at 70–250 hPa (Thrastarson et al. 2020). Southern Hemispheric TPVs by season are not treated in this study due to the lack of data.

Ozone VMR becomes prone to sampling error at all layers in all seasons. The sample sizes for individual seasons are very small (usually less than N = 10) (**Figure 3.5.3**) and data becomes absent in the winter. The other three seasons exhibit positive ozone anomalies (**Figure 3.5.1**) and relative change (**Figure 3.5.2**) in the layers below the 100 hPa level. Small negative ozone relative changes are visible in the summer and autumn seasons.

Year-long ozone VMR anomaly and relative change composites are illustrated respectively in **Figures 3.5.4 and 3.5.5**; however only the spring, summer, and autumn seasons have a non-negligible contribution to the total Northern Hemisphere composites. Corresponding sample size is shown in **Figure 3.5.6**. A possible ozone VMR "dipole" is visible in both the anomaly and relative change composites, however the negative ozone relative change is less apparent in the latter. Negative ozone anomalies and relative change in the mid-stratosphere are negligible or absent in the spring season but appear to become increasingly negative over the summer and fall. There is the caveat of very small sample sizes for individual seasons and the absence of data for the winter season. The ozone VMR anomaly and relative change are most negative in the layers between 7 hPa and 30 hPa.

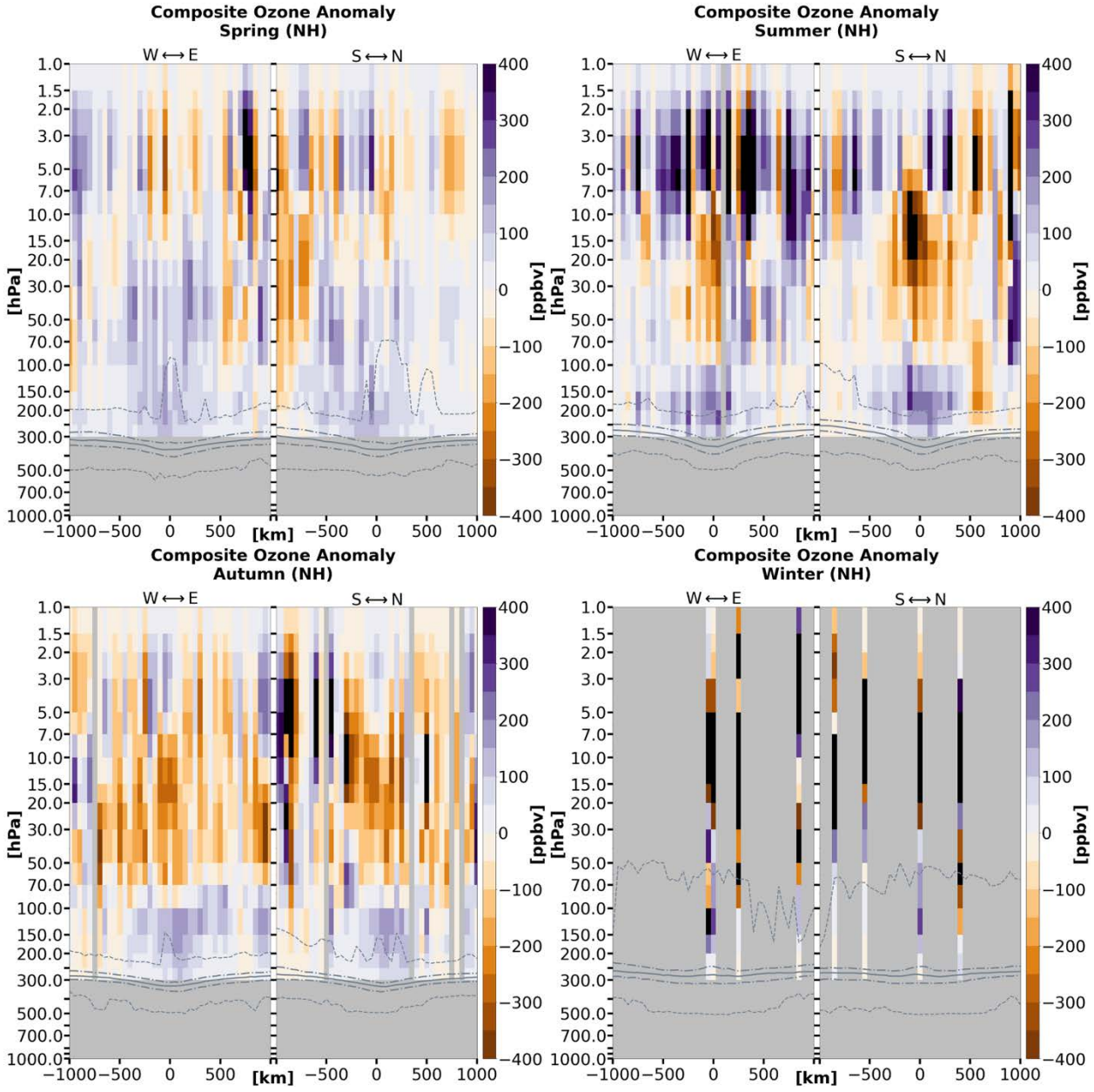

Figure 3.5.1: Composite ozone volume mixing ratio anomaly cross-sections by season for TPVs in the Northern Hemisphere under AIRS/AMSU. Anomalies are with respect to a 15-day mean background. Because of small sample size (see **Figure 3.5.3**), all data cells are shown, including those with sample sizes of N < 20. The grey solid line indicates the thermal tropopause median; the long (short) dashed grey lines indicate the thermal tropopause interquartile range (minima and maxima).

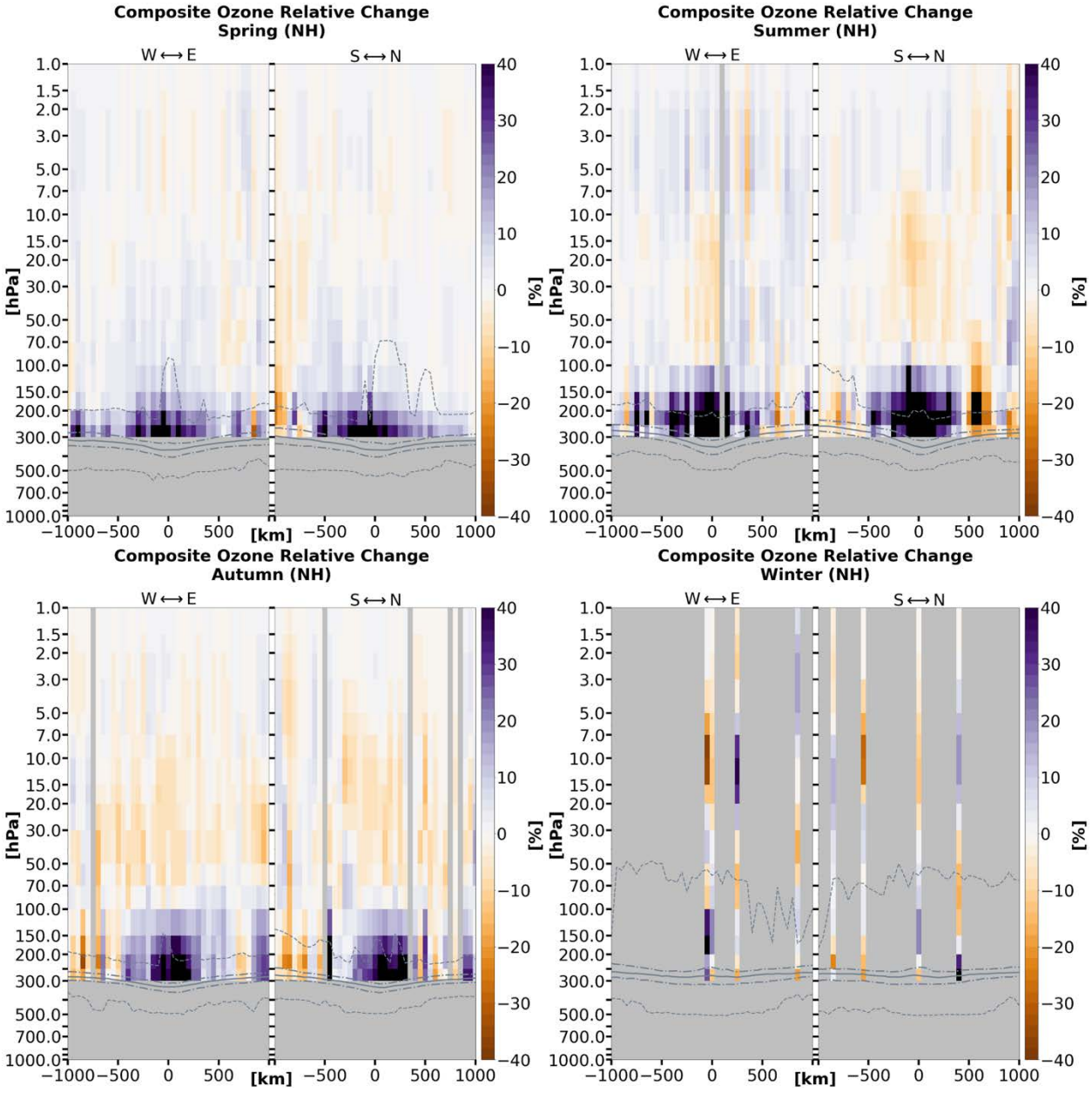

Figure 3.5.2: As in **Figure 3.5.1**, but for relative percent change.

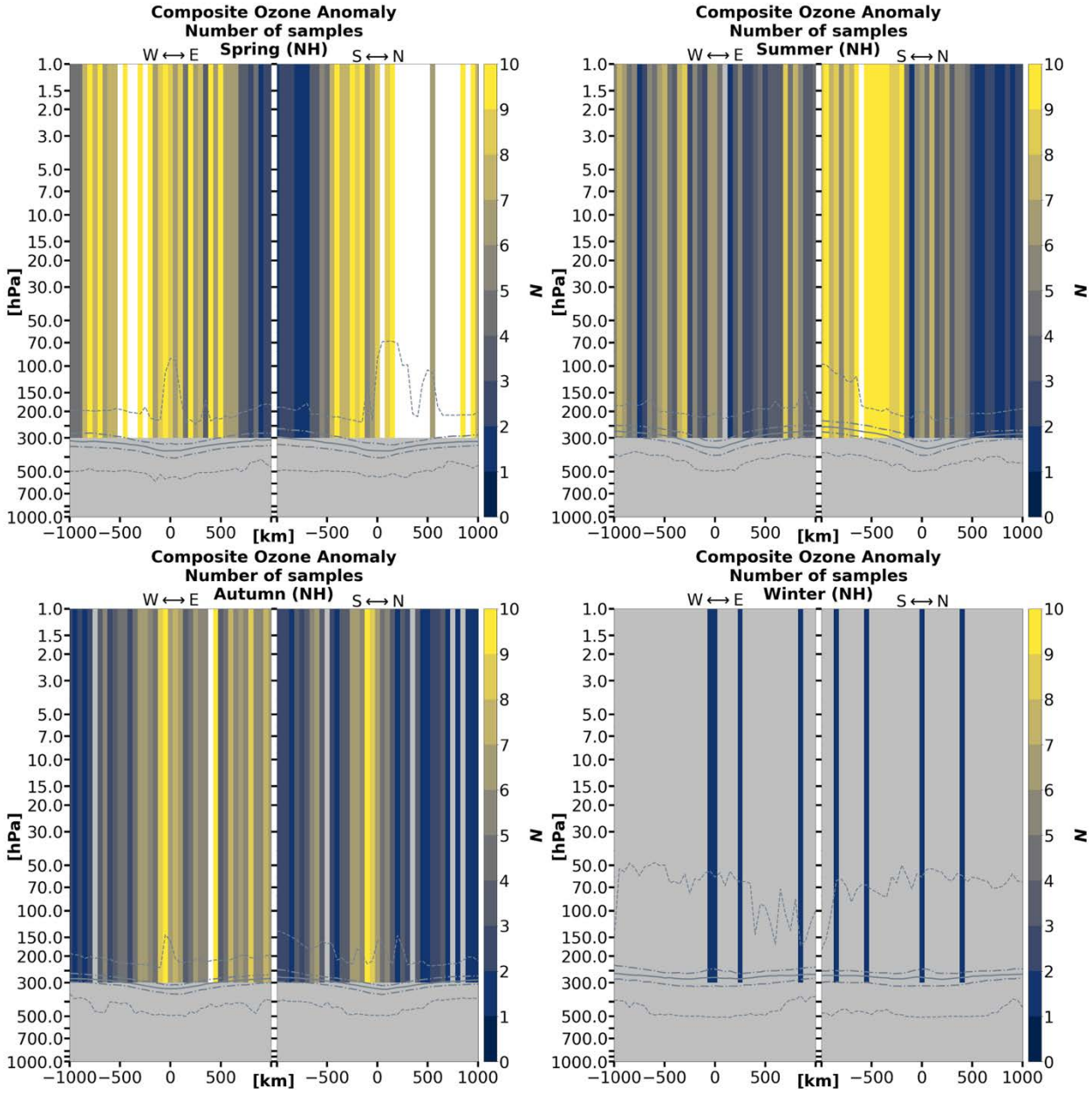

Figure 3.5.3: Sample size for each x–y–pressure-layer grid cell corresponding to both the Northern Hemisphere TPV ozone volume mixing ratio anomalies and relative change in **Figures 3.5.1** and **3.5.2**, respectively. Note the small sample sizes. The grey solid line indicates the thermal tropopause median; the long (short) dashed grey lines indicate the thermal tropopause interquartile range (minima and maxima).

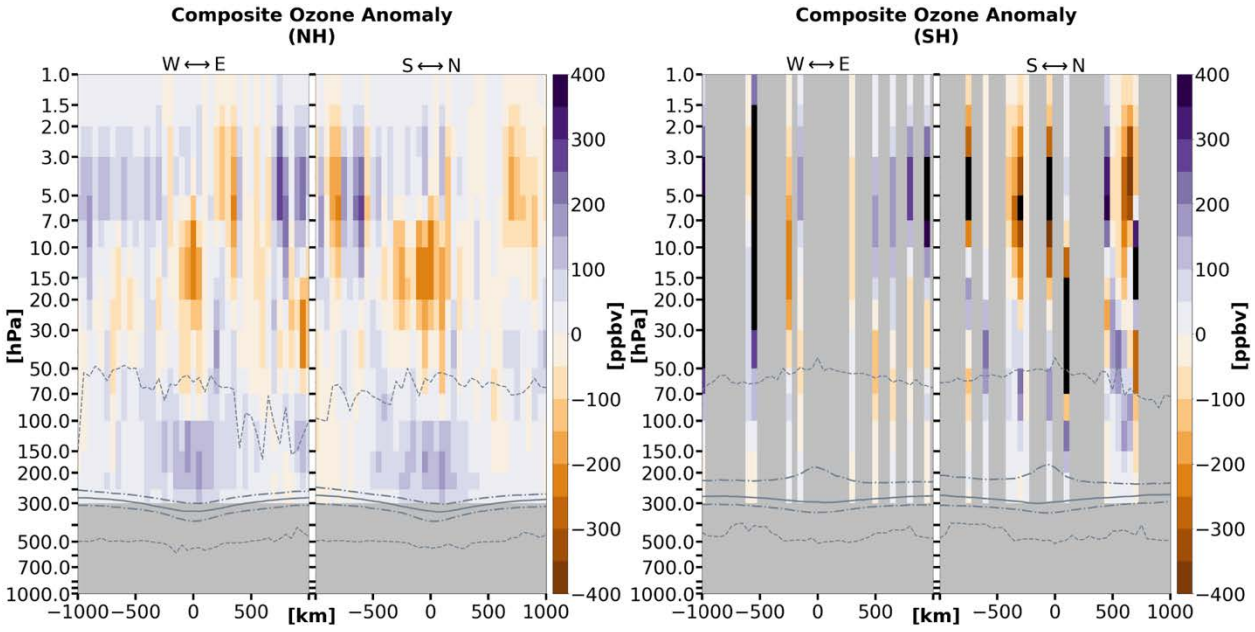

Figure 3.5.4: Composite ozone volume mixing ratio anomaly cross-sections for TPVs under AIRS/AMSU averaged over the 1-year-long study period for both hemispheres. The Southern Hemisphere is also shown to illustrate a lack of data over that hemisphere. Each contributing sample is weighted equally (i.e., seasons are not weighted equally due to different sample sizes between seasons). Because of small sample size (see **Figure 3.5.5**), all data cells are shown, including those with sample sizes of N < 20. The grey solid line indicates the thermal tropopause median; the long (short) dashed grey lines indicate the thermal tropopause interquartile range (minima and maxima).

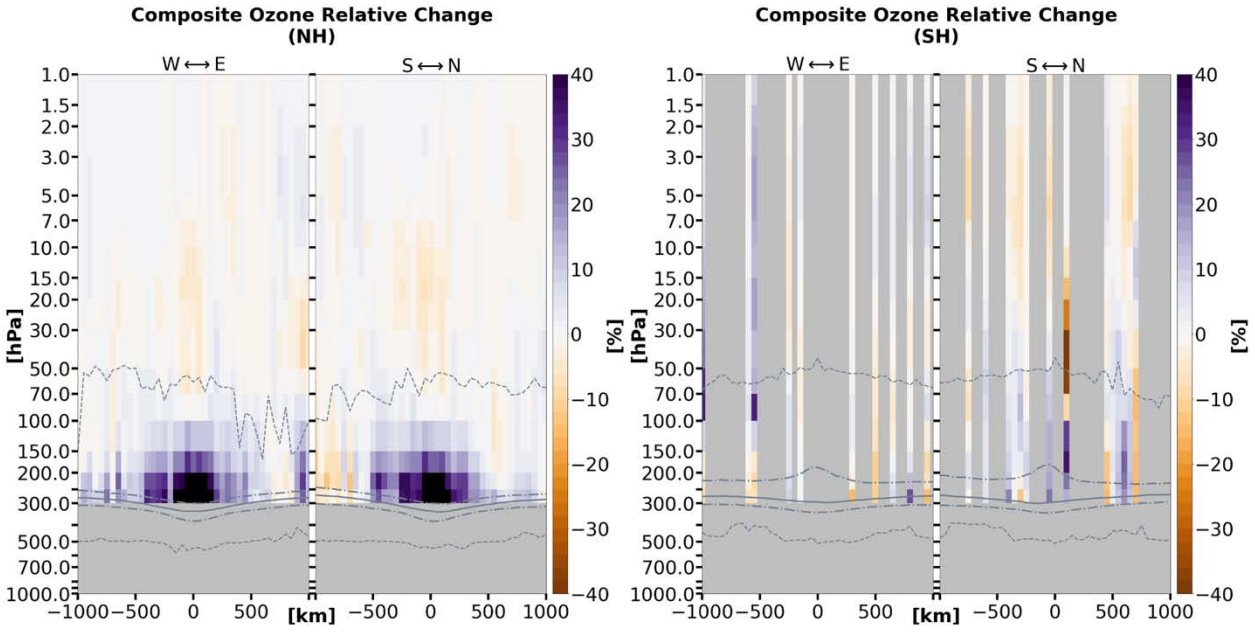

Figure 3.5.5: As in **Figure 3.5.4**, but for relative percent change.

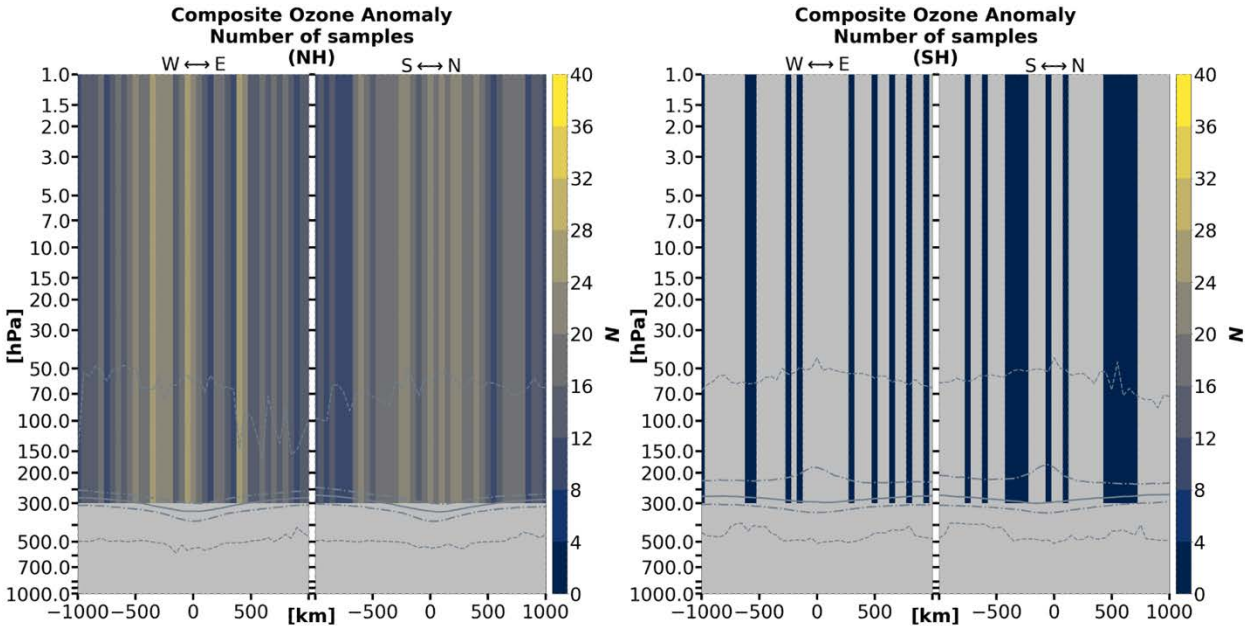

Figure 3.5.6: Sample size for each x–y–pressure-layer grid cell corresponding to **Figures 3.5.4 and 3.5.5** over the 1-year-long study period. The grey solid line indicates the thermal tropopause median; the long (short) dashed grey lines indicate the thermal tropopause interquartile range (minima and maxima).

Chapter 4

Discussion

The first two hypotheses treated in this study involve the comparison of this study's overall TPV composite anomaly structure to two prior studies that respectively utilize numerical models (e.g., Cavallo and Hakim (2010)) and ground-based observations over Summit Station, Greenland (Borg, Cavallo, and Turner 2020). The results of this present study are generally consistent with the two previous studies. That is, the overall temperature structure consists of anomalously high (low) temperatures above (below) the dynamic tropopause, and the overall relative humidity structure consists of anomalously low (high) relative humidity values above (below[12]) the dynamic tropopause. The low (high[13]) relative humidity anomalies are also shifted to slightly lower altitudes relative to the high (low) temperature anomalies. Differences between studies do exist and will be further discussed later in the chapter.

The third hypothesis in this study differs markedly from the first two, involving a direct comparison of the TPV anomaly structure between the Northern and Southern Hemispheres. Differences in the temperature anomaly structure between hemispheres is evident across all seasons, except for the cold anomaly in the spring season. Differences in the profiles of mixing ratio anomaly and relative change between hemispheres are restricted to the autumn season because there is insufficient data to create an anomaly composite in either one of the two hemispheres for the other three seasons.

Differences of TPVs between hemispheres largely appear to be mostly attributed to the magnitudes of the anomalies and relative change. A more qualitative conclusion can be drawn for the temperature anomaly structure–the magnitudes of the temperature anomalies for TPVs in the Northern Hemisphere are largely more variable than TPVs in the Southern Hemisphere. This suggests a contradiction to a study of TPVs over the Southern Hemisphere, in which the TPV maximum potential temperature anomaly exhibits high seasonal variability (Gordon, Cavallo, and Novak 2022).

The following discussion will go more in-depth to possible factors that contribute to the differences between this present study and those in Cavallo and Hakim (2010) and Borg, Cavallo, and Turner (2020). The following discussion will also explore some interpretation of the composite TPV anomalies and relative change for mixing ratio and ozone, and the relationship between mixing ratio and relative humidity structure within TPVs. Lastly, the biases that affect how well the TPV samples in this study represent the general population will be discussed, as well as possible causes to these biases.

[12] The positive relative humidity anomaly stated here applies only to Cavallo and Hakim (2010) and not Borg, Cavallo, and Turner (2020), where the positive relative humidity anomaly is absent.

[13] See the above footnote.

Section 4.1: Anomaly differences between studies

Between this present study and the studies conducted by Cavallo and Hakim (2010) and Borg, Cavallo, and Turner (2020), the most notable disparity is found in the TPV relative humidity anomaly composites. TPV composites over the Canadian Arctic exhibit a relative humidity anomaly below the dynamic tropopause that is positive both below and to the east of the of the TPV center (Cavallo and Hakim 2010), whereas TPV composites under AIRS/AMSU show a more symmetric horizontal distribution of positive relative humidity anomalies in the troposphere. Over Summit Station, Greenland, the absent positive relative humidity anomaly below the tropopause (Borg, Cavallo, and Turner 2020) is present in the TPV composites under AIRS/AMSU.

Disparities in the relative humidity anomaly structure can be partially attributed to the geographic sampling. The study by Cavallo and Hakim (2010) is restricted to the Canadian Arctic, where TPVs can be expected to advect moisture from the Hudson Bay, the Atlantic Ocean[14] northward on the eastern side. This would be a likely cause of the asymmetric relative humidity anomaly distribution below the dynamic tropopause. The study by Borg, Cavallo, and Turner (2020) is restricted to the Greenland ice sheet, residing at an elevation of over 3 km above sea level. Moisture advection to this high-altitude environment is expected to be unlikely and would be a plausible explanation for the missing positive relative humidity anomaly below the dynamic tropopause.

The geographic sampling for the TPVs considered under AIRS/AMSU in this present study are generally evenly distributed in longitude, but are clustered along the ~80˚ latitude, due to the nature of Aqua's orbit. This is likely to influence the TPV composite to overrepresent (underrepresent) TPVs from "hotspots" that are closer to (further from) the ~80˚ parallel (see **Figures 2.3.1 and 2.3.2**). The combined geographic effects on the TPV composites derived from AIRS/AMSU data are complex and will not be discussed further.

Minor differences between the TPVs in this present study and those in Cavallo and Hakim (2010) and Borg, Cavallo, and Turner (2020) are found in the magnitudes and vertical placements of the anomaly extrema and the horizontal extent of the anomalies. Explanations for these differences are multifactorial. One of these factors may be the more minute effects of geographic sampling between studies, as previously discussed.

Differences can also be attributed to how well numerical models can reproduce real-world phenomena like TPVs, especially over the data-sparse Arctic and Antarctic. The study conducted in Cavallo and Hakim (2010) is based on a forecast model, which may be prone to parameterizations that may not capture the full complexity of the state of the atmosphere.

There is a difference of ~7–8 years between the study conducted by Cavallo and Hakim (2010) and the present study. In the context of climatic change and Arctic amplification, a warmer troposphere would imply a raising in altitude of the tropopause, which may cause an upward shift in the anomaly pattern. **Figure 3.1.1** indicates an apparent raising of the background tropopause in the time frame between the two studies for the winter season. However, there is a noticeable *lowering* of the background tropopause over the summer season. In this study's seasonal temperature composites (**Figure 3.2.1**), the temperature anomaly "dipole" pattern is raised (lowered) in altitude in the winter (summer) seasons relative to the corresponding seasonal composites from Figure 14 in Cavallo and Hakim (2010). The lowering

[14] This is inclusive of Baffin Bay, the Davis Strait, and the Labrador Sea.

of the summer background tropopause over time may either be due to other factors that have a stronger influence upon the differences between composites, or that the response of the Arctic tropopause to global warming is more complex (e.g., Francis and Vavrus (2012)).

Yet another factor influencing anomaly differences between studies may be the differences in methodology in calculating the background. For example, a 5-day mean background was used to compute anomalies over Summit Station, while a 15-day mean background was used for AIRS/AMSU observations. A longer window may result in anomalies incorporating not only the TPV but a fraction of the background trough as well, thus altering anomaly magnitudes.

Temperature anomaly composites over the summer, winter, and year-long period (**Figures 3.2.1 and 3.2.5**) indicate that negative TPV anomaly minimum are approximately half the anomaly magnitudes of the corresponding composites in Figures 9 and 14 in Cavallo and Hakim (2010). When taking **Figure 3.1.1** into consideration, the decrease in negative temperature anomaly magnitude for TPVs under AIRS/AMSU can be attributed to either a tropospheric increase in temperature at the vortex center and/or a tropospheric decrease in background temperature at the vortex center relative to in Cavallo and Hakim (2010). There does not appear to be a clear pattern between seasons, so the difference in TPV temperature anomaly minima between this study and Cavallo and Hakim (2010) does not have a clear identifiable explanation.

It is interesting to note that the TPV anomalies in Borg, Cavallo, and Turner (2020) share similar magnitudes with TPV anomalies over the Antarctic in this present study. As with Greenland, East Antarctica contains a large continental ice sheet and high surface elevations. Moreover, the positive relative humidity anomaly for TPVs in the Southern Hemisphere, although present, appears to be partially obscured (see **Figure 3.4.1**) with an indeterminate relative humidity maximum.

Section 4.2: Structure of water vapor and ozone

This study considers the distribution of mixing ratio and ozone VMR within the interiors of TPVs. Dry "monopole" mixing ratio structures centered just above the TPV tropopause become most apparent when considering the relative change (or percent change) of mixing ratio relative to the background. This dry structure is due to downward stratospheric intrusion, and roughly collocates with the maximum PV anomaly in Figure 9c of Cavallo and Hakim (2010). Just below the mixing ratio relative change minimum, there is an increase in the vertical water vapor gradient with respect to height across the dynamic tropopause. The vertical position of where the gradient is steepest would collocate with the vertical position of the largest rates of PV growth for intensifying TPVs. Moreover, the steeper water vapor gradient allows LW radiation from lower levels to escape into space more easily. As a result, LW cooling is more concentrated to lower levels, contributing to maintaining TPV strength (Cavallo and Hakim 2013, 2010).

The dry "monopole" mixing ratio anomaly (relative change) pattern centered below (on) the dynamic tropopause contrasts the relative humidity anomaly "dipole" above and below the dynamic tropopause, suggesting that the tropospheric positive relative humidity anomaly below the TPV core is primarily driven by the negative temperature anomaly. More specifically, the saturation mixing ratio decreases exponentially as temperature decreases linearly as per the Clausius-Clapeyron relation, which is why relative humidity increases with decreasing temperature if mixing ratio remains constant. Although the mixing ratio also decreases with a negative relative change at the TPV core, this does not fully offset the larger magnitude negative relative change of the saturation mixing ratio, so the tropospheric relative humidity still increases under the TPV center.

An interesting finding in this study is the ozone VMR anomaly and relative change structure in the Northern Hemisphere. Higher anomalous and relative concentrations of ozone were expected with the downward intrusion of stratospheric air; however, the tentative dry anomaly in the mid-stratosphere was not expected. This could possibly be an artifact. If real however, it raises questions regarding possible interactions, if any, between TPVs and the mid-stratosphere. A negative-over-positive ozone anomaly "dipole" would concentrate heating from SW radiation to the lower stratosphere toward the TPV warm anomaly, while the mid-stratosphere over the TPV would be subject to greater LW cooling. While the vertical ozone distribution in this study differs slightly from the ozone initialization in Cavallo and Hakim (2013), any influence on TPV evolution may still be negligible.

The low sample size of the ozone VMR anomalies is a major limitation, due to the fact that AIRS/AMSU ozone retrievals are not reliable when the surface skin temperature falls below 240 K (Thrastarson et al. 2020). This becomes an issue over high-latitude regions, which are inherently cold. Moreover, since Antarctic temperatures are generally colder than Arctic temperatures (see **Figure 2.3.3**), ozone anomalies are virtually and unsurprisingly absent for TPVs in the Southern Hemisphere (**Figure 3.5.6**). Whether this "dipole" exists or not would require studies with much larger sample sizes[15] and significance testing.

[15] Direct composites of ozone VMR (Appendix A) provide further evidence that a "dipole" exists in the Northern Hemisphere summer and autumn seasons and are not as limited by sample size.

Section 4.3: Limitations of sample representation

In this study, 2378 Northern Hemispheric TPV samples and 2312 Southern Hemispheric TPV samples were composited from AIRS/AMSU observations. Since only higher-amplitude (≥ 10 K) and larger-scale (≥ 200 km) were considered, it is assumed that the composites in this study are representative of only larger and higher intensity TPVs. Considering only TPVs with ≥ 10 K amplitude and ≥ 200 km equivalent radius, Section 2.3 reveals that the 2378 (2312) Northern (Southern) Hemispheric TPV samples have amplitude distributions that are not significantly different from that of the general population output by TPVTrack ($p > 0.1$). Section 2.3 also reveals that the equivalent radius distribution of the TPV cases considered for this study is significantly different ($p < 10^{-5}$) from that of the general population for either hemisphere. Judging from the histograms presented in **Figures 2.3.5 and 2.3.6**, it can be assumed that the TPV composites presented in this study are representative of the general population in the vertical direction but are biased to TPVs with smaller (larger) equivalent radii in the Northern (Southern) Hemisphere relative to the total population of higher-amplitude, larger-scale TPVs from TPVTrack.

The anomaly composites presented in this study have been shown to be composed of TPV cases that are unevenly distributed throughout the one-year study period. It is shown from **Figure 3.2.2** that TPV temperature anomaly cases are represented less for the winter season in the Northern Hemisphere and for the winter and spring seasons in the Southern Hemisphere. The asymmetry in the seasonal distribution of TPV anomaly cases is even more extreme for water vapor. Anomaly cases are most heavily weighted to the spring (autumn) season, and virtually absent for the winter and summer (winter and spring) seasons in the Northern (Southern) Hemisphere. Thus, total year-long composites do not accurately represent TPV anomaly structure.

The seasonal asymmetry can most plausibly be due to the fact that AIRS retrievals perform worse in very cloudy environments with high optical depths (e.g., Joel Susskind, Barnet, and Blaisdell (2003); Thrastarson et al. (2021)). This also means that the sampling of TPV composites is biased to clear-sky cases. Over the Canadian Archipelago, where TPV density is high (see **Figure 2.3.1**), cloud cover is climatologically highest in the summer and lowest in the spring (Shupe et al. 2011). This may explain why TPV mixing ratio anomaly samples are absent in the summer and heavily skewed to the spring in the Northern Hemisphere. In the Antarctic, cloud cover is generally higher in the summer and autumn seasons than in the winter and spring seasons (Bromwich et al. 2012). However, this pattern does not correspond well with TPV anomaly cases in the Southern Hemisphere, so there may also be regional differences in cloud cover that are involved.

Section 4.4: Study summary

Tropopause polar vortices have presented a challenge to numerical weather forecasting (Cavallo and Hakim 2013), as well as climate models. Unlike linear Rossby waves, TPVs are highly non-linear solutions to the vorticity equation (Hakim 2000) and resolving them spectrally requires large amounts of computational resources to forecast (Hakim, Keyser, and Bosart 1996). The effects of TPVs are not restricted to the polar regions. They can be responsible for Rossby wave initiation events (e.g., Röthlisberger, Martius, and Wernli (2018)), serve as precursors to high-impact weather events including cold air outbreaks (e.g., Lillo et al. (2021)) and tornado outbreaks (e.g., Bray, Cavallo, and Bluestein (2021)) as well as climatologically important events such as sea-ice loss (e.g., Simmonds and Rudeva (2012)).

These has been considerable research of TPVs in numerical models (e.g., (Cavallo and Hakim 2013, 2010)), but observational verification is limited (Borg, Cavallo, and Turner 2020). This study has the purpose of furthering the observational knowledge of TPVs, utilizing the AIRS science team retrieval product from the AIRS and AMSU atmospheric profilers (J Susskind et al. 2020; Thrastarson et al. 2021). These tools are used in this study to produce an observation-based three-dimensional view of TPV structure.

A list of TPV cases was compiled for each hemisphere by first identifying TPV track locations (Szapiro and Cavallo 2018) from 2015–2016, followed by collocation of TPVs with Aqua satellite overpasses using GIS software (Esri 2011). A year-long study period from 1 September 2015 through 31 August 2016 was selected for this study.

Composites for TPV anomaly structure for temperature, water vapor mass mixing ratio, relative humidity, and ozone volume mixing ratio, and TPV relative change for water vapor mass mixing ratio and ozone volume mixing ratio were produces for the year-long period as well as for each season in both hemispheres.

There are some shortcomings and caveats that have arisen in this study. The biggest caveat concerns the sample size distribution and data availability for some of the variables. The sample distributions for the TPV moisture anomalies between seasons are highly asymmetric, with cases being concentrated to a single season (spring in the northern hemisphere; summer in the southern hemisphere), while other seasons having little to no data (summer in the northern hemisphere; winter in the southern hemisphere). As a result, year-long moisture composites are not accurate representations of the TPVs average throughout the year. Composites of TPV ozone anomalies and relative change severely suffered from low sample sizes across the whole year-long period of this study. No meaningful composites could be created for Northern Hemisphere winter TPVs nor Southern Hemisphere TPVs across all seasons.

The temperature and relative humidity anomaly structure for TPVs under AIRS/AMSU qualitatively confirmed the structure produced in previous model studies (Cavallo and Hakim 2013, 2010) and observational studies (Borg, Cavallo, and Turner 2020). The largest differences between this study and previous studies include a more symmetrical tropospheric relative humidity anomaly structure versus the east-west asymmetric tropospheric relative humidity anomaly structure in Cavallo and Hakim (2010), and the presence of a positive relative humidity anomaly below the tropopause that was largely absent in Borg, Cavallo, and Turner (2020). Other composite differences between studies were minor, mainly limited to the vertical positions of temperature and relative humidity anomaly extrema. Comparison of relative humidity anomalies was limited by the seasonally skewed anomaly samples for the TPVs under AIRS/AMSU that were considered for this study.

TPVs in this study were also characterized by a dry mixing ratio relative change over the tropopause of the TPV center, consistent with the presence of steeper vertical water vapor gradients found in previous studies (Cavallo and Hakim 2013). TPVs in the Northern Hemisphere exhibit an increase in ozone concentration through the upper troposphere and lower stratosphere, and a possible decrease in ozone concentration in the mid-stratosphere.

Composite TPV structure was compared between TPVs in the Northern and Southern Hemispheres. Temperature anomalies in Northern Hemisphere TPVs were generally larger in magnitude and displayed more inter-seasonal variability than Southern Hemisphere TPVs. Northern Hemisphere TPVs also have larger magnitude mixing ratio anomalies and relative change than Southern Hemisphere TPVS for at least the autumn season.

The results of this study are summarized below:

Question: Is the overall composite structure of TPVs characterized in numerical model studies reproducible using AIRS/AMSU-derived observations?

Hypothesis: There will be no notable difference in the overall structure of the temperature nor the humidity profiles other than a difference in magnitude.

Result: The hypothesis is confirmed for temperature anomalies and stratospheric relative humidity anomalies and rejected for tropospheric relative humidity anomalies. Tropospheric relative humidity anomalies for Northern Hemisphere TPVs under AIRS/AMSU display more symmetry in structure than the tropospheric relative humidity structure of TPVs resolved from model studies.

Question: Is the overall composite structure of TPVs characterized from ground-based observations at Summit Station, Greenland consistent with TPVs characterized from AIRS/AMSU-derived observations?

Hypothesis: There will be no notable difference in the overall temperature structure other than a difference in magnitude. There are expected to be qualitative differences in the relative humidity profiles of TPVs between this study and a previous study conducted by Borg, Cavallo, and Turner (2020). TPVs over Greenland lack the anomalously high relative humidities in the lower troposphere that are present in TPVs over the Canadian Arctic, presumably due to the altitude of the local geography (Borg, Cavallo, and Turner 2020; Cavallo and Hakim 2010). Most AIRS/AMSU Arctic observations will be over low topography because most of the Arctic region is topographically low. The average Northern Hemisphere TPV in this study will therefore reflect a relative humidity profile of TPVs over low altitudes, such as those over the Canadian Arctic, rather than a relative humidity profile of TPVs over high altitudes, such as those over Greenland.

Result: The hypothesis is confirmed. There was no notable difference in temperature anomaly structure other than differences in magnitude. The positive relative humidity anomaly below the tropopause was present for Northern Hemisphere TPVs in this study while it was not present for TPVs over Summit Station, Greenland.

Question: Are there detectable differences in composite structure between TPVs of the Northern and Southern Hemispheres based on AIRS/AMSU-derived observations?

Hypothesis: There are expected to be measurable differences in the composite temperature profiles of TPVs between the Northern and Southern Hemispheres. The maximum amplitude and maximum θ anomaly distributions of TPV populations in the Northern and Southern Hemispheres have been shown to be statistically different across all seasons albeit being similarly shaped (Gordon, Cavallo, and Novak 2022), so TPV temperature profiles are expected to differ between hemispheres in this study. There will be no measurable difference in the overall structure of mixing ratio. Since humidity profiles of Southern Hemisphere TPVs have yet to be fully characterized, a null hypothesis for differences in mixing ratio is assumed.

Result: This hypothesis is rejected for temperature anomalies and inconclusive for mixing ratio anomalies and relative change. The magnitudes of the temperature anomalies across all seasons and the magnitudes of the mixing ratio anomalies and relative change in the autumn season are measurably different from those of TPVs in the Northern Hemisphere at levels/layers where anomalies are expected to be present (i.e., non-overlapping error bars). Comparisons for winter, spring, and summer mixing ratio anomalies and mixing ratio relative change were not possible due to insufficient data. The temperature anomaly profiles for TPVs in the Northern Hemisphere also exhibited larger inter-seasonal variability than the temperature anomaly profiles in Southern Hemisphere TPVs.

Appendix A

Composite Averages

As mentioned in Chapter 2, Section 2.5, direct composite averages for temperature, mixing ratio, relative humidity, and ozone VMR were not an area of focus in Chapter 3. Direct composite figures are shown in the following pages for each season and hemisphere. As with most anomaly and relative change composites in Chapter 3, direct composites in the following pages are masked for sample sizes of $N < 20$. For clarity reasons, level quantities have been used for all direct composites, including mixing ratio and ozone VMR. Level quantities reflect the same patterns found using layer quantities, although these patterns are less easily resolvable using layer quantities. Additionally, all figures include the median thermal tropopause (solid grey line), the thermal tropopause at the 25% and 75% quartiles (long dashed grey lines), and the thermal tropopause minima and maxima (short dashed grey line) for the corresponding season and hemisphere.

(a)

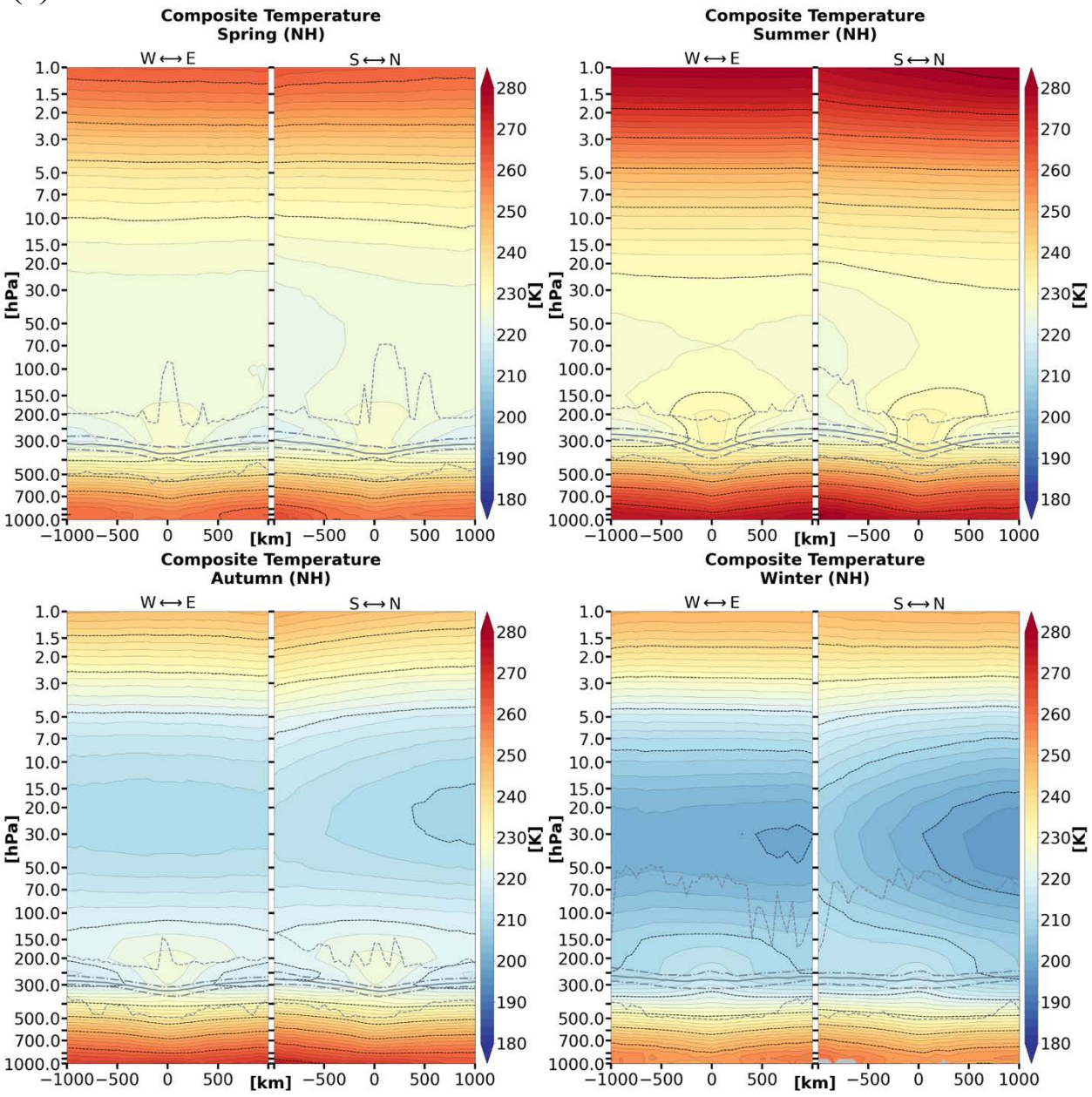

Figure A.1: Composite mean temperature of TPV cases by season and hemisphere.

(b)

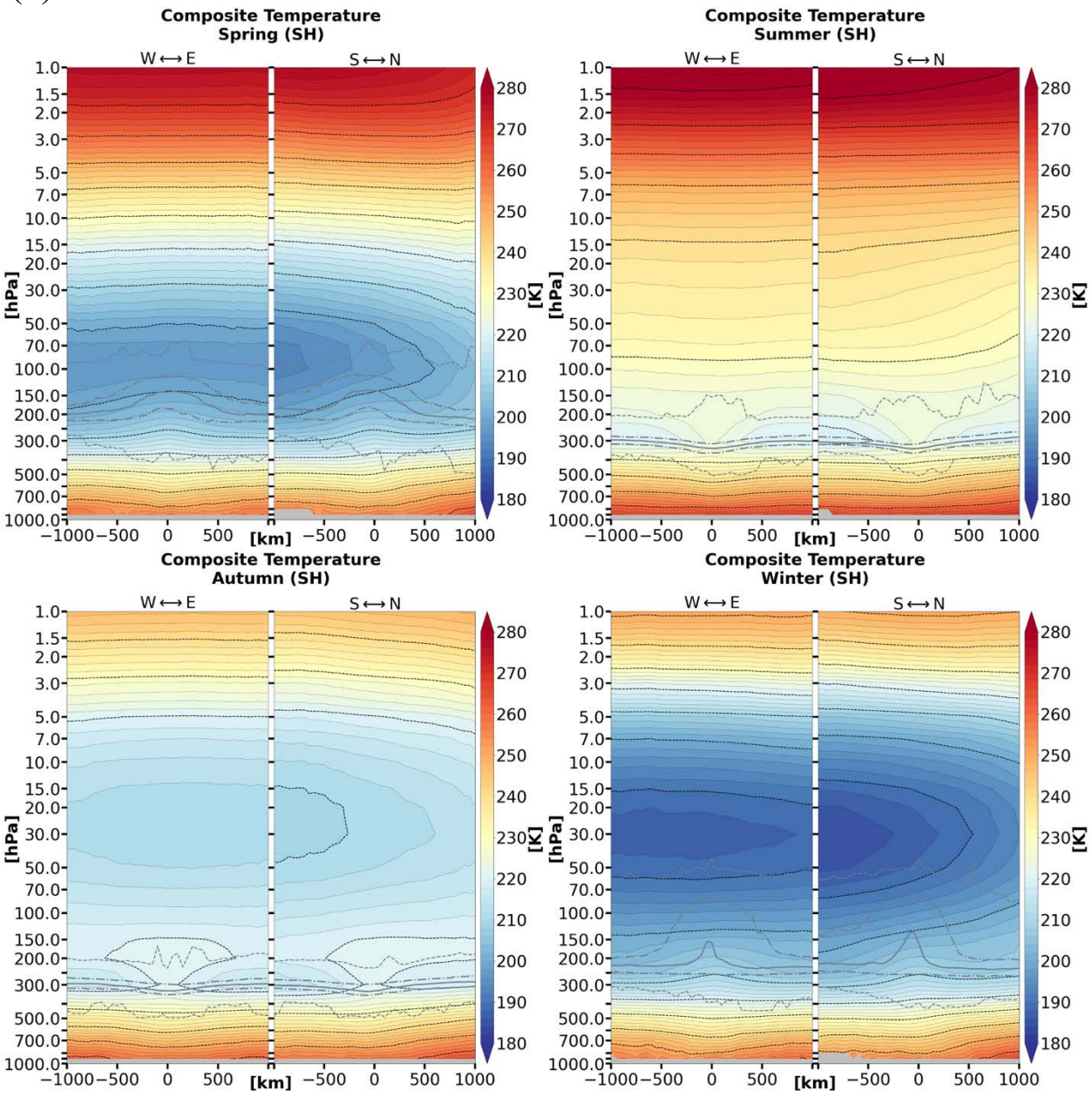

Figure A.1 (continued)

(a)

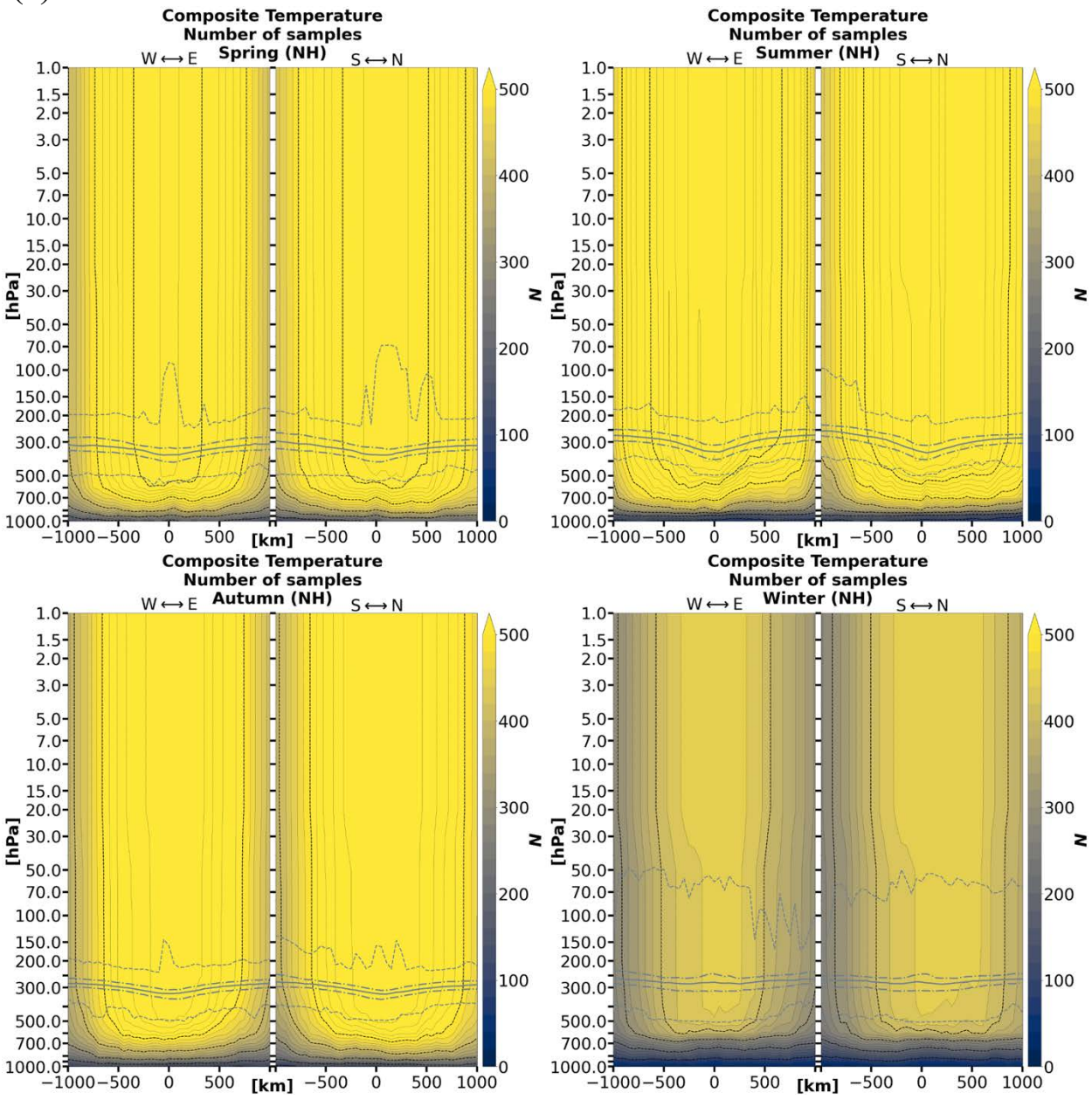

Figure A.2: Number of samples by grid point for the composite mean temperature of TPV cases by season and hemisphere.

(b)

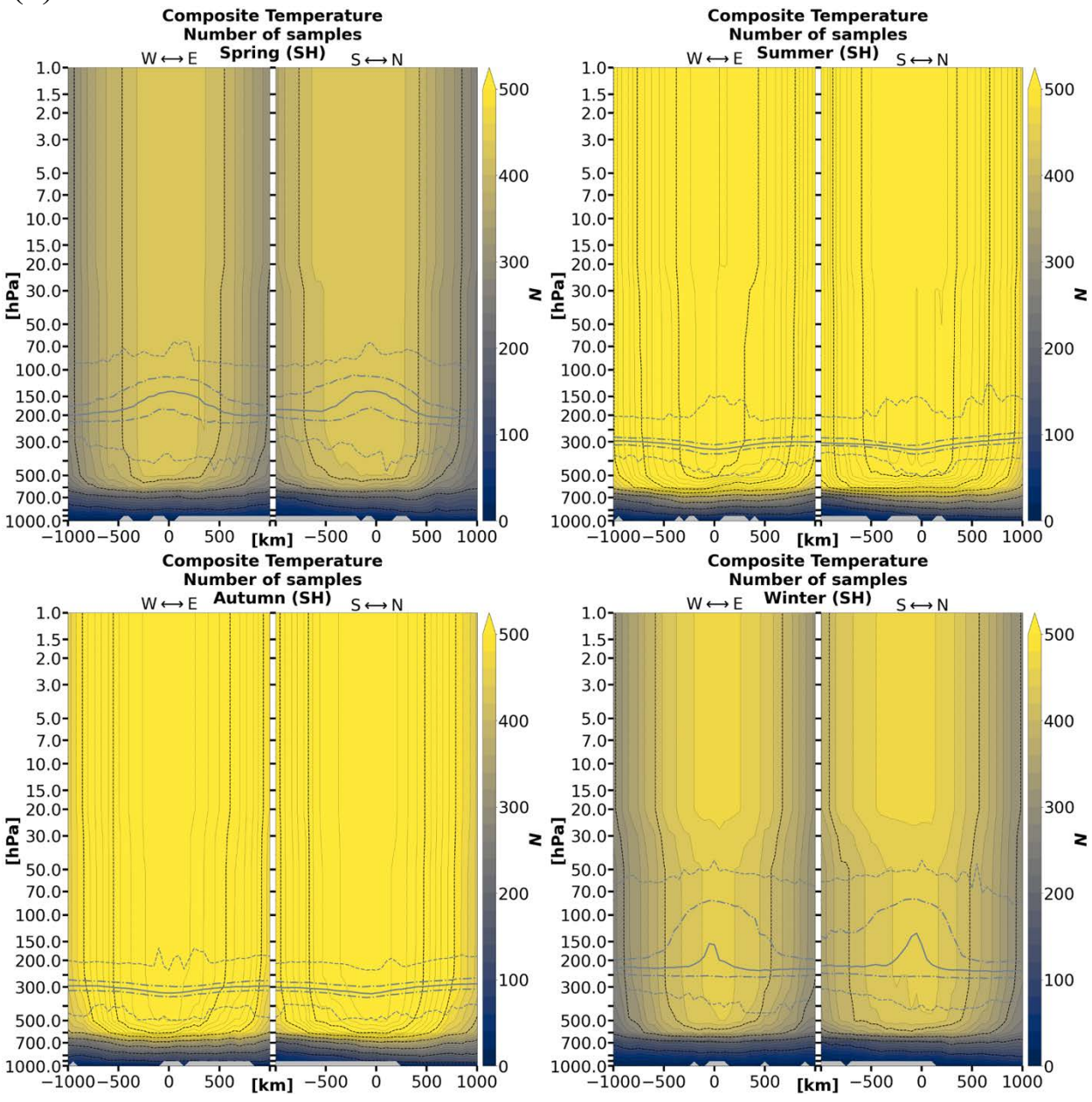

Figure A.2 (continued)

(a)

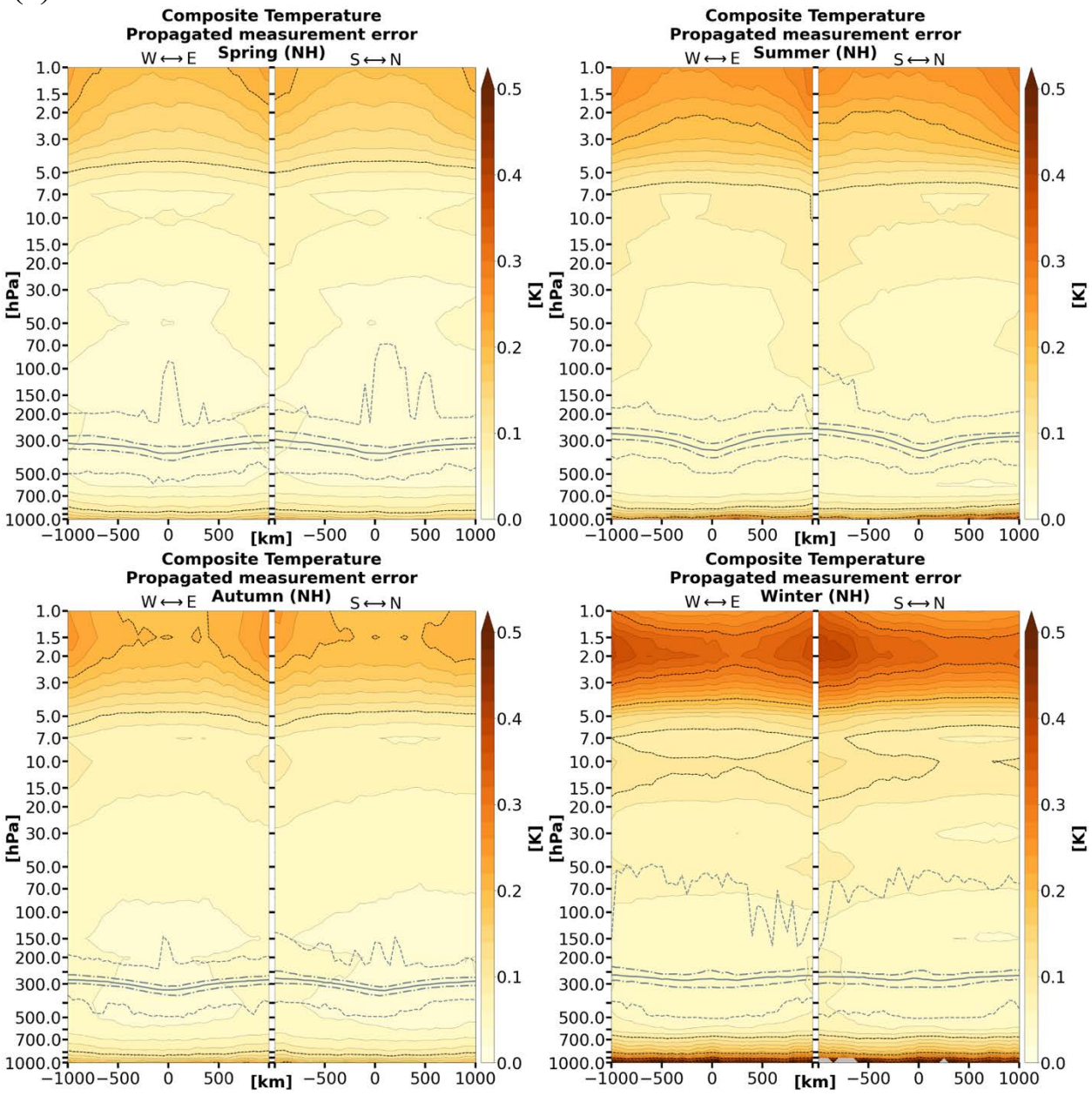

Figure A.3: Calculated error for the composite mean temperature of TPV cases by season and hemisphere.

(b)

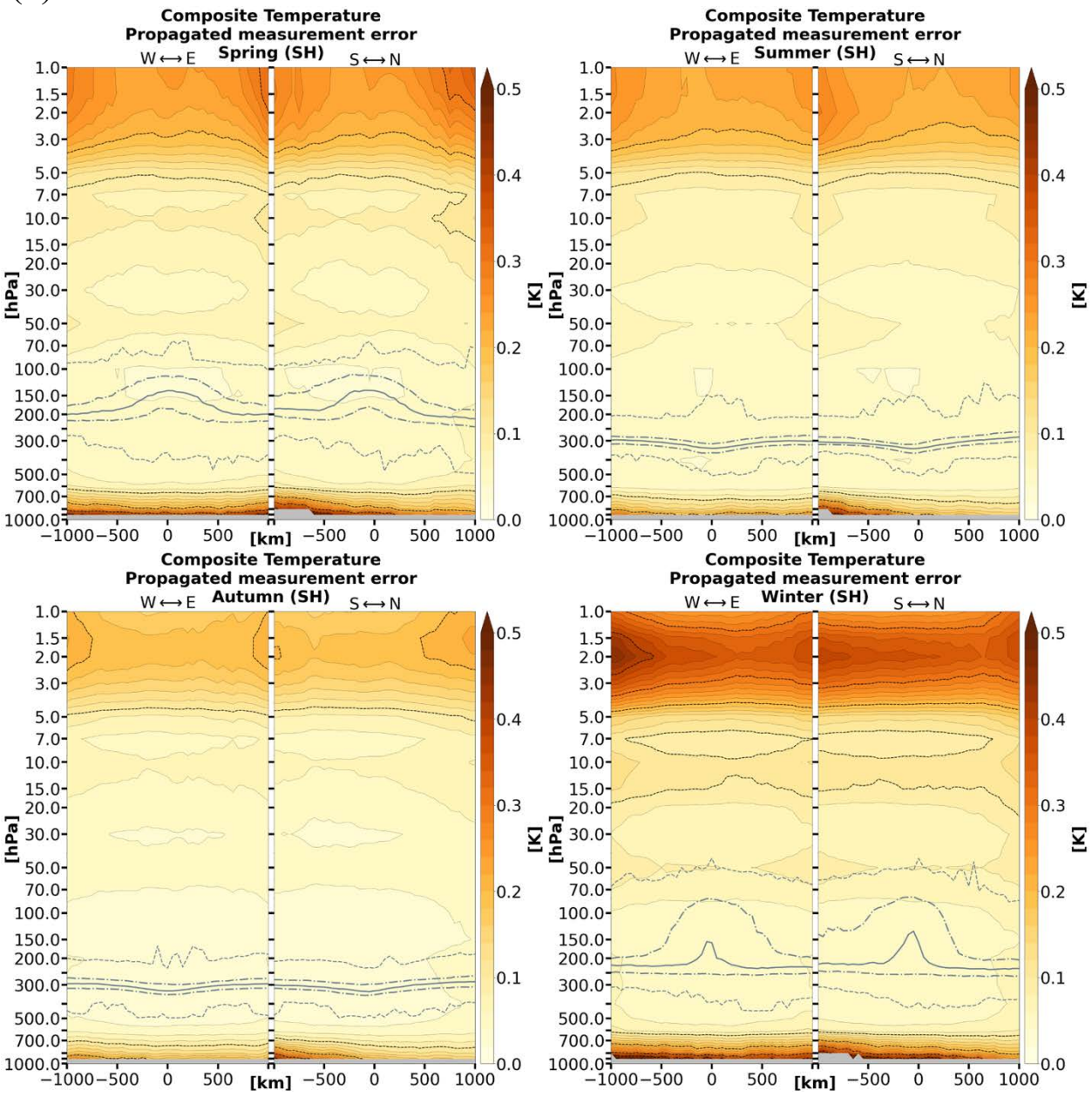

Figure A.3 (continued)

(a)

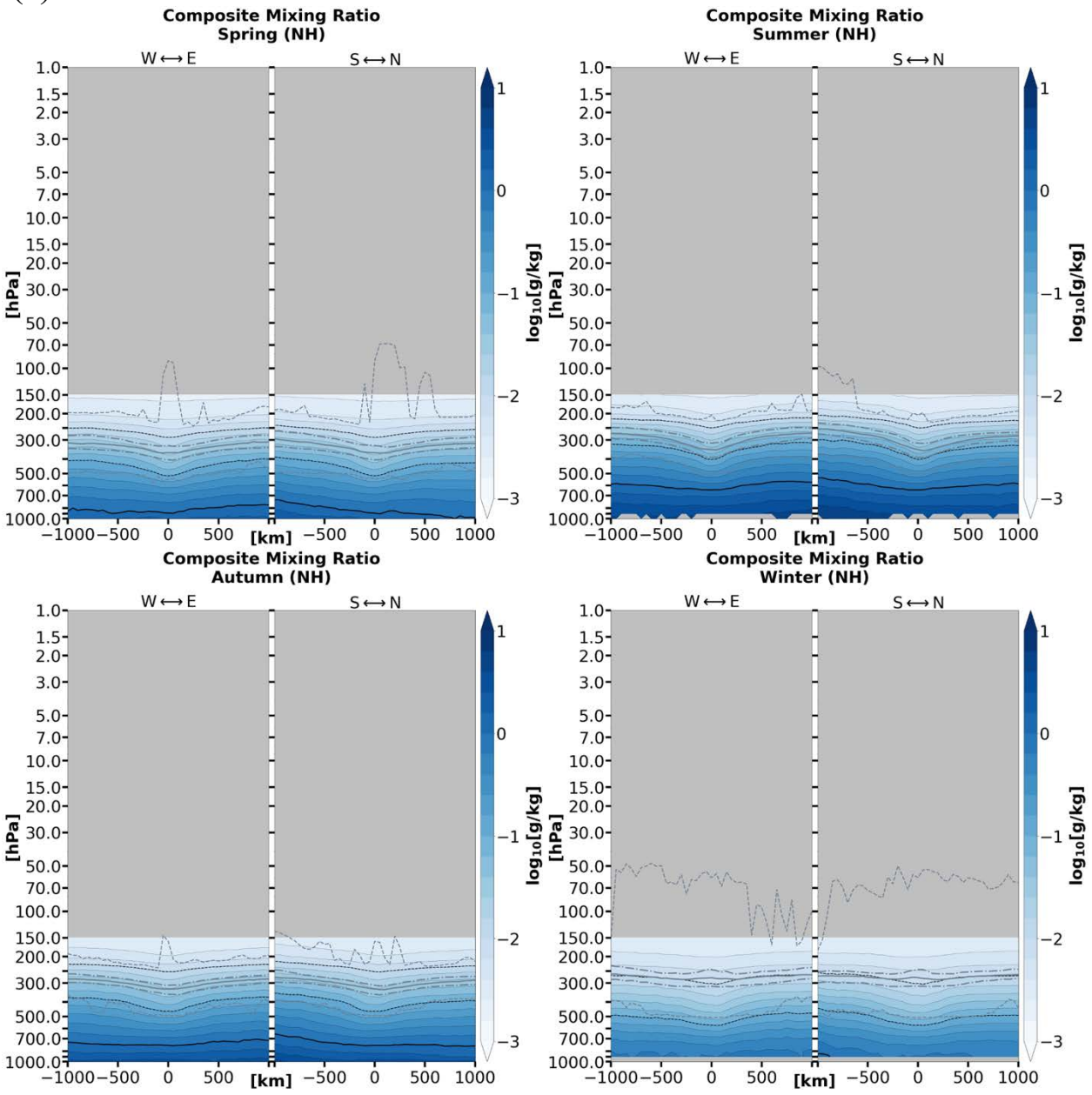

Figure A.4: Composite mean water vapor mass mixing ratio of TPV cases by season and hemisphere.

(b)

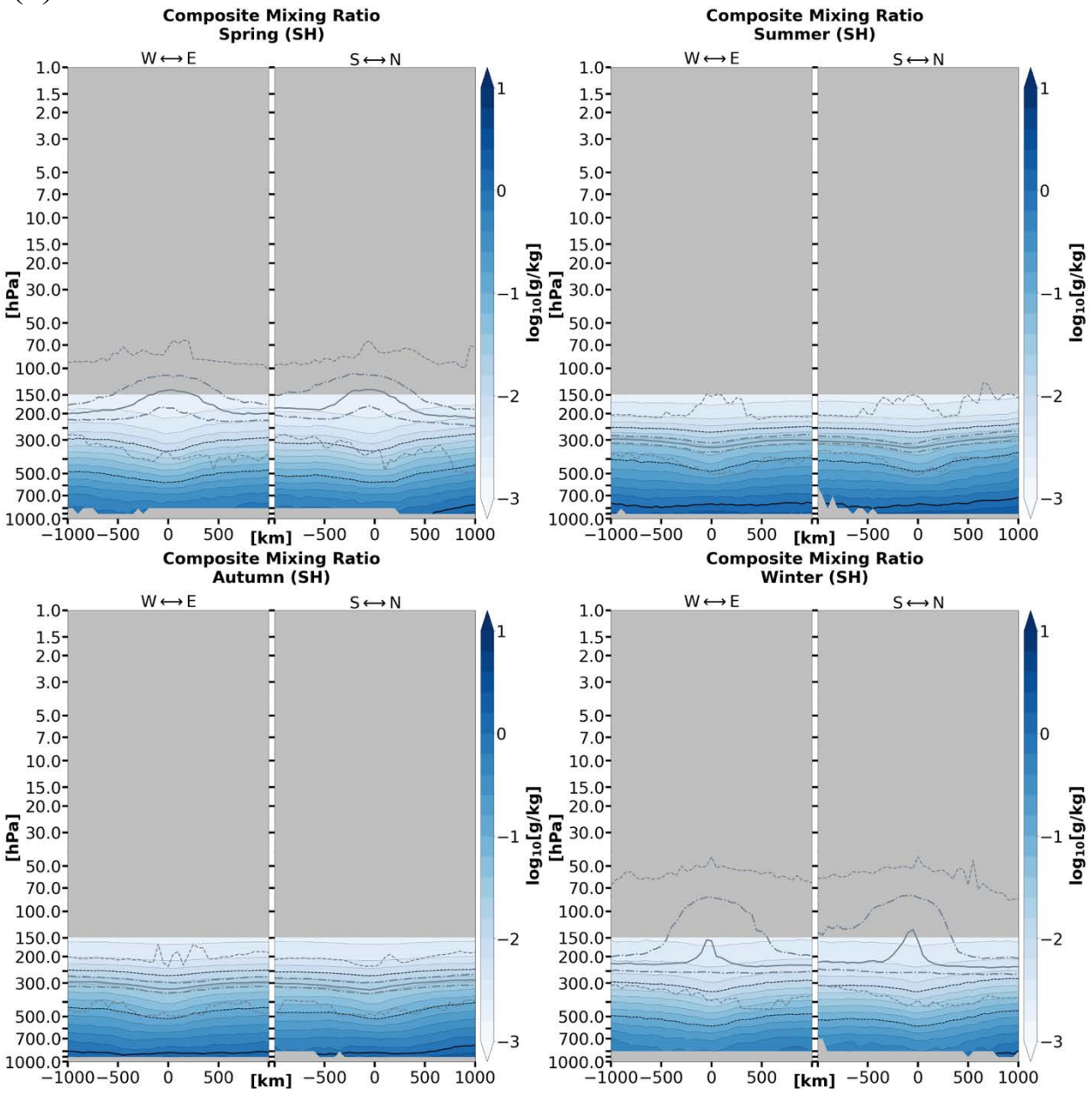

Figure A.4 (continued)

(a)

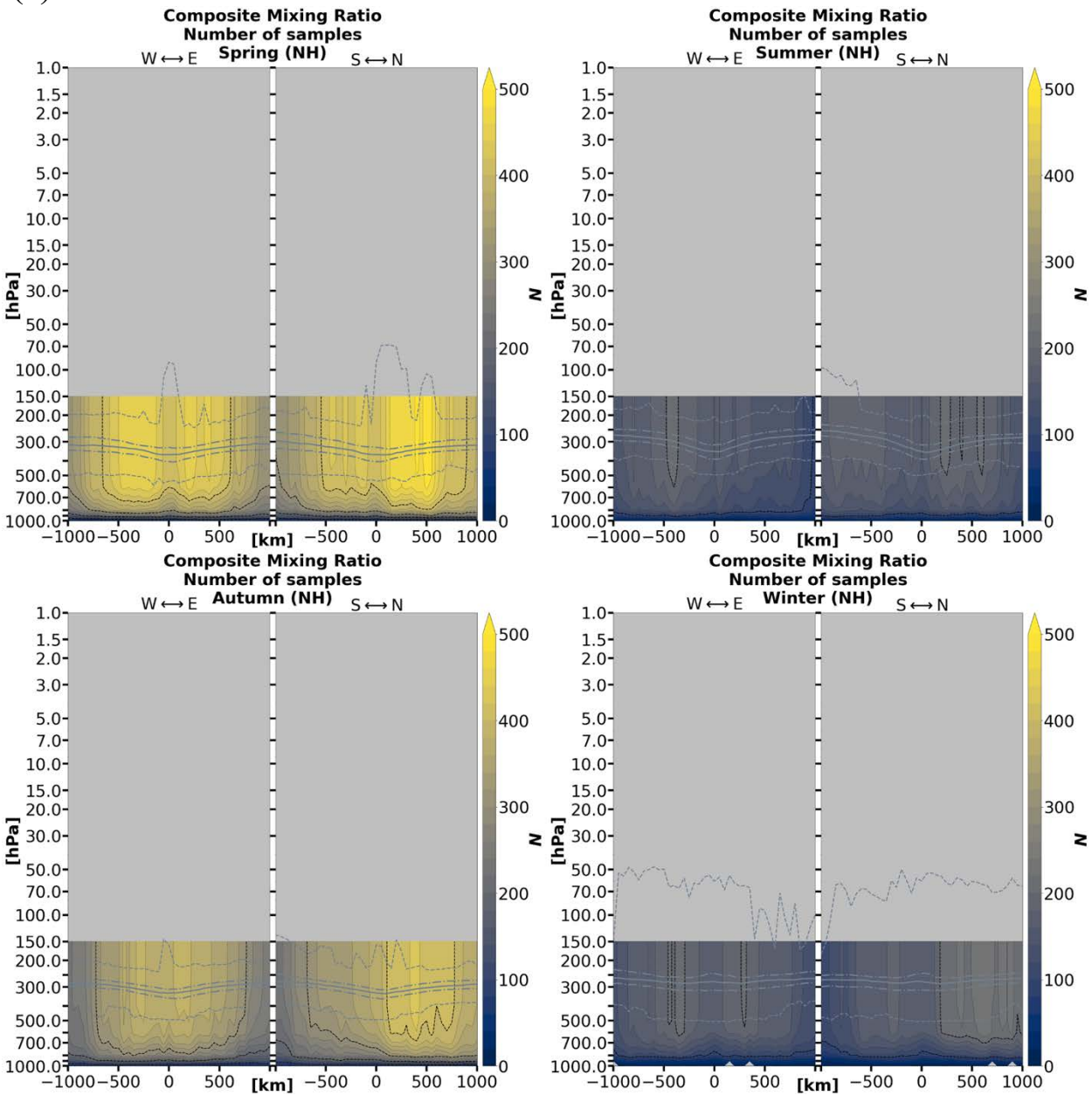

Figure A.5: Number of samples by grid point for the composite mean water mass mixing ratio of TPV cases by season and hemisphere.

(b)

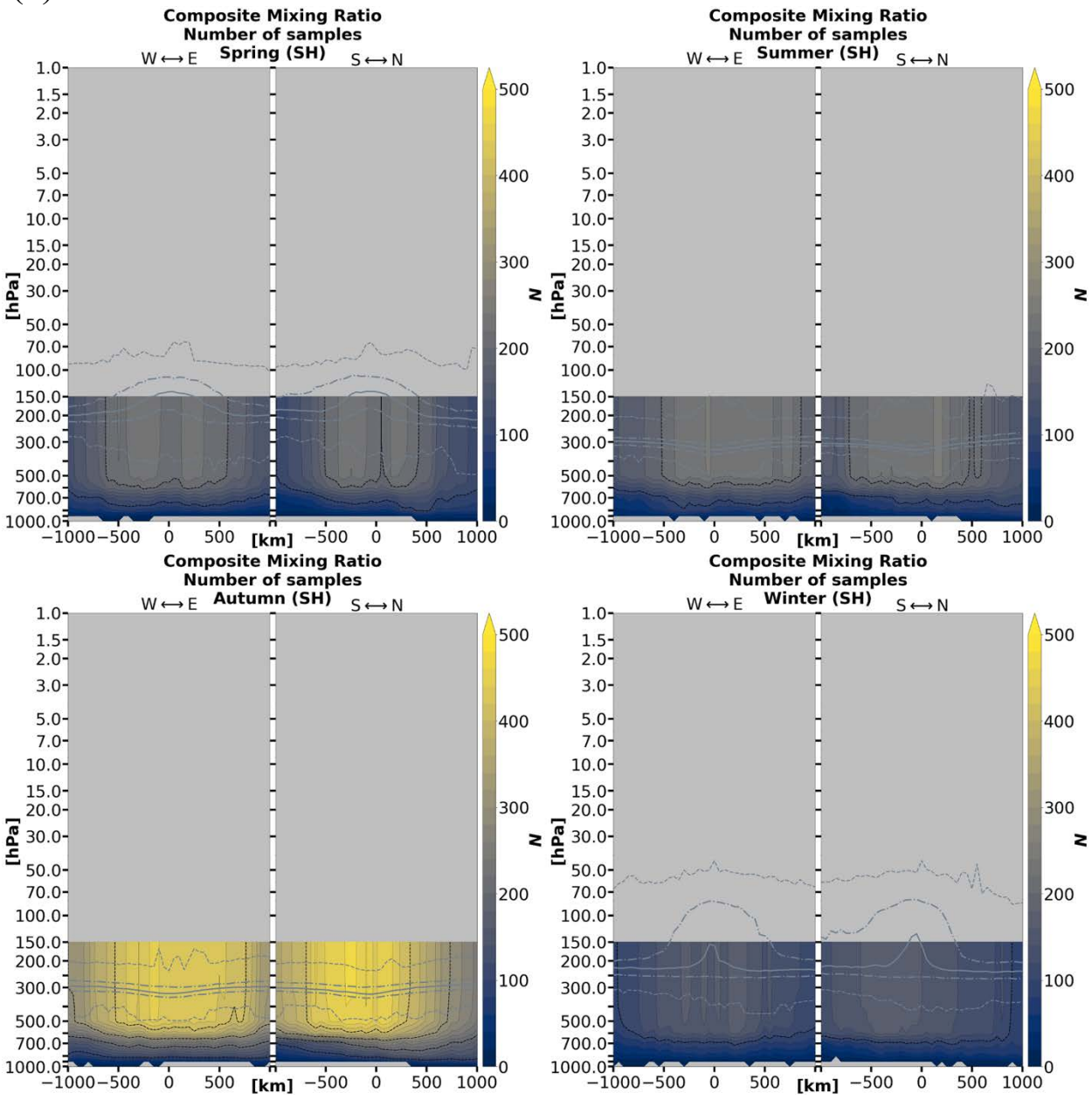

Figure A.5 (continued)

(a)

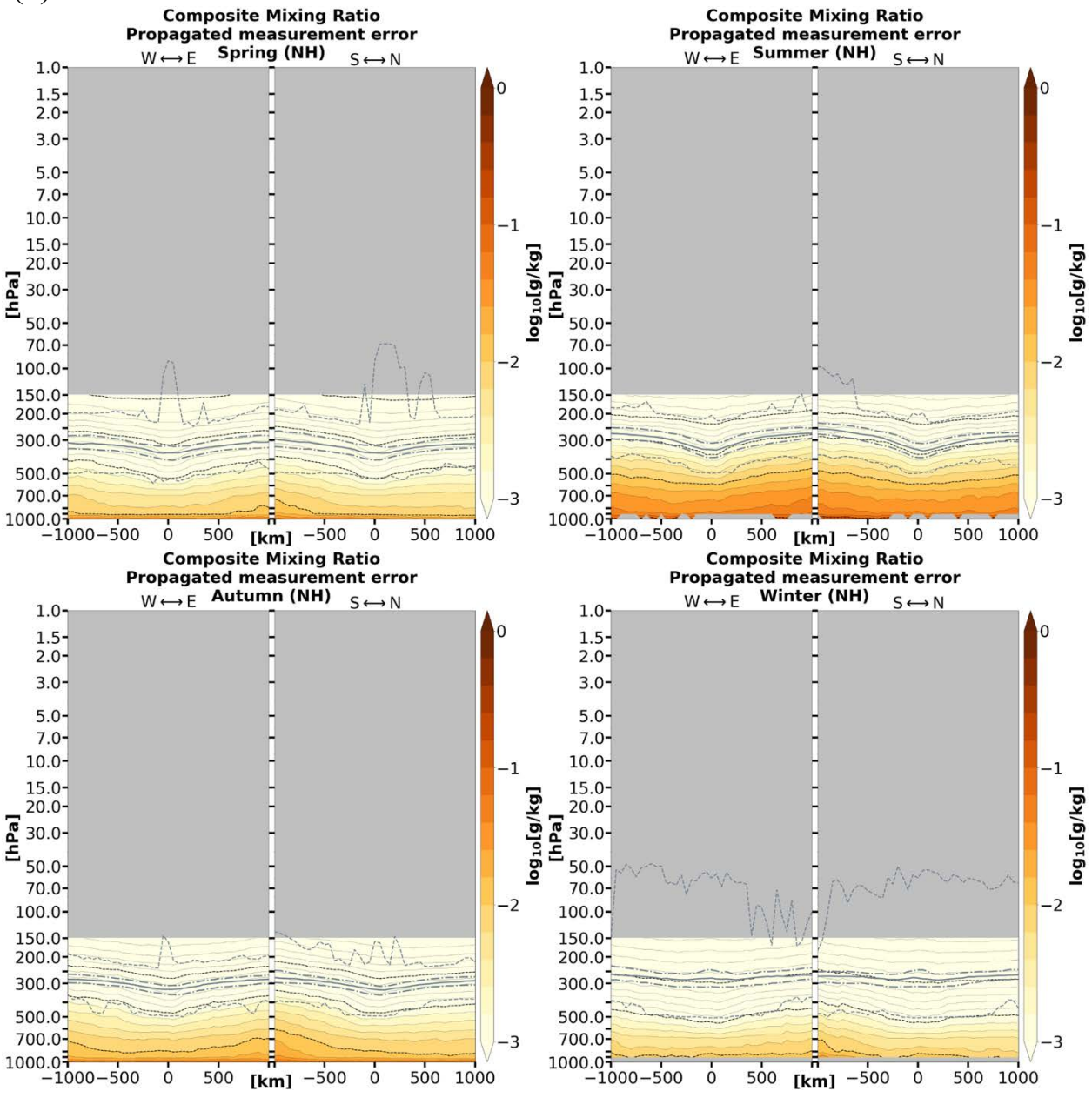

Figure A.6: Calculated error for the composite mean water vapor mass mixing ratio of TPV cases by season and hemisphere.

(b)

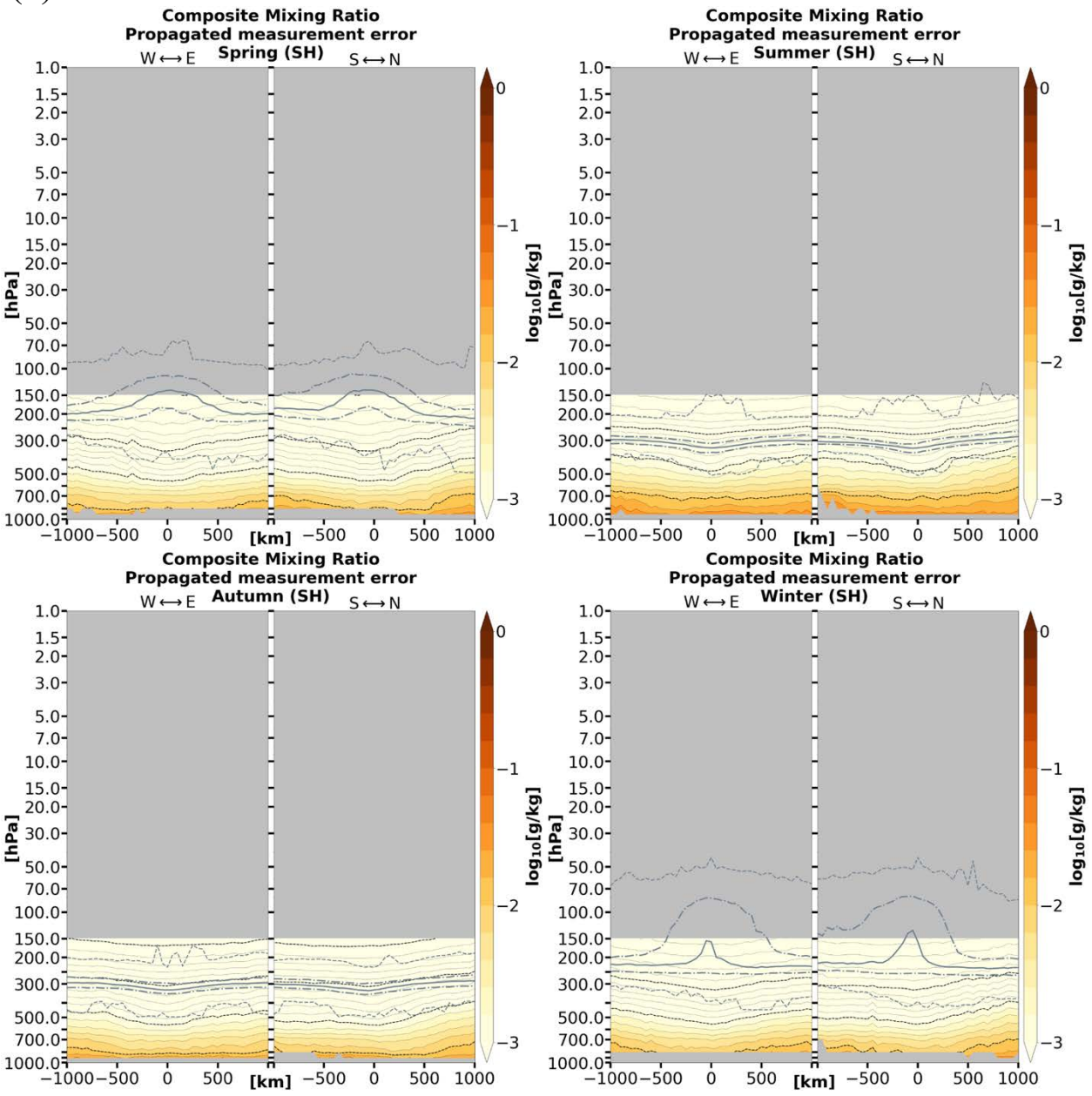

Figure A.6 (continued)

(a)

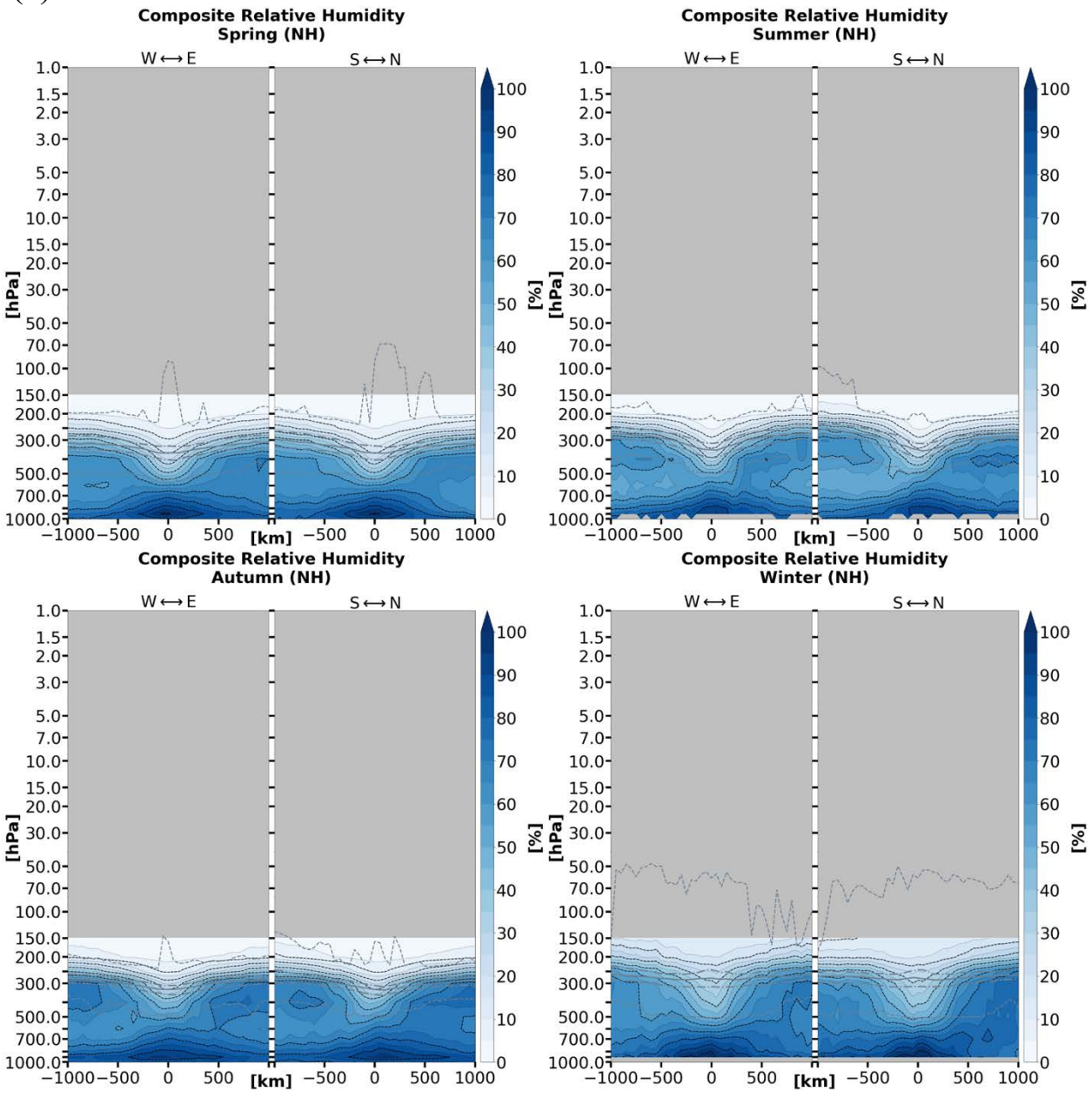

Figure A.7: Composite mean relative humidity of TPV cases by season and hemisphere.

(b)

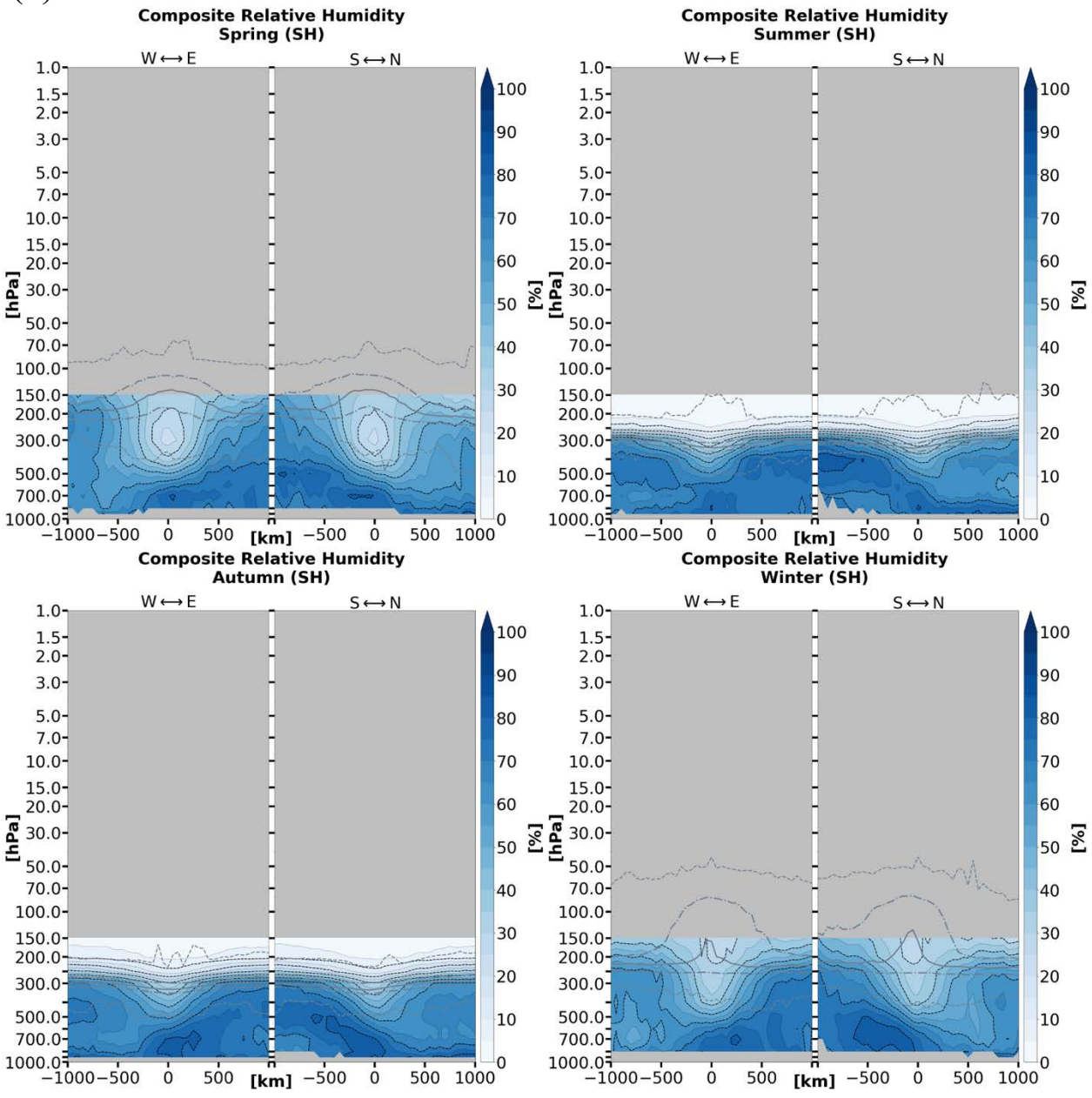

Figure A.7 (continued)

(a)

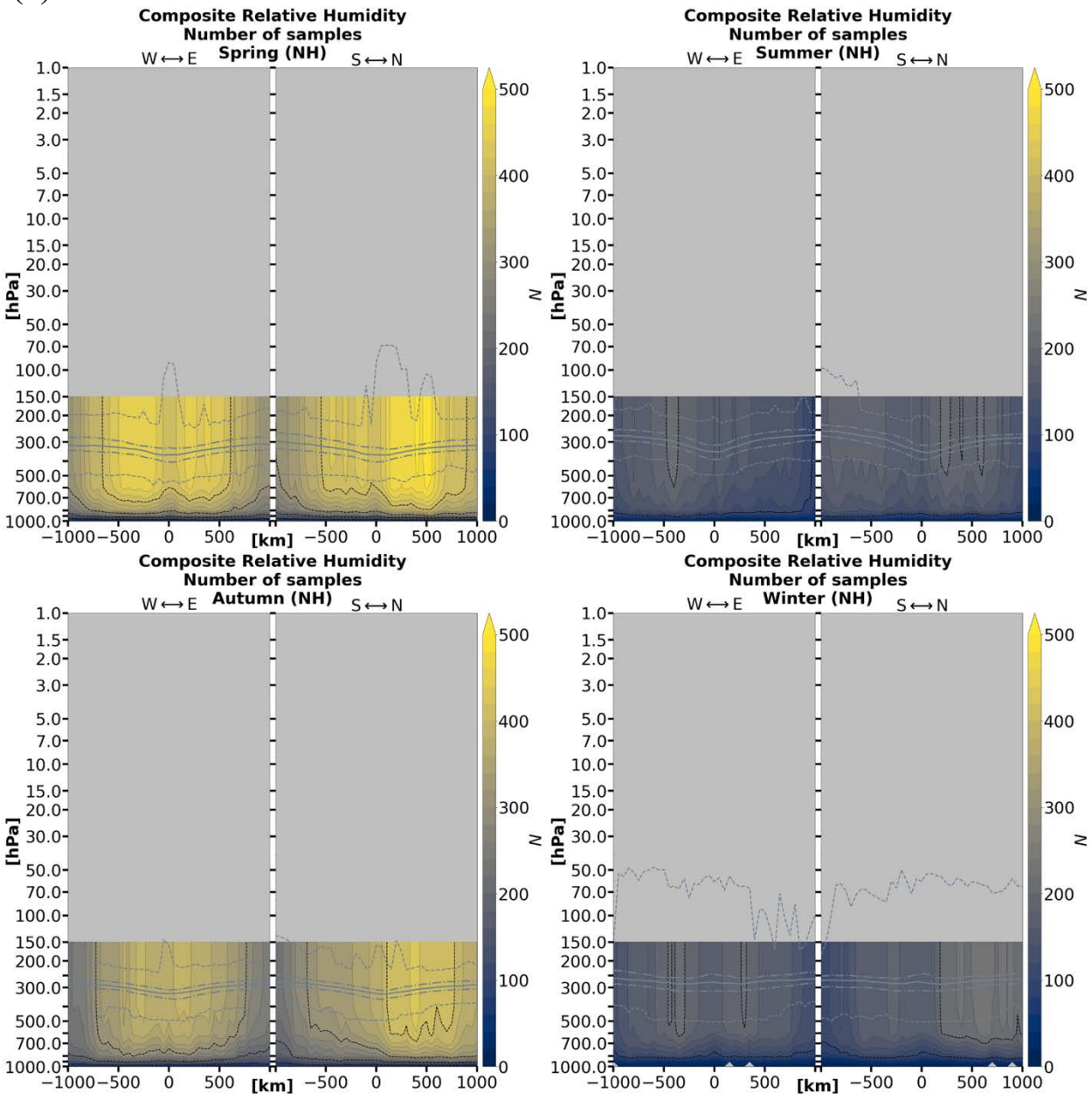

Figure A.8: Number of samples by grid point for the composite mean relative humidity of TPV cases by season and hemisphere.

(b)

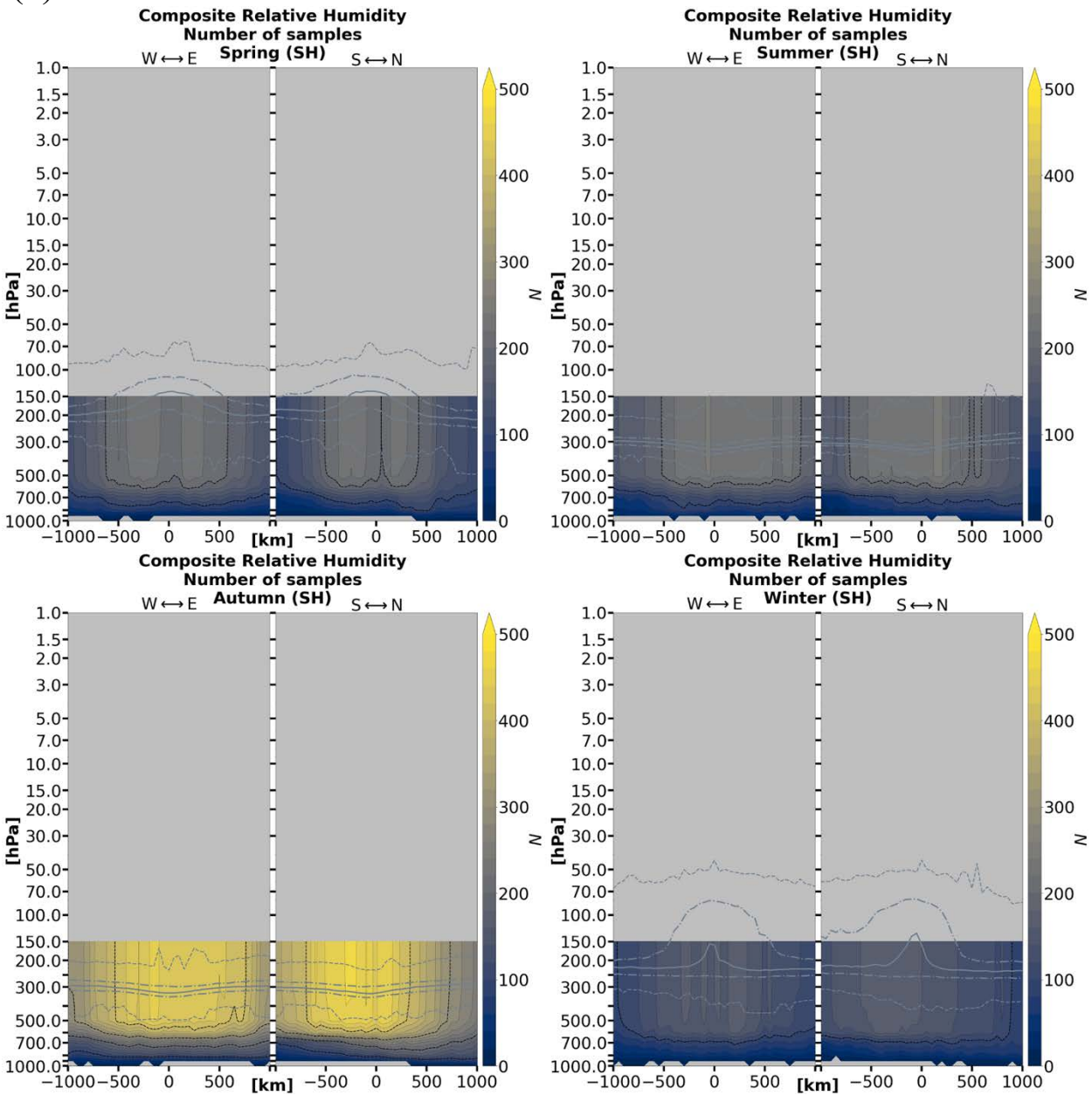

Figure A.8 (continued)

(a)

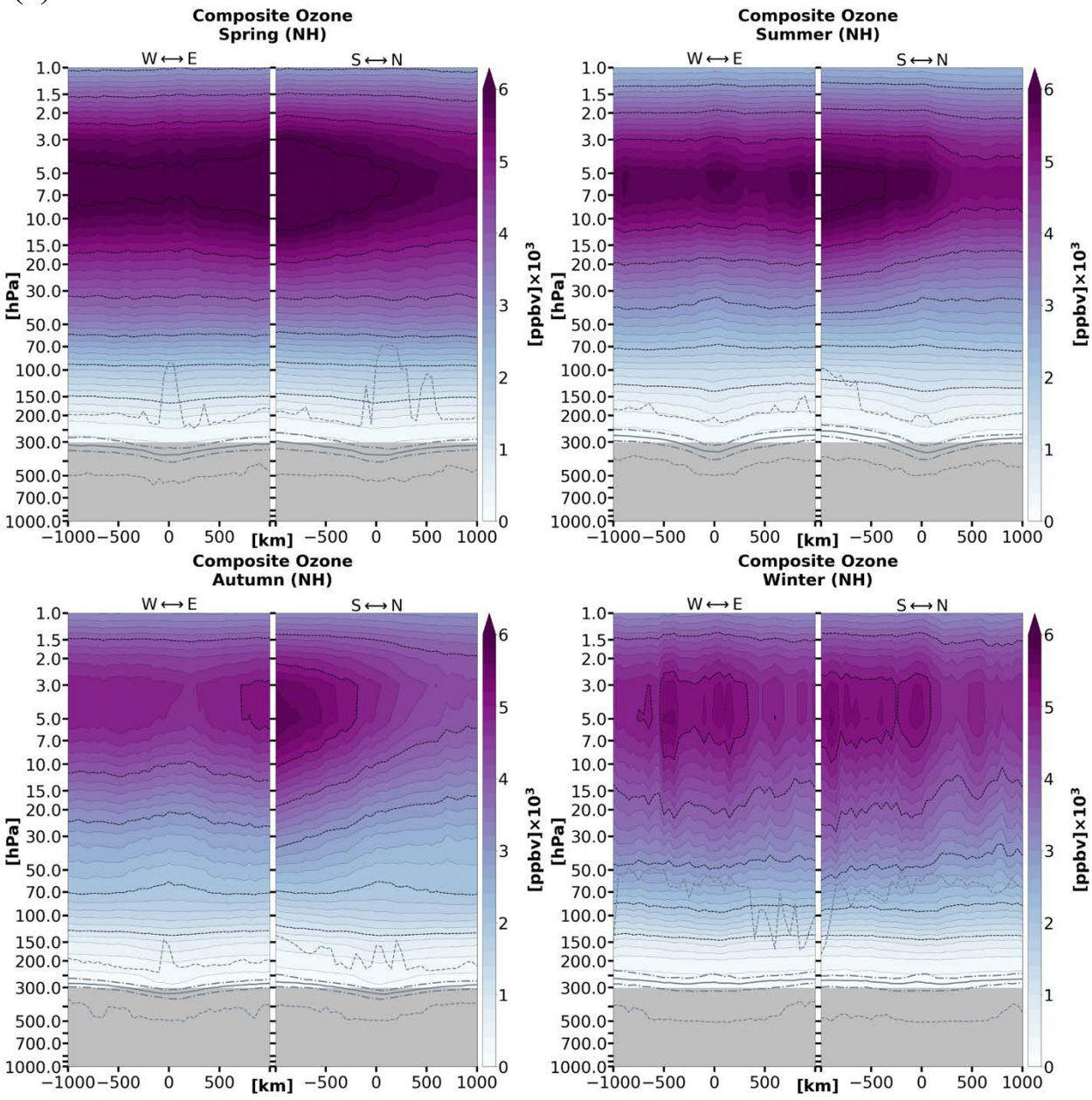

Figure A.9: Composite mean ozone volume mixing ratio of TPV cases by season and hemisphere.

(b)

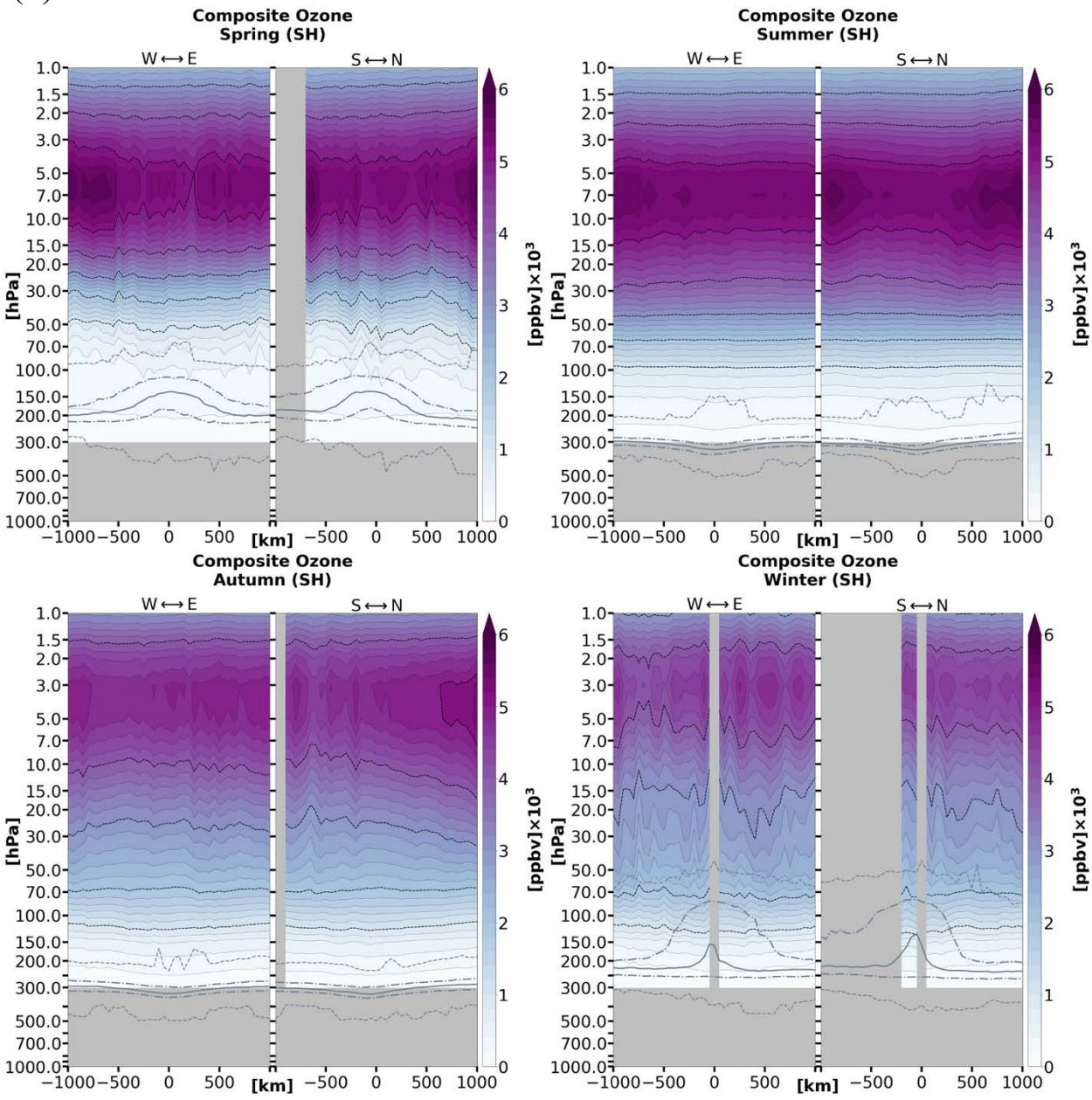

Figure A.9 (continued)

(a)

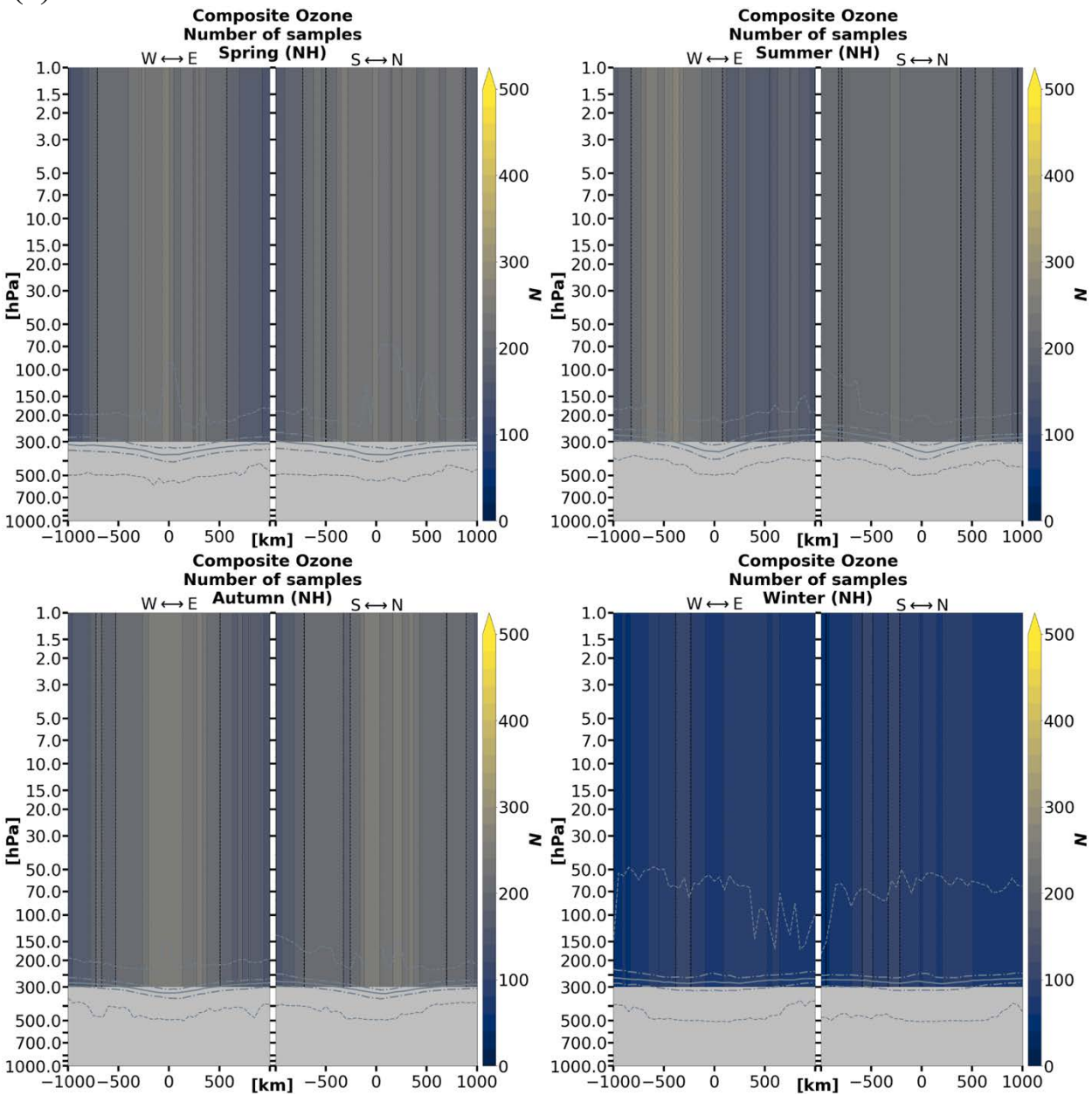

Figure A.10: Number of samples by grid point for the omposite mean ozone volume mixing ratio of TPV cases by season and hemisphere.

(b)

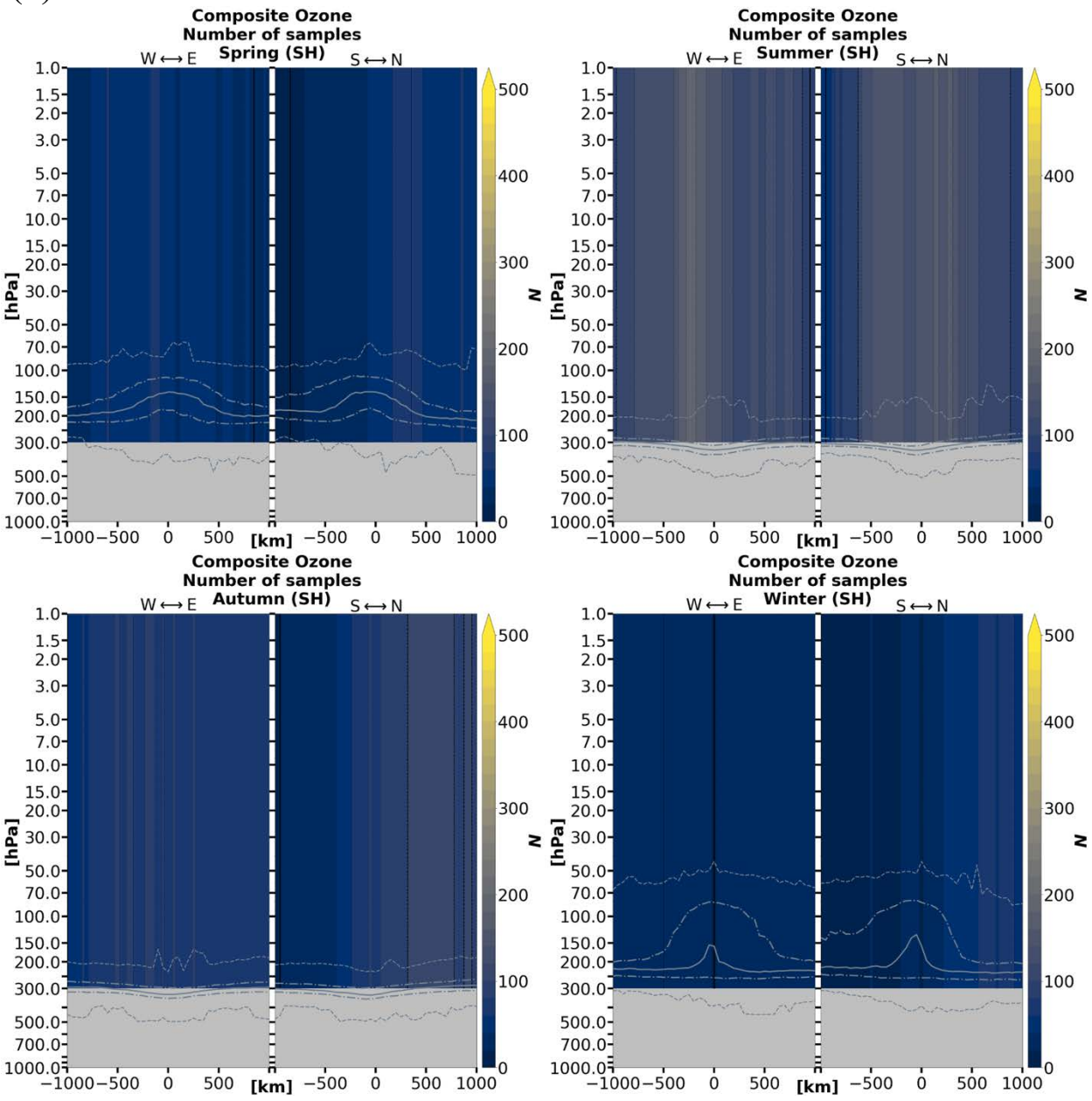

Figure A.10 (continued)

References

Adem, Julián. 1956. "A series solution for the barotropic vorticity equation and its application in the study of atmospheric vortices." *Tellus* 8 (3): 364-372.

Aumann, Hartmut H, Moustafa T Chahine, Catherine Gautier, Mitchell D Goldberg, Eugenia Kalnay, Larry M McMillin, Hank Revercomb, Philip W Rosenkranz, William L Smith, and David H Staelin. 2003. "AIRS/AMSU/HSB on the Aqua mission: Design, science objectives, data products, and processing systems." *IEEE Transactions on Geoscience and Remote Sensing* 41 (2): 253-264.

Aumann, Hartmut H, and Robert J Pagano. 1994. "Atmospheric infrared sounder on the Earth Observing System." *Optical Engineering* 33 (3): 776-784.

Biernat, Kevin A, Lance F Bosart, and Daniel Keyser. 2021. "A climatological analysis of the linkages between tropopause polar vortices, cold pools, and cold air outbreaks over the central and eastern United States." *Monthly Weather Review* 149 (1): 189-206.

Bolton, David. 1980. "The computation of equivalent potential temperature." *Monthly weather review* 108 (7): 1046-1053.

Borg, Sarah M, Steven M Cavallo, and David D Turner. 2020. "Characteristics of Tropopause Polar Vortices Based on Observations over the Greenland Ice Sheet." *Journal of Applied Meteorology and Climatology* 59 (11): 1933-1947.

Bosart, Lance F, Gregory J Hakim, Kevin R Tyle, Mary A Bedrick, W Edward Bracken, Michael J Dickinson, and David M Schultz. 1996. "Large-scale antecedent conditions associated with the 12–14 March 1993 cyclone ("Superstorm'93") over eastern North America." *Monthly weather review* 124 (9): 1865-1891.

Bray, Matthew T, and Steven M Cavallo. 2022. "Characteristics of long-track tropopause polar vortices." *Weather and Climate Dynamics* 3 (1): 251-278.

Bray, Matthew T, Steven M Cavallo, and Howard B Bluestein. 2021. "Examining the Relationship between Tropopause Polar Vortices and Tornado Outbreaks." *Weather and Forecasting* 36 (5): 1799-1814.

Bromwich, David H, Julien P Nicolas, Keith M Hines, Jennifer E Kay, Erica L Key, Matthew A Lazzara, Dan Lubin, Greg M McFarquhar, Irina V Gorodetskaya, and Daniel P Grosvenor. 2012. "Tropospheric clouds in Antarctica." *Reviews of Geophysics* 50 (1).

Carnevale, George F, Geoffrey K Vallis, Roberto Purini, and Marco Briscolini. 1988. "Propagation of barotropic modons over topography." *Geophysical & Astrophysical Fluid Dynamics* 41 (1-2): 45-101.

Cavallo, S. M., and G. J. Hakim. 2009. "Potential Vorticity Diagnosis of a Tropopause Polar Cyclone." *Monthly Weather Review* 137 (4): 1358-1371. https://doi.org/10.1175/2008mwr2670.1. <Go to ISI>://WOS:000266834100010.

---. 2010. "Composite Structure of Tropopause Polar Cyclones." *Monthly Weather Review* 138 (10): 3840-3857. https://doi.org/10.1175/2010mwr3371.1. <Go to ISI>://WOS:000283264600008.

---. 2012. "Radiative Impact on Tropopause Polar Vortices over the Arctic." *Monthly Weather Review* 140 (5): 1683-1702. https://doi.org/10.1175/mwr-d-11-00182.1. <Go to ISI>://WOS:000303790800016.

---. 2013. "Physical Mechanisms of Tropopause Polar Vortex Intensity Change." *Journal of the Atmospheric Sciences* 70 (11): 3359-3373. https://doi.org/10.1175/jas-d-13-088.1. <Go to ISI>://WOS:000326354600002.

Cesana, G, JE Kay, H Chepfer, JM English, and G De Boer. 2012. "Ubiquitous low-level liquid-containing Arctic clouds: New observations and climate model constraints from CALIPSO-GOCCP." *Geophysical Research Letters* 39 (20).

Curry, JA, JL Schramm, and EE Ebert. 1993. "Impact of clouds on the surface radiation balance of the Arctic Ocean." *Meteorology and Atmospheric Physics* 51 (3): 197-217.

Curry, Judith A, Julie L Schramm, William B Rossow, and David Randall. 1996. "Overview of Arctic cloud and radiation characteristics." *Journal of Climate* 9 (8): 1731-1764.

Davis, Christopher A, and Kerry A Emanuel. 1991. "Potential vorticity diagnostics of cyclogenesis." *Monthly weather review* 119 (8): 1929-1953.

De Boer, Gijs, William Chapman, Jennifer E Kay, Brian Medeiros, Matthew D Shupe, Steve Vavrus, and John Walsh. 2012. "A characterization of the present-day Arctic atmosphere in CCSM4." *Journal of Climate* 25 (8): 2676-2695.

Dee, D. P., S. M. Uppala, A. J. Simmons, P. Berrisford, P. Poli, S. Kobayashi, U. Andrae, M. A. Balmaseda, G. Balsamo, P. Bauer, P. Bechtold, A. C. M. Beljaars, L. van de Berg, J. Bidlot, N. Bormann, C. Delsol, R. Dragani, M. Fuentes, A. J. Geer, L. Haimberger, S. B. Healy, H. Hersbach, E. V. Holm, L. Isaksen, P. Kallberg, M. Kohler, M. Matricardi, A. P. McNally, B. M. Monge-Sanz, J. J. Morcrette, B. K. Park, C. Peubey, P. de Rosnay, C. Tavolato, J. N. Thepaut, and F. Vitart. 2011. "The ERA-Interim reanalysis: configuration and performance of the data assimilation system." *Quarterly Journal of the Royal Meteorological Society* 137 (656): 553-597. https://doi.org/10.1002/qj.828. <Go to ISI>://WOS:000290450900001.

Esri, Redlands. 2011. "ArcGIS desktop: release 10." *Environmental Systems Research Institute, CA*.

Francis, J. A., and S. J. Vavrus. 2012. "Evidence linking Arctic amplification to extreme weather in mid-latitudes." *Geophysical Research Letters* 39: 6. https://doi.org/10.1029/2012gl051000. <Go to ISI>://WOS:000301668300004.

Fuenzalida, Humberto A, Rodrigo Sánchez, and René D Garreaud. 2005. "A climatology of cutoff lows in the Southern Hemisphere." *Journal of Geophysical Research: Atmospheres* 110 (D18).

Gordon, Andrea E, Steven M Cavallo, and Amanda K Novak. 2022. "Evaluating Common Characteristics of Antarctic Tropopause Polar Vortices." *Journal of the Atmospheric Sciences*.

Gray, Suzanne L, Kevin I Hodges, Jonathan L Vautrey, and John Methven. 2021. "The role of tropopause polar vortices in the intensification of summer Arctic cyclones." *Weather and Climate Dynamics* 2 (4): 1303-1324.

Hakim, G. J. 2000. "Climatology of coherent structures on the extratropical tropopause." *Monthly Weather Review* 128 (2): 385-406. https://doi.org/10.1175/1520-0493(2000)128<0385:cocsot>2.0.co;2. <Go to ISI>://WOS:000085230500007.

Hakim, G. J., and A. K. Canavan. 2005. "Observed cyclone-anticyclone tropopause vortex Asymmetries." *Journal of the Atmospheric Sciences* 62 (1): 231-240. https://doi.org/10.1175/jas-3353.1.

Hakim, Gregory J, Lance F Bosart, and Daniel Keyser. 1995. "The Ohio Valley wave-merger cyclogenesis event of 25–26 January 1978. Part I: Multiscale case study." *Monthly Weather Review* 123 (9): 2663-2692.

Hakim, Gregory J, Daniel Keyser, and Lance F Bosart. 1996. "The Ohio Valley wave-merger cyclogenesis event of 25–26 January 1978. Part II: Diagnosis using quasigeostrophic potential vorticity inversion." *Monthly weather review* 124 (10): 2176-2205.
Hersbach, Hans, Bill Bell, Paul Berrisford, Shoji Hirahara, András Horányi, Joaquín Muñoz-Sabater, Julien Nicolas, Carole Peubey, Raluca Radu, and Dinand Schepers. 2020. "The ERA5 global reanalysis." *Quarterly Journal of the Royal Meteorological Society* 146 (730): 1999-2049.
Hoerling, Martin P, Todd K Schaack, and Allen J Lenzen. 1991. "Global objective tropopause analysis." *Monthly Weather Review* 119 (8): 1816-1831.
Hoskins, Brian, and Paul Berrisford. 1988. "A potential vorticity perspective of the storm of 15–16 October 1987." *Weather* 43 (3): 122-129.
Hoskins, Brian J, Michael E McIntyre, and Andrew W Robertson. 1985. "On the use and significance of isentropic potential vorticity maps." *Quarterly Journal of the Royal Meteorological Society* 111 (470): 877-946.
Huo, Zonghui, Da-Lin Zhang, John Gyakum, and Andrew Staniforth. 1995. "A diagnostic analysis of the superstorm of March 1993." *Monthly weather review* 123 (6): 1740-1761.
Johnson, Aaron, and Xuguang Wang. 2021. "Observation Impact Study of an Arctic Cyclone Associated with a Tropopause Polar Vortex (TPV)-Induced Rossby Wave Initiation Event." *Monthly Weather Review* 149 (5): 1577-1591.
Keegan, Thomas J. 1958. "Arctic synoptic activity in winter." *Journal of Atmospheric Sciences* 15 (6): 513-521.
Kew, Sarah F, Michael Sprenger, and Huw C Davies. 2010. "Potential vorticity anomalies of the lowermost stratosphere: A 10-yr winter climatology." *Monthly Weather Review* 138 (4): 1234-1249.
Kocin, Paul J, Philip N Schumacher, Ronald F Morales Jr, and Louis W Uccellini. 1995. "Overview of the 12–14 March 1993 superstorm." *Bulletin of the American Meteorological Society* 76 (2): 165-182.
Lillo, Samuel P, Steven M Cavallo, David B Parsons, and Christopher Riedel. 2021. "The role of a tropopause polar vortex in the generation of the January 2019 extreme Arctic outbreak." *Journal of the Atmospheric Sciences* 78 (9): 2801-2821.
McWilliams, James C, and Glenn R Flierl. 1979. "On the evolution of isolated, nonlinear vortices." *Journal of Physical Oceanography* 9 (6): 1155-1182.
McWilliams, JC. 1991. "Geostrophic vortices." *Nonlinear Topics in Ocean Physics*: 5-50.
Morgan, M. C., and J. W. Nielsen-Gammon. 1998. "Using tropopause maps to diagnose midlatitude weather systems." *Monthly Weather Review* 126 (10): 2555-2579. https://doi.org/10.1175/1520-0493(1998)126<2555:utmtdm>2.0.co;2.
Murphy, Daniel M, and Thomas Koop. 2005. "Review of the vapour pressures of ice and supercooled water for atmospheric applications." *Quarterly Journal of the Royal Meteorological Society: A journal of the atmospheric sciences, applied meteorology and physical oceanography* 131 (608): 1539-1565.
Nieto, R, M Sprenger, Heini Wernli, RM Trigo, and L Gimeno. 2008. "Identification and Climatology of Cut-off Lows near the Tropopause." *Annals of the New York Academy of Sciences* 1146 (1): 256-290.
Papritz, Lukas, Emmanuel Rouges, Franziska Aemisegger, and Heini Wernli. 2019. "On the thermodynamic preconditioning of Arctic air masses and the role of tropopause polar

vortices for cold air outbreaks from Fram Strait." *Journal of Geophysical Research: Atmospheres* 124 (21): 11033-11050.
Pinheiro, Henri, Manoel Gan, and Kevin Hodges. 2021. "Structure and evolution of intense austral cut-off lows." *Quarterly Journal of the Royal Meteorological Society* 147 (734): 1-20.
Pithan, Felix, Brian Medeiros, and Thorsten Mauritsen. 2014. "Mixed-phase clouds cause climate model biases in Arctic wintertime temperature inversions." *Climate dynamics* 43 (1): 289-303.
Price, JD, and G Vaughan. 1992. "Statistical studies of cut-off-low systems." Annales geophysicae (1988).
Pyle, Matthew E, Daniel Keyser, and Lance F Bosart. 2004. "A diagnostic study of jet streaks: Kinematic signatures and relationship to coherent tropopause disturbances." *Monthly weather review* 132 (1): 297-319.
Rasmussen, Erik A. 2003. "Polar lows." In *A Half Century of Progress in Meteorology: A Tribute to Richard Reed*, 61-78. Springer.
Reed, Richard J, and Bruce A Kunkel. 1960. "The Arctic circulation in summer." *Journal of the Atmospheric Sciences* 17 (5): 489-506.
Reznik, GM, and WK Dewar. 1994. "An analytical theory of distributed axisymmetric barotropic vortices on the β-plane." *Journal of Fluid Mechanics* 269: 301-321.
Rossby, Carl-Gustaf. 1940. "Planetary flow pattern in the atmosphere. Quart." *J. Roy. Meteor. Soc.* 66: 68-87.
Rossby, CG. 1948. "On displacements and intensity changes of atmospheric vortices." *J. mar. Res* 7 (175): 71.
Röthlisberger, Matthias, Olivia Martius, and Heini Wernli. 2018. "Northern Hemisphere Rossby wave initiation events on the extratropical jet—A climatological analysis." *Journal of Climate* 31 (2): 743-760.
Screen, James A, Ian Simmonds, and Kevin Keay. 2011. "Dramatic interannual changes of perennial Arctic sea ice linked to abnormal summer storm activity." *Journal of Geophysical Research: Atmospheres* 116 (D15).
Shupe, Matthew D, and Janet M Intrieri. 2004. "Cloud radiative forcing of the Arctic surface: The influence of cloud properties, surface albedo, and solar zenith angle." *Journal of climate* 17 (3): 616-628.
Shupe, Matthew D, David D Turner, Alexander Zwink, Mandana M Thieman, Eli J Mlawer, and Timothy Shippert. 2015. "Deriving Arctic cloud microphysics at Barrow, Alaska: Algorithms, results, and radiative closure." *Journal of Applied Meteorology and Climatology* 54 (7): 1675-1689.
Shupe, Matthew D, Von P Walden, Edwin Eloranta, Taneil Uttal, James R Campbell, Sandra M Starkweather, and Masataka Shiobara. 2011. "Clouds at Arctic atmospheric observatories. Part I: Occurrence and macrophysical properties." *Journal of Applied Meteorology and Climatology* 50 (3): 626-644.
Simmonds, Ian, Kevin Keay, and Eun-Pa Lim. 2003. "Synoptic activity in the seas around Antarctica." *Monthly Weather Review* 131 (2): 272-288.
Simmonds, Ian, and Irina Rudeva. 2012. "The great Arctic cyclone of August 2012." *Geophysical Research Letters* 39 (23).
Spaete, Paul, Donald R Johnson, and Todd K Schaack. 1994. "Stratospheric–Tropospheric Mass Exchange during the Presidents' Day Storm." *Monthly weather review* 122 (3): 424-439.

Stoelinga, Mark T. 1996. "A potential vorticity-based study of the role of diabatic heating and friction in a numerically simulated baroclinic cyclone." *Monthly weather review* 124 (5): 849-874.
Stramler, Kirstie, Anthony D Del Genio, and William B Rossow. 2011. "Synoptically driven Arctic winter states." *Journal of Climate* 24 (6): 1747-1762.
Susskind, J, J Blaisdell, L Iredell, J Lee, A Milstein, C Barnet, E Fishbein, E Manning, L Strow, and J Teixeira. 2020. "AIRS-Team Retrieval For Core Products and Geophysical Parameters: Versions 6 and 7 Level 2." *Jet Propulsion Laboratory, Pasadena*.
Susskind, Joel, Chris Barnet, John Blaisdell, Lena Iredell, Fricky Keita, Lou Kouvaris, Gyula Molnar, and Moustafa Chahine. 2006. "Accuracy of geophysical parameters derived from Atmospheric Infrared Sounder/Advanced Microwave Sounding Unit as a function of fractional cloud cover." *Journal of Geophysical Research: Atmospheres* 111 (D9).
Susskind, Joel, Christopher D Barnet, and John M Blaisdell. 2003. "Retrieval of atmospheric and surface parameters from AIRS/AMSU/HSB data in the presence of clouds." *IEEE Transactions on Geoscience and Remote Sensing* 41 (2): 390-409.
Szapiro, N., and S. Cavallo. 2018. "TPVTrack v1.0: a watershed segmentation and overlap correspondence method for tracking tropopause polar vortices." *Geoscientific Model Development* 11 (12): 5173-5187. https://doi.org/10.5194/gmd-11-5173-2018. <Go to ISI>://WOS:000454113900001.
Takayabu, Izuru. 1991. "" Coupling development": an efficient mechanism for the development of extratropical cyclones." *Journal of the Meteorological Society of Japan. Ser. II* 69 (6): 609-628.
Taljaard, JJ. 1967. "Development, distribution and movement of cyclones and anticyclones in the Southern Hemisphere during the IGY." *Journal of Applied Meteorology and Climatology* 6 (6): 973-987.
Thorpe, Alan J. 1986. "Synoptic scale disturbances with circular symmetry." *Monthly weather review* 114 (7): 1384-1389.
Thorpe, Alan J, and Hans Volkert. 1997. "Potential vorticity: A short history of its definitions and uses." *Meteorologische Zeitschrift* 6: 275-280.
Thrastarson, Heidar Th, EF Fetzer, Sharon Ray, Thomas Hearty, and Nadia Smith. 2021. "Overview of the AIRS Mission: Instruments, Processing Algorithms, Products, and Documentation." *Jet Propulsion Laboratory California Institute of Technology, Pasadena, CA, https://docserver. gesdisc. eosdis. nasa. gov/public/project/AIRS/Overview_of_the_AIRS_Mission. pdf, last access* 1.
Thrastarson, Heidar Th, Evan Manning, Brian Kahn, E Fetzer, Qing Yue, Sun Wong, Peter Kalmus, Vivienne Payne, E Olsen, and RC Wilson. 2020. "AIRS/AMSU/HSB Version 7 Level 2 Product User Guide." *Jet Propulsion Laboratory, California Institute of Technology: Pasadena, CA, USA*: 83-92.
Tjernström, Michael, Joseph Sedlar, and Matthew D Shupe. 2008. "How well do regional climate models reproduce radiation and clouds in the Arctic? An evaluation of ARCMIP simulations." *Journal of Applied Meteorology and Climatology* 47 (9): 2405-2422.
Turner, DD, MD Shupe, and AB Zwink. 2018. "Characteristic atmospheric radiative heating rate profiles in Arctic clouds as observed at Barrow, Alaska." *Journal of Applied Meteorology and Climatology* 57 (4): 953-968.
Uccellini, Louis W, Daniel Keyser, Keith F Brill, and Carlyle H Wash. 1985. "The Presidents' Day cyclone of 18–19 February 1979: Influence of upstream trough amplification and

associated tropopause folding on rapid cyclogenesis." *Monthly Weather Review* 113 (6): 962-988.

Uccellini, Louis W, Paul J Kocin, Ralph A Petersen, Carlyle H Wash, and Keith F Brill. 1984. "The Presidents' Day cyclone of 18–19 February 1979: Synoptic overview and analysis of the subtropical jet streak influencing the pre-cyclogenetic period." *Monthly weather review* 112 (1): 31-55.

Uccellini, Louis W, Paul J Kocin, Russell S Schneider, Paul M Stokols, and Russell A Dorr. 1995. "Forecasting the 12–14 March 1993 superstorm." *Bulletin of the American Meteorological Society* 76 (2): 183-200.

Walsh, John E, David H Bromwich, James E Overland, Mark C Serreze, and Kevin R Wood. 2018. "100 years of progress in polar meteorology." *Meteorological Monographs* 59: 21.1-21.36.

Waugh, Darryn W, Adam H Sobel, and Lorenzo M Polvani. 2017. "What is the polar vortex and how does it influence weather?" *Bulletin of the American Meteorological Society* 98 (1): 37-44.

Wirth, Volkmar. 1995. "Diabatic heating in an axisymmetric cut-off cyclone and related stratosphere-troposphere exchange." *Quarterly Journal of the Royal Meteorological Society* 121 (521): 127-147.

Zierl, Bärbel, and Volkmar Wirth. 1997. "The influence of radiation on tropopause behavior and stratosphere-troposphere exchange in an upper tropospheric anticyclone." *Journal of Geophysical Research: Atmospheres* 102 (D20): 23883-23894.